9.1 Interferometry

H.J. Tiziani, N. Kerwien, G. Pedrini

9.1.1 Introduction

Interferometry is a powerful tool for many applications in optics, spectroscopy, and optical metrology. Interference phenomena can be observed in daily live, for example when colors in a soap bubble or in oil slicks on a wet road appear. Colored fringes, the so-called "Newton rings", are seen in a thin air film enclosed between two glass plates brought in contact. Interference results from the superposition of two or more at least partially coherent electromagnetic waves. The characteristic feature of the interference phenomenon is a spatially modulated intensity distribution in the region of superposition, that differs in magnitude from the mean intensity values of the superimposing beams.

The development of optical interferometry is closely linked with the history of wave optics. In 1690 Huygens put forward the basis for the theory we use today. In 1801, Thomas Young performed a fundamental experiment for demonstrating interference and the wave nature of light, see Fig. 9.1.26. He used monochromatic light passing a single pinhole first and subsequently traveling to two separated slits or pinholes. The light diffracted from these pinholes illuminates a screen at a distance much larger than the pinhole separation. Then interference fringes can be seen in the overlapping area. The simple demonstration is the well-known Young experiment. In 1816 Fresnel and Arago perfected these investigations. Since two orthogonal polarized light waves could not interfere Young concluded out of these experiments that light waves are transverse waves.

Applications of interferometry in optical metrology followed in succession. In 1896 Michelson carried out the first interferometric measurements to determine the length of the Pt-Ir bar which was the international prototype of the meter and defined its length in terms of the wavelength of the red cadmium radiation. In 1960 followed the redefinition of the meter with the wavelength of the orange radiation of ^{86}Kr.

Interferometry plays also an important role in optical testing and high-precision metrology. Twyman used 1916 a modified Michelson-interferometer for testing optical components. This interferometer was adapted by Linnik 1933 for the examination of microscopic structures of reflecting surfaces. Furthermore, interferometry has important applications in spectroscopy as well as for studies of fluid flow and combustion, but these will not be discussed here.

Different developments led to new applications of interferometry. To these belongs the progress in the development of lasers as coherent light source as well as the automated computer-assisted fringe analysis together with the development of high-resolution detector arrays based on CCD (Charge Coupled Device) or CMOS (Complementary Metal Oxide Semiconductor) technology.

For micro- and nanotechnology and especially for structures with lateral dimensions near or smaller than the wavelength of the light used, coherence properties and polarization need to be considered, as will be discussed, see Sect. 9.1.2.4 and Sect. 9.1.4.4.

Speckle pattern interferometry (see Sect. 9.1.7) as well as holographic interferometry (see Sect. 9.1.8) plays an important role in non-destructive testing in our days. The test object is, however, not a highly polished surface but rather an optically rough surface.

9.1.2 Basic principles of interference

Before we start with a detailed discussion of different interferometric methods in the following sections, we first give a short summary of the basic principles of interferometry. Starting point in Sect. 9.1.2.1 is the very short discussion of coherence as a necessary prerequisite for the occurrence of interference phenomena, see also Part 6 in this volume. In Sect. 9.1.2.2 we describe the mathematical basics of two-beam interference, in Sect. 9.1.2.3 the interference in a plane-parallel plate, and in Sect. 9.1.2.4 we account for the vectorial character of light interference.

9.1.2.1 Coherence

Two overlaid beams of light produce only an interference pattern, if their relative phases are stable long enough to be sensed by a detecting system (i.e. the eye). In this case we say the two beams are coherent. The coherence of light will be treated extensively in Born and Wolf [87Bor] as well as in Part 6 of this volume, therefore a brief introduction will be given here only.

The first quantitative concepts of coherence were formulated by Laue 1907. The basis for modern coherence theory was derived by van Cittert [34Van, 39Van] and Zernike [38Zer]. The van Cittert–Zernike theorem is well-known in spatial coherence descriptions. The theory was further developed by Hopkins [51Hop, 53Hop, 55Hop] and Wolf [54Wol, 55Wol] including higher-order coherence theory described by Mandel and Wolf [65Man]. For simplicity and to point out the main aspects we will discuss in the following only two special cases of the general term of coherence: the pure temporal as well as the pure spatial coherence.

9.1.2.1.1 Temporal coherence

The Fourier Transform (FT) $\mathcal{F}$ of the spectral energy distribution of the light source leads to the coherence time T_{coh}. Multiplication with the velocity of the light c gives the coherence length $L = cT_{\mathrm{coh}}$. With $T_{\mathrm{coh}} = 1/\Delta\nu$ and $\nu = c/\lambda$ we get:

$$L \approx \frac{\lambda^2}{|\Delta\lambda|} \,. \tag{9.1.1}$$

These relationships are illustrated in Fig. 9.1.1.

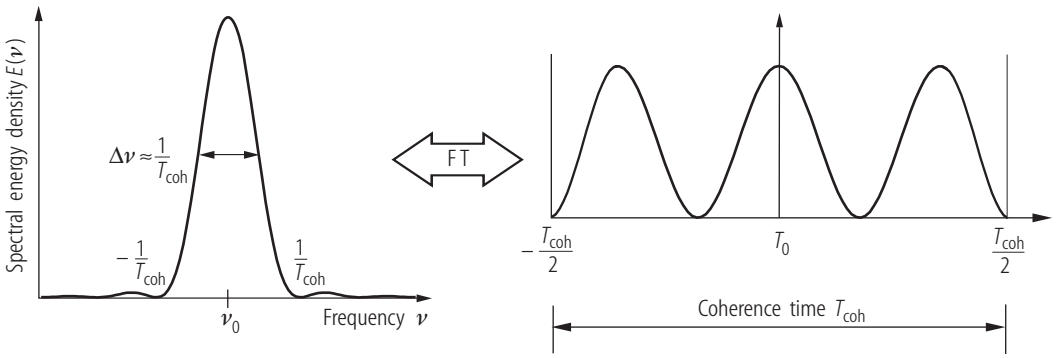

Fig. 9.1.1. Relationship between spectral energy density $E(\nu)$ of a light spectrum and its temporal behavior of the corresponding light train with coherence time T_{coh}.

9.1.2.1.2 Spatial coherence

It can be shown that the complex degree of coherence is equivalent to the calculation of the complex amplitude in a diffraction pattern. The well-known van Cittert–Zernike theorem was developed by van Cittert [34Van, 39Van] and presented in a simpler way by Zernike. For simplicity let us consider the source to be replaced by a screen with randomly distributed grains with random phase illuminated by a spherical wave. In the focusing plane the complex degree of spatial coherence is the Fourier transform of the source area [51Hop, 87Bor].

9.1.2.2 Two-beam interference

The light wave is propagating as an electromagnetic wave in vacuum. For simplicity we assume at first a scalar plane wave propagating in vacuum in z-direction. In Sect. 9.1.2.4 polarization effects will be discussed. The electric field E at any point can be represented by a sinusoidal function of distance z and time t:

$$E = a \cos\left[2\pi\nu\left(t - \frac{z}{c}\right)\right] , \tag{9.1.2}$$

where a is the amplitude, ν the frequency, and c the speed of propagation of the wave in vacuum. The period of vibration T is

$$T = \frac{1}{\nu} = \frac{2\pi}{\omega} ,$$

where ω is the circular frequency. The wavelength λ is given by the relation

$$\lambda = cT = \frac{c}{\nu} .$$

k is the propagation constant of the wave,

$$k = \frac{2\pi}{\lambda} .$$

The speed of the light propagation in the medium with the refractive index n is $v = c/n$. The wavelength in the medium is now

$$\lambda_n = \frac{\lambda}{n} .$$

It is convenient to use the complex representation of light waves. Equation (9.1.2) can then be written as

$$E = \mathrm{Re}\left\{a \exp\left[\mathrm{i}\,2\pi\nu\left(t - \frac{zn}{c}\right)\right]\right\} , \tag{9.1.3}$$

where $\mathrm{Re}\{\}$ represents the real part of the expression within the braces and $\mathrm{i} = \sqrt{-1}$. We can write (9.1.3) as a product of the time- and space-varying functions

$$E = \mathrm{Re}\left\{a \exp(-\mathrm{i}\,\phi) \exp(\mathrm{i}\,2\pi\nu t)\right\} = A \exp(2\,\mathrm{i}\,\pi\nu t) , \tag{9.1.4}$$

where $\phi = 2\pi nz/\lambda$ is the phase and nz is the optical path difference from the origin of z.

It should be noticed that the frequency of the visible light is in the order of 6×10^{14} Hz. Therefore a direct observation of the electric field is not possible. The only measurable quantity is the time average of the amount of energy, which in a unit of time crosses a unit area normal to the

direction of the energy flow. This is proportional to the time average of the square of the electric field:

$$\langle E^2 \rangle = \lim_{T\to\infty} \frac{1}{2T} \int_{-T}^{T} E^2 \, \mathrm{d}t = \lim_{T\to\infty} \frac{1}{2T} \int_{-T}^{T} a^2 \, \cos^2(\omega t - \phi) \, \mathrm{d}t = \frac{a^2}{2} \, . \tag{9.1.5}$$

We are, however, not interested in the absolute intensity, but only in the relative values over the specified region. We can ignore the factor $\frac{1}{2}$, as well as any other factors of proportionality, and define the optical intensity as

$$I = a^2 = |A|^2 \, . \tag{9.1.6}$$

Let us now consider two monochromatic waves propagating in the same direction superposed in a point P. The total electric field at this point is

$$E = E_1 + E_2 \, , \tag{9.1.7}$$

where E_1 and E_2 are the electric fields due to the two waves. Assuming that the two waves have the same frequency, the intensity at this point is

$$I = |A_1 + A_2|^2 \, . \tag{9.1.8}$$

Considering $A_1 = a_1 \exp(-\mathrm{i}\,\phi_1)$ and $A_2 = a_2 \exp(-\mathrm{i}\,\phi_2)$ to be the complex amplitudes of the two waves of the same wavelength, we obtain:

$$I = A_1^2 + A_2^2 + A_1 A_2^* + A_1^* A_2 = I_1 + I_2 + 2\,\gamma_{12} \sqrt{I_1 I_2} \, \cos(\phi_1 - \phi_2) \, , \tag{9.1.9}$$

where I_1 and I_2 are the intensities at P for the two waves acting separately (incoherent superposition) and γ_{12} is the coherence factor. Equation (9.1.9) is often called the general interference law for stationary optical fields [87Bor]. For incoherent light $\gamma_{12} = 0$ and for perfectly coherent light $\gamma_{12} = 1$. For partial coherence γ_{12} is between 0 and 1. We consider at first $\gamma_{12} = 1$, i.e. perfect coherence.

The intensity has its maximum $I_{\max}$ when $\phi_1 - \phi_2 = 2\,m\,\pi$, where m is an integer. The minima occur for $\phi_1 - \phi_2 = (2m+1)\,\pi$. The intensity can be written according to (9.1.9) as

$$I = I_0 \, \{1 + \gamma \, \cos(\phi_1 - \phi_2)\} \, , \tag{9.1.10}$$

where $I_0 = I_1 + I_2$ and the contrast γ or visibility (sometimes called modulation m) is conveniently defined according to Michelson

$$\gamma = \frac{(I_{\max} - I_{\min})}{(I_{\max} + I_{\min})} = \frac{2\sqrt{I_1 I_2}}{I_1 + I_2} \, . \tag{9.1.11}$$

Maximum visibility is obtained for $I_1 = I_2$.

9.1.2.3 Interference in a plane-parallel plate

Up to now we have treated interference from a quite abstract point of view. In the following we will give a simple example where interference occurs in a plane-parallel plate. The effects demonstrated here will also be the basis for more sophisticated methods described especially in Sect. 9.1.3. The principal arrangement and the notations used are depicted in Fig. 9.1.2. The refractive index of the glass plate is n_1 and the surrounding medium is considered to be air ($n = 1.0$). The angle of incidence is ϑ and the angle after refraction is ϑ_1'. The optical path

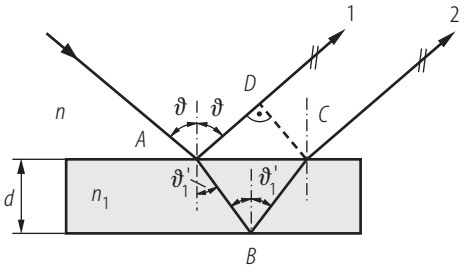

Fig. 9.1.2. Optical path difference between the front and back surface of a plane-parallel plate.

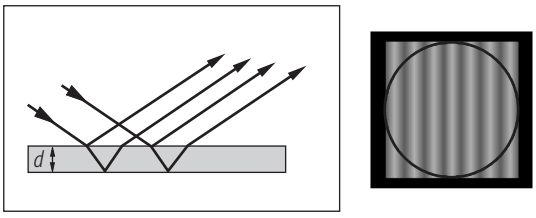

a

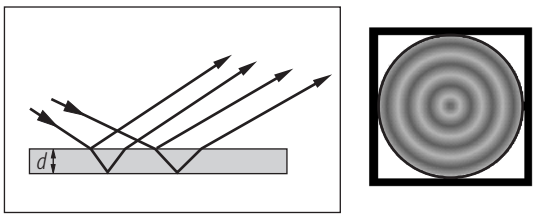

b

Fig. 9.1.3. Plane-parallel plate illuminated with (**a**) a small light source (parallel incident light) with the corresponding fringe pattern and (**b**) a large light source together with the appropriate fringe pattern at infinity or in the focus plane of a lens. In order to see fringes a small wedge angle was introduced in the plate for (**a**).

difference between the waves reflected from the front and back surface for a plane-parallel plate is by neglecting a phase jump at the interface

$$\Delta = [ABC] - [AD] = 2n_1 d \cos(\vartheta'_1) \ , \tag{9.1.12}$$

where $[ABC]$ means the optical path corresponding to the geometrical path following the points A, B, and C multiplied with the refractive index n_1. It should be noted that there is a phase jump of π at the interface, which can be derived from the Fresnel equations at the boundary. The optical path difference is therefore

$$\Delta = 2n_1 d \cos(\vartheta'_1) \pm \frac{\lambda}{2} \ . \tag{9.1.13}$$

In Fig. 9.1.3 fringe patterns for a small and a large monochromatic light source, respectively, are seen. The source is placed in the focal plane of a collimating lens. An ideal point source therefore generates a parallel beam, whereas an extended light source results in a divergence of the light beam. The fringes in Fig. 9.1.3a are called Fizeau fringes (fringes of equal thickness) and in Fig. 9.1.3b Haidinger fringes (fringes of equal inclination). It should be noted that in Fig. 9.1.3a there is a small wedge angle introduced into the plate in order to see parallel and equidistant fringes (tilt fringes). For a perfect plane-parallel plate no Fizeau fringes would be observed (uniform field). The existence of fringes of equal inclination depends on the direction of the incident light being reflected by the two parallel surfaces. The Optical Path Difference (OPD) depends on the angle of incidence of the waves. The fringe patterns are therefore different, for the same plane-parallel plate, depending on whether a point or extended source is used. By contrast for the same incidence direction the OPD is the same.

9.1.2.4 Vector effects of interference

Up to now we have treated light as a scalar quantity and therefore didn't account for the real nature of light, especially its vectorial character. Initially assuming that light performs longitudinal vibrations, Fresnel and Arago did systematic investigations on this topic in 1816. Their set-up resembled Young's earlier experiments despite the fact, that different configurations of polarizers in front of the light source, the slits, and the screen are involved in the experiments. Their work was the basis of understanding the transverse nature of light and led to empirical statements, called the interference laws of Fresnel and Arago [1819Ara]. They can be formulated in a slightly modernized form [92Bro, 93Col] as (see also Fig. 9.1.4):

1. Two waves linearly polarized in the same plane can interfere (Fig. 9.1.4a).
2. Two waves linearly polarized with perpendicular polarizations cannot interfere (Fig. 9.1.4b).
3. Two waves linearly polarized with perpendicular polarizations, if derived from perpendicular components of unpolarized light and subsequently brought into the same plane of polarization, cannot interfere (Fig. 9.1.4c).
4. Two waves linearly polarized with perpendicular polarizations, if derived from the same linearly polarized wave and subsequently brought into the same plane of polarization, can interfere (Fig. 9.1.4d).

Stating these laws as experimental facts, Fresnel and Arago didn't provide the theoretical and mathematical basis. This step was preserved to Stokes, who picked up the investigations of Fresnel and Arago and formulated his famous paper in 1852 [1852Sto]. A deeper discussion would lead to the partial coherence theory of polarized light, which is not the scope of this text. We will just restate some fundamental results and definitions here, which are important for some experiments to follow. For further reading we refer to excellent literature that covers this subject [62Shu, 92Bro, 93Col]. Following the same considerations as in Sect. 9.1.2.2 for two quasi-monochromatic plane waves in

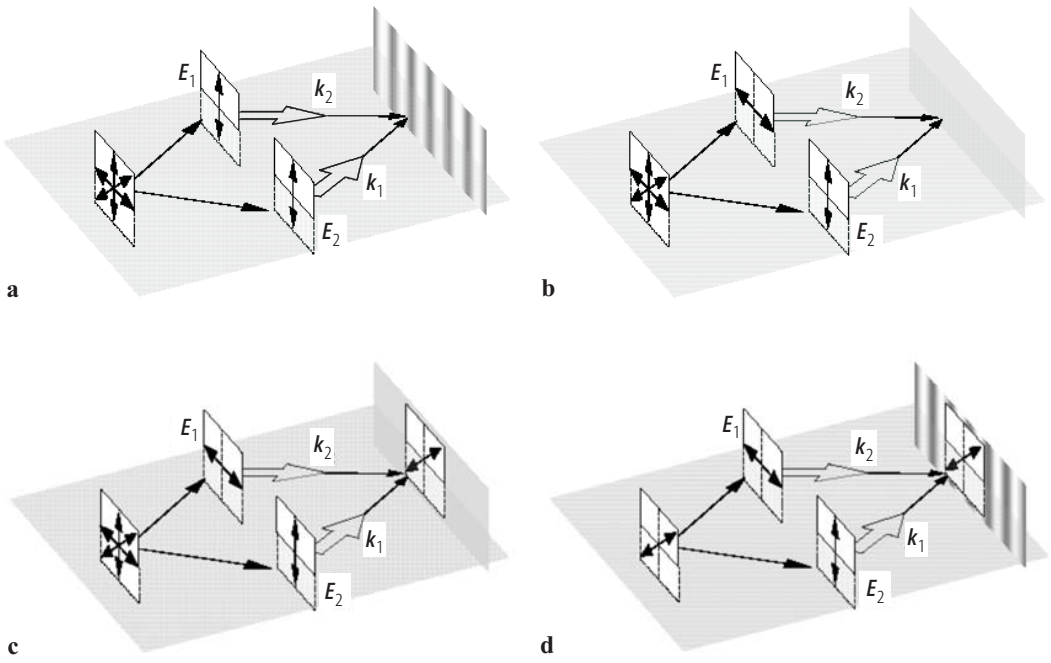

Fig. 9.1.4. Interference laws of Fresnel and Arago.

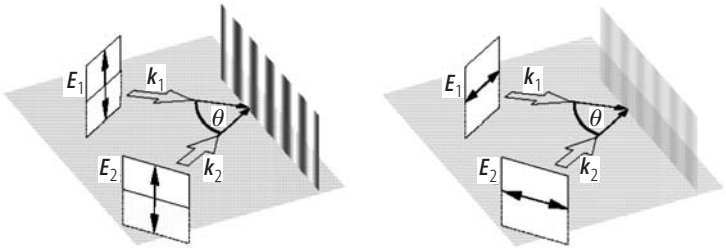

Fig. 9.1.5. Vector effects of interference. The contrast of the interference fringes depends on the mutual propagation direction and the polarization of the interfering plane waves.

vector formulation

$$\boldsymbol{E}_{1/2}(t) = \boldsymbol{a}_{1/2}(t)\,\exp\left\{\mathrm{i}\,\left(\boldsymbol{k}_{1/2}\,\boldsymbol{r} - 2\,\pi\,\bar{\nu}\,t + \phi_{1/2}(t)\right)\right\} \tag{9.1.14}$$

we get a quite similar interference equation as in (9.1.9) nevertheless revealing the characteristic polarization properties of interference:

$$I = \left\langle \boldsymbol{A}_1^2 \right\rangle + \left\langle \boldsymbol{A}_2^2 \right\rangle + 2\,\mathrm{Re}\left(\left\langle \boldsymbol{A}_1 \boldsymbol{A}_2^* \right\rangle\,\exp\left\{\mathrm{i}\,(\boldsymbol{k}_1 - \boldsymbol{k}_2)\,\boldsymbol{r}\right\}\right)\,, \tag{9.1.15}$$

where $\bar{\nu}$ denotes the mean frequency, $\boldsymbol{A}_{1/2} = \boldsymbol{a}_{1/2}\,\exp\left(-\mathrm{i}\,\phi_{1/2}\right)$ the in general complex vector amplitudes, $\phi_{1/2}$ the phases, and $\boldsymbol{k}_{1/2}$ the wave vectors of the corresponding plane waves, respectively. As in Sect. 9.1.2.2 Re stands for the real part and $\langle\ \rangle$ for the time-averaging operation defined in (9.1.5).

The chief difference to (9.1.9) consists in the replacement of the conventional product by the vectorial inner product both in the amplitude and the phase part of the interference term. This fact has quite important consequences, which lead to interference effects not explainable by scalar theory. They are subject of the following discussion.

We start with the two special cases depicted in Fig. 9.1.5. The plane spanned by the two wave vectors serves as reference plane. If the waves are both linearly polarized perpendicular to the reference plane (often referred to as TE-polarization) the field vectors are always parallel to each other regardless of the mutual angle of incidence θ and therefore cause the same interference pattern.

The situation is quite different for polarization vectors parallel to the reference plane. In this case of so-called TM-polarization the interference term depends on the aperture angle and is proportional to $\cos(\theta)$ as a consequence of the inner vector product. This means that starting with parallel propagating waves the contrast of the interference pattern decreases with increasing aperture angle. It even vanishes for $\theta = 90°$, i.e. perpendicular mutual incidence, before increasing again up to plane waves propagating in opposite direction.

As learned from the discussion above, waves with orthogonal polarization states don't interfere. This is also true for two orthogonal[1] polarized plane waves, which propagate in the same direction. Nevertheless, the question arises if there exists a relationship between the two vector components of the resulting wave, that can be described in a corresponding formalism to scalar coherence theory and that causes, under certain circumstances, similar interference effects.

To discuss this situation in more detail the propagation direction of the resulting plane wave is chosen along the z-axis, whereas the two partial waves are linearly polarized in x- und y-directions, respectively:

$$E_{x/y}(t) = a_{x/y}(t)\,\exp\left\{\mathrm{i}\,\left(\phi_{x/y}(t) - 2\,\pi\,\bar{\nu}\,t\right)\right\}\,. \tag{9.1.16}$$

In order to force the two orthogonal vector components to interfere, we have to project them onto the same plane of vibration (i.e. the same plane of polarization). Experimentally this is done by a polarizer. Let the polarizer be aligned in direction α to the x-axis, then we get:

[1] Up to now we have used the word "orthogonal" in a geometrical sense. Entering the scope of polarimetry the meaning is broadened to its mathematical definition common in theory of linear algebra.

$$E(t,\alpha) = E_x(t)\cos(\alpha) + E_y(t)\sin(\alpha) \ . \tag{9.1.17}$$

This results in the intensity:

$$\begin{aligned} I(\alpha) &= \langle E(t,\alpha)\, E^*(t,\alpha)\rangle \\ &= J_{xx}\cos^2(\alpha) + J_{yy}\cos^2(\alpha) + 2\sqrt{J_{xx}}\sqrt{J_{yy}}\cos(\alpha)\sin(\alpha)\,\mathrm{Re}(j_{xy}) \ , \end{aligned} \tag{9.1.18}$$

where we fall back on the definition of the coherency matrix:

$$\mathsf{J} = \begin{bmatrix} \langle E_x E_x^*\rangle & \langle E_x E_y^*\rangle \\ \langle E_y E_x^*\rangle & \langle E_y E_y^*\rangle \end{bmatrix} = \begin{bmatrix} \langle a_x^2\rangle & \langle a_x a_y\, \mathrm{e}^{\mathrm{i}(\phi_x-\phi_y)}\rangle \\ \langle a_x a_y\, \mathrm{e}^{-\mathrm{i}(\phi_x-\phi_y)}\rangle & \langle a_y^2\rangle \end{bmatrix} \tag{9.1.19}$$

and the complex correlation factor

$$j_{xy} = \frac{J_{xy}}{\sqrt{J_{xx}}\sqrt{J_{yy}}} = |j_{xy}|\ \mathrm{e}^{\mathrm{i}A\phi} \ . \tag{9.1.20}$$

While the absolute value of j_{xy} describes the degree of coherence of the two polarization components the phase of j_{xy} represents their effective phase difference. The introduced definitions and the structure of (9.1.15) resemble a natural generalization of the scalar interference law for stationary optical fields (9.1.9) to its vectorial form.

We close this section by defining a further essential quantity, the degree of polarization [98Mov, 99Piq, 00Mov]:

$$P = \frac{I_{\mathrm{polarized}}}{I_{\mathrm{total}}} = \sqrt{1 - \frac{4\det(\mathsf{J})}{(J_{xx}+J_{yy})^2}} \ . \tag{9.1.21}$$

In contrast to the coherency matrix and the correlation factor, the degree of polarization is independent of the choice of the coordinate system and therefore provides a fundamental measure of the partially coherent light field.

Now we have arrived at the basis of vectorial coherence theory. In Sect. 9.1.4.4 we will give some measurement examples that demonstrate the implementation of this formalism for metrological purposes. It is strongly related to the neighboring fields of polarimetry and ellipsometry.

9.1.3 Interferometry for optical testing

There are two general methods to produce mutually coherent waves for interference, namely wavefront division and amplitude division. For wavefront division different points on a wavefront are sampled to produce two new wavefronts. For amplitude division the wavefront is divided into two beams by some sort of beam splitter. Amplitude division is mainly used in optical testing. Interferometry is frequently used for length measurement in optical testing [66Fra]. In the following Fizeau fringes are considered.

9.1.3.1 Basic interferometer types

9.1.3.1.1 Michelson interferometer

Interferometry can be used to study phase variation across an optical wavefront. A frequently used interference arrangement is based on the Michelson principle, see Fig. 9.1.6. The beam splitter BS

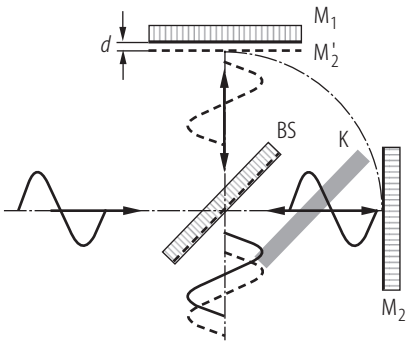

Fig. 9.1.6. Michelson arrangement.

separates reference and object waves and recombines them after reflection at the mirrors M_1, M_2. A compensating plate K of identical glass and the same thickness as the beam splitter compensates for the dispersion when a broad-band source is used. The compensating plate is not needed for optical testing with monochromatic light [21Mic, 66Fra, 72Wya, 87Bor, 90Har, 92Mal, 98Mov, 99Piq, 00Mov, 03Har].

9.1.3.1.2 Twyman–Green interferometer

The Twyman–Green arrangement is frequently used for optical testing with monochromatic light. A laser serves mainly as light source. Due to the small bandwidth no compensating plate is needed. The interferometer is appropriate for testing optical components and systems as shown schematically in Fig. 9.1.7 for testing a spherical surface (S) or alternatively the objective (Obj.). The laser beam is expanded by the lenses L_1 and L_2. The reference is reflected by the reference mirror R and the beam splitter BS. The object beam is reflected by BS and the spherical mirror S with its center of curvature in the focal point of the objective under test. The test object is passed twice in turn.

For testing the prism quality in transmission alternatively a prism mirror system can be put into the parallel test beam. The fringe pattern obtained is stored on a CCD for instance and analyzed by fringe analyzing procedures, which are described in Sect. 9.1.3.2. The most frequent first-order aberration types observed in optical systems are also shown schematically in Fig. 9.1.7, namely (a) for a perfect wavefront, no fringes can be seen, (b) shows a wavefront with defocus, (c) with astigmatisms, (d) with tilt, (e) with spherical aberration and defocus, (f) with coma or centering error.

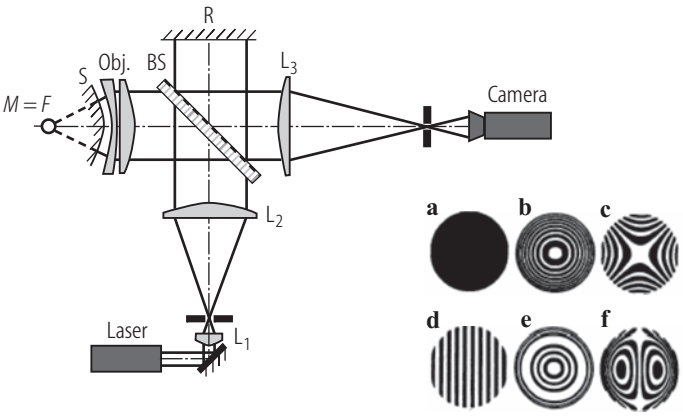

Fig. 9.1.7. Twyman–Green interferometer for testing optical systems with typical fringe patterns.

9.1.3.1.3 Fizeau interferometer

In the Fizeau interferometer one optical reference surface is compared with a test surface by placing them in close proximity and is therefore nearly a common path interferometer and very robust with respect to turbulence and vibration. Fringes of equal thickness between the reference and test surface are observed and analyzed. The Fizeau and the Twyman–Green interferometer are standard interferometers for optical testing. In Fig. 9.1.8 a Fizeau interferometer is shown.

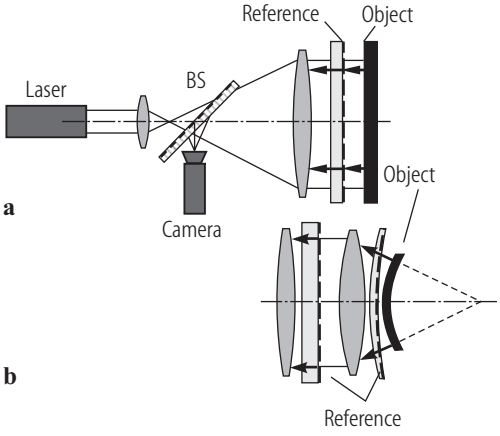

Fig. 9.1.8. Fizeau interferometer set-up (**a**) for testing a flat surface and (**b**) for testing a spherical surface.

A collimated plane wave is partly reflected back by the reference and the object surface, respectively. The optical path from the reference surface to the detector is nearly the same as for the corresponding object wave (after the beam splitter). For testing spherical surfaces the measuring wave is focused to the center of curvature of the spherical surface under test. The reference wave can either be reflected by a plane reference surface or alternatively by the last surface of the collimating lens system, an aplanatic surface, see Fig. 9.1.8b.

9.1.3.1.4 Mach–Zehnder interferometer

In the Mach–Zehnder interferometer reference and object waves are separated. The illuminating beam is divided by BS_1 into an object and reference beam and recombined again by BS_2 as shown in Fig. 9.1.9, where a configuration for an interference microscope system is shown. BS_1 and BS_2 are beam splitters, M_1 and M_2 are mirrors, and R is a compensating plate to compensate for the optical path of the substrate plate in the object path, O_1 and O_1' are identical microscope objectives. The Mach–Zehnder interferometer can be very useful to measure the refractive index

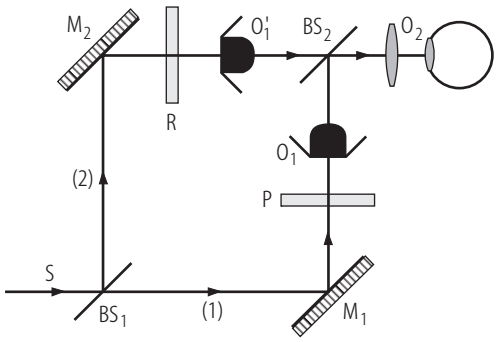

Fig. 9.1.9. Mach–Zehnder interference arrangement.

of air for instance, where the path in air is compared with the same geometrical path in a vacuum cell.

9.1.3.1.5 Shearing interferometry

Shearing interferometry has been used as a tool for many decades. Lasers, optical components, and elements can be tested quickly. In shearing interferometry, both wavefronts are derived from the system under test. The interference pattern occurs by shearing one wavefront with respect to the other; no reference is needed. It is a very robust technique with respect to mechanical disturbances like vibrations, since both interfering waves follow nearly the same optical path [64Mur, 92Mal, 03Har]. Radial shear is frequently used for testing rotationally symmetric wavefronts. Lateral shearing interferometers have found the most applications in optical testing. In lateral shearing diffractive gratings can be very attractive for separating and combining the beams [96Lei, 97Sch, 03Har]. Rotational and axial shearing can be used for particular applications.

9.1.3.1.6 Fabry–Perot interferometer

We have assumed in the discussion so far that only two beams interfere. There occur, however, situations where multiple beams are involved such as in a diffraction grating or plane-parallel plate. Considering the division of amplitudes in a plane-parallel plate, where the surfaces are coated to give higher reflectivity, the intensity for a specific wavelength decreases for multiple reflections. This effect used by a Fabry–Perot interferometer is an important example of a system which makes use of multiple beam interference. The interferometer can serve as a high-resolution spectrometer and as an optical resonator which is an essential component of a laser. The optical resonator consists of two highly reflective parallel surfaces separated by a distance d. The laser cavity is a Fabry–Perot consisting of the two separated plates or a single plane-parallel glass plate with highly reflecting coatings.

The performance of a Fabry–Perot cavity is described by the finesse. It is a measure of the number of resolvable spectral lines. It is defined as the ratio of the phase difference between adjacent fringes to the Full Width-Half Maximum (FWHM) of a single fringe. The finesse, F, depends strongly on the reflectivity R and can be written [87Bor]

$$F = \frac{\pi\sqrt{R}}{1-R} \,. \tag{9.1.22}$$

The finesse of a cavity with flat mirrors is limited by the flatness and parallelism of the mirrors and is about 30. For etalons consisting of two curved mirrors it can be up to 10000.

9.1.3.2 Quantitative electronic phase evaluation techniques

Increasing use of electronic phase measuring techniques for direct measurements of phase differences in interferometry with very high accuracy has led to a high acceptance of interferometry in industry. Traditional methods of recording and analyzing interference patterns have largely been replaced by electronic techniques. Photodetector arrays based on CCD (Charge Coupled Device) or CMOS (Complementary Metal Oxide Semiconductor) technology together with computer analysis lead to a fast interpretation of interference patterns [93Rob].

There are many techniques using computer-aided fringe analysis, only the most used are discussed here, namely:

– Fourier-transform technique,
– phase-shifting technique.

In Fig. 9.1.7 some interference patters of lens systems in a Twyman–Green set-up are shown. Fringe interpretation is required for a quantitative analysis.

For the Fourier-transform technique the fringes should not be closed. Sometimes they can be opened by introducing an additional tilt to be subtracted afterwards. For closed fringes the phase-shifting technique is most appropriate.

9.1.3.2.1 The Fourier-transform technique

For open fringes or fringe patterns that can be opened by the introduction of a tilt in order to generate an optical carrier the Fourier-transform technique as shown by Takeda [82Tak] is appropriate. No additional interaction with the interferometer is necessary. This spatial carrier is modulated by the local variation of the phase difference, $\phi_1 - \phi_2 = \Delta\phi$, between the two beams. The intensity of the interference pattern can be written, according to (9.1.9):

$$I(x,y) = a(x,y) + b(x,y)\cos(2\pi\beta_0 x + \Delta\phi(x,y)) \tag{9.1.23}$$

which can be expressed as

$$I(x,y) = a(x,y) + c(x,y)\exp(\mathrm{i}\,2\pi\beta_0\kappa) + c^*(x,y)\exp(-\mathrm{i}\,2\pi\beta_0\kappa)\ , \tag{9.1.24}$$

where $c(x,y) = \frac{1}{2}b(x,y)\exp(\mathrm{i}\,\Delta\phi)$. The Fourier transform of the intensity with respect to x is

$$I(\beta,y) = A(\beta,y) + C(\beta-\beta_0,y) + C^*(\beta+\beta_0,y)\ . \tag{9.1.25}$$

β is the spatial frequency in the x-direction and β_0 the carrier frequency which should be high in order to be able to separate the first from the zeroth order. One first order will be isolated and shifted back by β_0 to lead to $C(\beta,y)$. Its Fourier transform is $c(x,y)$ from which the phase difference at any point can be calculated, namely

$$\Delta\phi(x,y) = \arctan\left[\frac{\mathrm{Im}\{c(x,y)\}}{\mathrm{Re}\{c(x,y)\}}\right]\ . \tag{9.1.26}$$

The Fourier-transform method for fringe analysis is fast and needs no mechanical movements. However, closed fringes should be avoided in order to avoid ambiguity by the analysis. Fringe patterns can be opened by introducing additional tilts in the reference beam for instance. Ge et al., showed [01Ge] that the Fourier-transform technique can be extended to analyze closed fringes.

9.1.3.2.2 Fringe analysis by phase shifting

Phase-shifting techniques are mostly used for fringe analysis. For phase shifting the optical path difference is changed in one beam either continuously or in steps [74Bru, 82Doe, 91Cre, 92Gre, 93Sch, 03Har]. In the phase-shifting method the optical path difference between the reference and measuring beam can be changed by means of a mirror mounted on a piezoelectric element (PZT). Remember that in (9.1.10) we have three unknown, namely the mean intensity I_0, the contrast γ as well as the phase difference $\Delta\phi = \phi_1 - \phi_2$. At least 3 independent equations are needed [82Doe]. However, due to possible errors by the phase shifting [91Cre] more phase-shifted interference patterns are used. Algorithms using an averaging technique have been introduced successfully by Schwider [83Sch, 93Sch] for instance. The introduced phase shifts are typically $\pi/2$ each, therefore

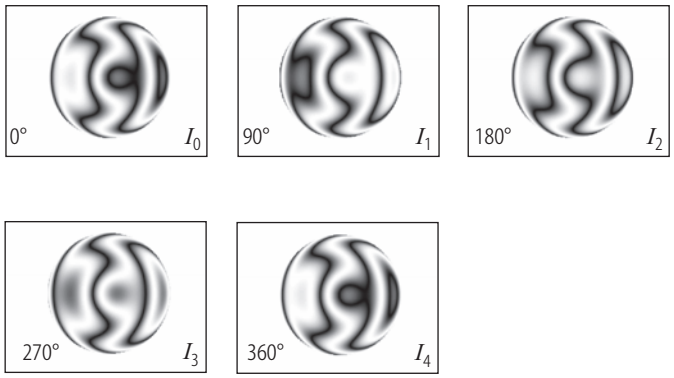

Fig. 9.1.10. Five phase-shifted interferograms with 4×90 degrees phase shifts introduced.

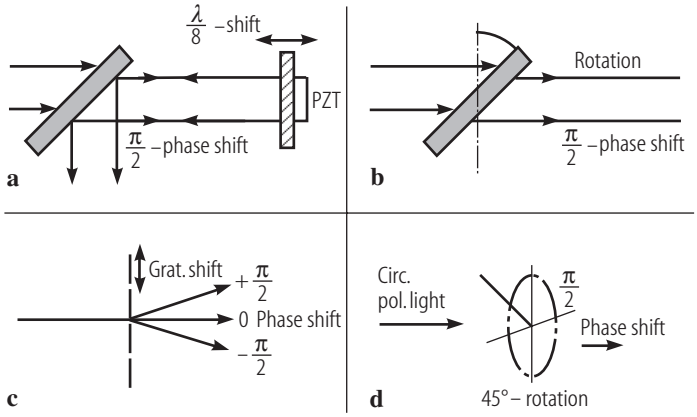

Fig. 9.1.11. Phase-shifting methods based on (**a**) a mirror on PZT, (**b**) a rotating plane-parallel plate, (**c**) a laterally shifted grating, (**d**) a rotating $\lambda/2$ polarizing plate. Additional methods for phase shifting are based on the change of wavelength. There are different methods to change the wavelength of a laser, e.g. changing the current of a diode laser or using a diode laser with an external cavity.

$$I_m = I_0 \left(1 + \gamma \cos\left\{\Delta\Phi + m\,\frac{\pi}{2}\right\}\right) \,, \tag{9.1.27}$$

where $m = 0, 1, 2, 3, 4, 5, \ldots$

The most commonly used algorithms for the calculation of the phases are the four- and five-frame intensity data recordings with phase shifts of $\pi/2$ between.

For 4 frames (3 phase shifts between) the phase difference $\Delta\phi$ is given by

$$\Delta\Phi = \arctan\left(\frac{I_3 - I_1}{I_0 - I_2}\right) \,. \tag{9.1.28}$$

Considering 5 frames (4 phase shifts between). The phase difference $\Delta\phi$ is given by

$$\Delta\phi = \arctan\left(\frac{2\,(I_1 - I_3)}{I_4 + I_0 - 2I_2}\right) \,. \tag{9.1.29}$$

In Fig. 9.1.10 five phase-shifted interferograms with 4×90 degrees phase shifts introduced are shown. In Fig. 9.1.11 several phase-shifting methods are depicted.

A problem in phase-shifting interferometry for optical testing is the sensitivity to the environment such as air turbulence and vibrations, leading to a reduced measuring accuracy. Simultaneous phase shifting is a solution to reduce the influence of the environment.

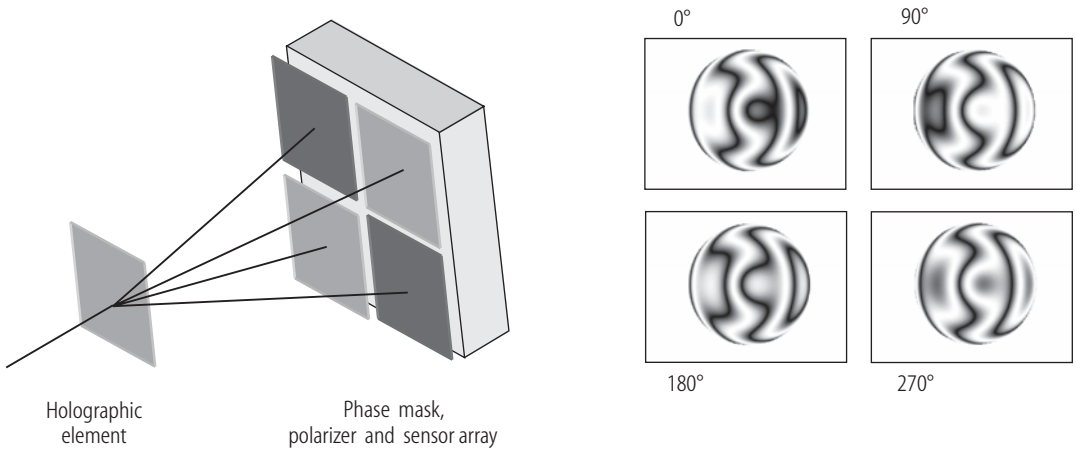

Fig. 9.1.12. Phase cam set-up.

In Fig. 9.1.12 a holographic optical element separates the same wavefront to be measured into 4 spatially separated parts [03Wya]. Each wavefront will be phase-shifted by phase plates with a multiple of 90 degrees phase shift (9.1.27). The phase-shifted interference patterns will be detected and analyzed with a single detector (CCD).

9.1.3.2.3 Phase-locked interferometry

In phase-locked interferometry the phase of a reference beam is modulated sinusoidally with a small amplitude. Different techniques can be used such as controlling the injection current of a laser diode or moving a mirror. The time-varying signal detected by a point detector is filtered to obtain a signal that contains the original signal and the introduced modulated phase signal of the reference [03Har]. The value of this signal is held at zero using a feedback loop.

9.1.4 Interferometry for surface metrology

9.1.4.1 Interferometry with extended range and reduced sensitivity: Oblique incidence interferometry

Oblique incidence on the object reduces the sensitivity by $1/(\cos \vartheta)$, but with extended measuring range, as shown in (9.1.13) and (9.1.30). There are different possibilities and arrangements to be considered such as prismatic or diffractive configurations. In the diffractive method in addition to the reduction of the sensitivity the object shape can be adapted by the holographic optical element designed for oblique incidence and shape adaptation.

9.1.4.1.1 Prismatic interferometer with oblique incidence

It was shown in Sect. 9.1.2.3 that the optical path difference of a plane incident wave reflected at the front and back surface, respectively, is proportional to the thickness d and $\cos \vartheta$, where ϑ is the incidence angle on the reflecting surface. The basic principle of oblique-incidence interferometry with a prism is shown in Fig. 9.1.13a, where the light of a plane wave is coupled into a glass

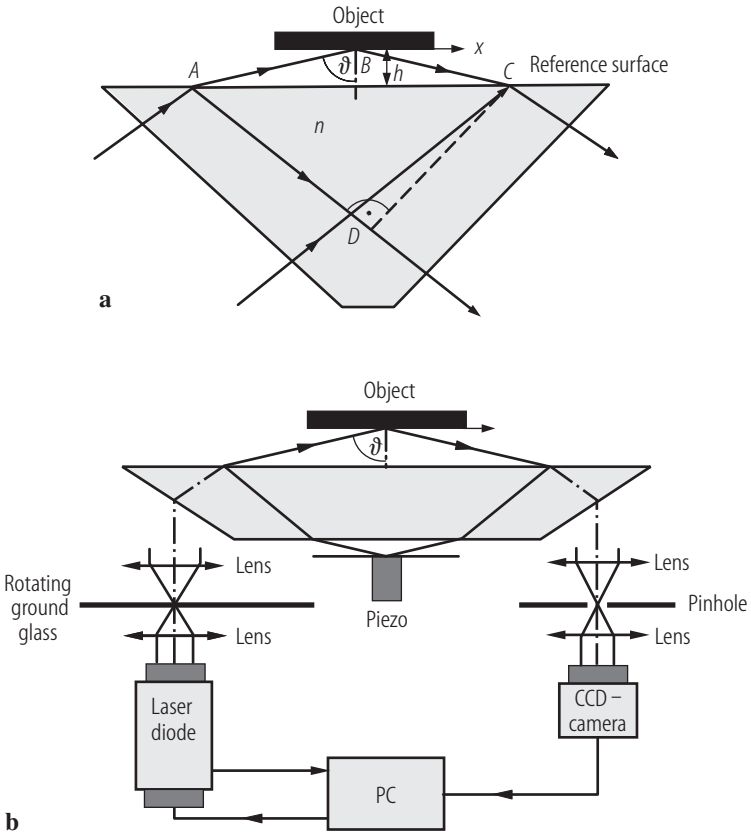

Fig. 9.1.13. Prism interferometer with oblique incidence. (**a**) Basic principle. (**b**) Typical arrangement.

prism with refractive index n. An air gap (refractive index is considered to be 1.0) is separating the perfect reference surface from the test surface; the separation is h. The optical path difference OPD between the reference and object beam is $\mathrm{OPD} = ABC - n\,AD = 2h\cos\vartheta$ and its phase is

$$\phi = 2\pi\,\frac{2\,h\,\cos\vartheta}{\lambda} = 2\pi\,\frac{2\,h}{\lambda_{\mathrm{eff}}}\,, \tag{9.1.30}$$

where $\lambda_{\mathrm{eff}} = \lambda/(\cos\vartheta)$. Therefore, fringes of equal thickness with a reduced sensitivity are obtained.

λ_{eff} can typically vary from 0.98 µm to 10 µm when ϑ varies from 50 to 86.4 degrees for $\lambda = 632.8$ nm.

For perfect reference and object surfaces a uniform fringe would be seen. Therefore, fringes obtained indicate defects $\Delta\,h(x)$ of the surface under test. The fringes will be analyzed as described in Sect. 9.1.3.2.

A typical prism interferometric arrangement we used is shown in Fig. 9.1.13b, where the reference mirror is not part of the prism. The reference mirror is moved for phase shifting by a piezo-element attached to it. In addition, it is slightly tilted to reduce unwanted reflections introducing some wedge or tilt fringes. By the arrangement the distortion in the interferogram can be reduced. A rotating ground glass reduces the spatial coherence in the time average and leads to a speckle reduction as will be discussed together with the speckle properties (Sect. 9.1.7). It should be noted that in addition to extend the measuring range for interferometric measurement, optically rougher surfaces can be measured as compared to interferometry with normal incidence. To extend the measuring range further synthetic wavelengths can be implemented by using two or more neighbor wavelengths of diode lasers [98Fra], see Sect. 9.1.4.2.

9.1.4.1.2 Grating interferometer with oblique incidence

For comparison a grating interferometer for oblique incidence is shown in Fig. 9.1.14. The CGH 1 (Computer-Generated Hologram) is splitting the incidence plane wave into the non-diffracted reference wave and the diffracted measuring wave. CGH 2 combines the reference wave and the wave coming from the object by diffracting the object wave in order to be parallel with the undiffracted reference wave in Fig. 9.1.14. Alternatively, the diffracted reference wave at CGH 2 could be combined with the undiffracted object wave. CGH 1 can, in addition, be used for shape adaptation. The phase variation due to the height variation is equivalent to that of the prism interferometer in (9.1.30) [86Sch].

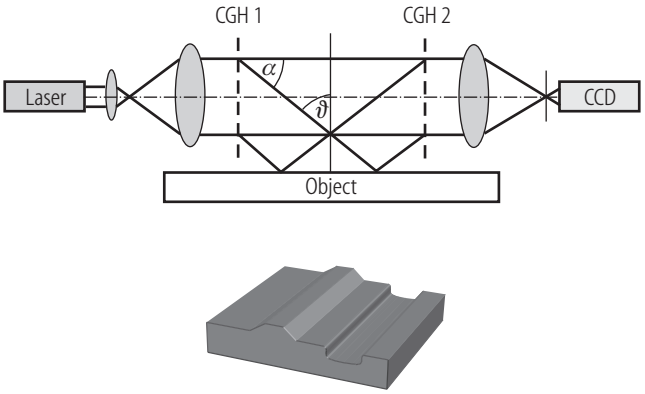

Fig. 9.1.14. Grating interferometer with oblique incidence.

9.1.4.2 Multiwavelength interferometry

To reduce the sensitivity of surface measurements an IR wavelength with $\lambda = 10.6$ μm can be used. Although the laser is available, high-resolution detectors with a comparable performance as obtained with CCDs in the visible are not yet available or too expensive. Two or more neighboring wavelengths can be used leading to beat wavelengths as will be seen by the two-wavelength heterodyne interferometry (Sect. 9.1.5). The beat wavelength for two wavelengths λ_1 and λ_2 is

$$\Lambda = \frac{\lambda_1 \lambda_2}{|\lambda_1 - \lambda_2|} \,. \tag{9.1.31}$$

As an example the interferograms of an aspheric surface are shown in Fig. 9.1.15a for $\lambda_1 = 822$ nm and in Fig. 9.1.15b for $\lambda_2 = 812$ nm. The synthetic wavelength is $\Lambda = 66.7$ μm. Fringes for the single wavelengths cannot be analyzed. By using both wavelengths, producing the synthetic wavelength, 3 fringes are observed as seen in Fig. 9.1.15c. The wavefront can be analyzed pixel by pixel, as shown in Fig. 9.1.15d from where the shape of the surface is obtained. For accurate measurements the interference pattern of a single wavelength can be used by taking into account (pixel-wise) the results obtained with the synthetic wavelength.

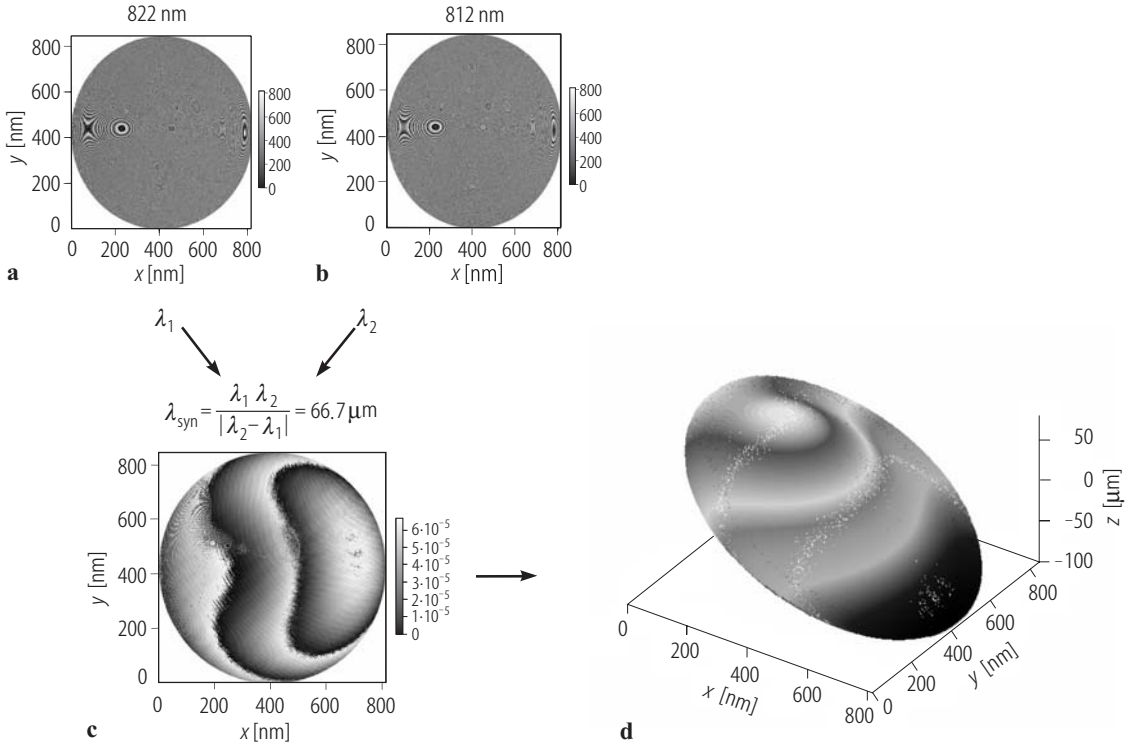

Fig. 9.1.15. Interferometry with 2 wavelengths, (**a**) $\lambda_1 = 822$ nm and (**b**) $\lambda_2 = 812$ nm; (**c**) is the interferogram obtained with the synthetic wavelength; (**d**) is the analyzed wavefront.

9.1.4.3 White-light interferometry

In white-light interferometry a short-coherence source is used. The $2\,\pi$ phase ambiguity discussed earlier can be overcome. However, the object needs to be scanned in depth. Starting at a point along the z-axis where the optical path is the same for the reference and test beam and moving the test surface along the z-axis in steps, the intensity by superposing the two interfering beams can be written:

$$I(z) = I_1 + I_2 + 2\sqrt{I_1 I_2}\;\; V(p)\,\cos\left(2\,\frac{\pi p}{\overline{\lambda}}\right)\;. \tag{9.1.32}$$

I_1 and I_2 are the independently acting intensities of the two beams, $V(p)$ is the visibility or coherence function (envelope of the fringes in Fig. 9.1.16b), p is the optical path difference. Interference can only be seen when the optical path difference between the reference path and the measuring path is smaller than the coherence length, which may be a few micrometers. Sources based on thermal white light, LEDs, multimode laser diodes, or super-luminescence diodes can be used. One way to measure the topography is to focus the microscope objective in order to obtain maximum visibility (zero optical path difference) for different object points by using a piezo-electric element. There are many algorithms for finding the coherence peaks (maximum fringe contrast). Combining the coherence-peak sensing and phase-shifting interferometry may provide the advantage of both methods, i.e. high precision and large dynamic range [90Kin, 92Dre].

There are different arrangements to be chosen, we concentrate on the Mirau arrangement only. The Mirau arrangement shown in Fig. 9.1.16a is a very robust set-up (nearly common path).

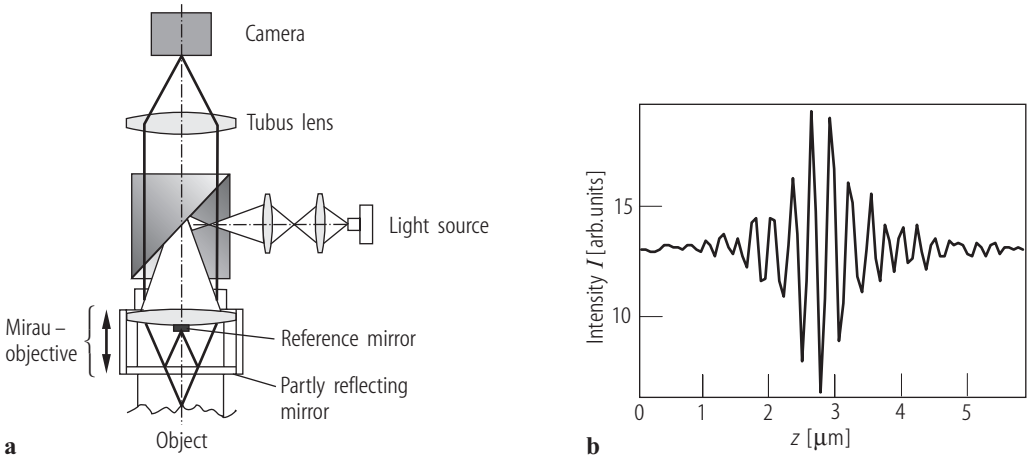

Fig. 9.1.16. (**a**) White-light interferometer arrangement according to Mirau and (**b**) the corresponding fringe pattern.

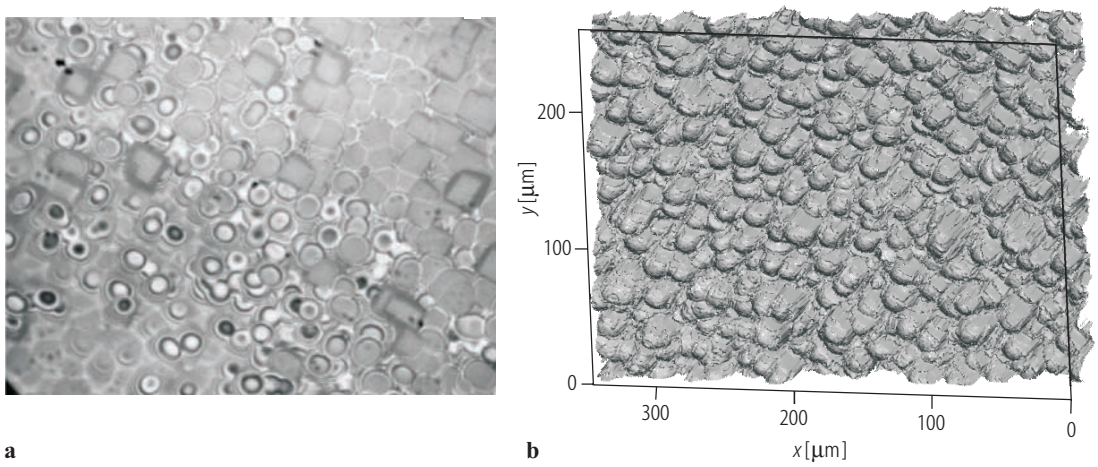

Fig. 9.1.17. (**a**) Interference fringes obtained with the white-light interference arrangement using a Mirau objective. The object was a coated Si waver. (**b**) Topography of the coated Si waver.

Figure 9.1.16b shows a typical fringe pattern by defocusing. For very high numerical aperture and extended working distance a Linnik arrangement is preferable. It is based on the Twyman–Green interferometer (Fig. 9.1.7), where two identical microscope objectives are used to focus the beams on the reference mirror as well as on the object, respectively.

In the Mirau set-up the illuminating wave is separated by the partly reflecting mirror into the reference and object beams and recombined after reflection at the mirror or test object, respectively, by the partly reflecting mirror.

In Fig. 9.1.17a as an example, results obtained by measuring a Si waver are shown. Interference fringes can only be seen when the Optical Path Difference (OPD) between reference and object wave is smaller than the coherence length. The maximum contrast occurs when the OPD is zero, hence the topography can be obtained; the topography of the Si waver is shown in Fig. 9.1.17b.

9.1.4.4 Polarization interferometry

The basic principle of the interferometric methods presented until now is the comparison of the object wave with an external reference. Typically this external reference is provided by the wavefront originating from a well characterized reference object. If such an external reference is not available or not preferable for technical reasons one can also compare the object wavefront with itself by dividing the wavefront and shifting one part by a certain amount. In dependence on the magnitude of this separation we talk about shearing interferometry with a differential or total shear. Picking up this idea of self-reference the vectorial character of the light field provides a further possibility of interferometry: namely the interferometric comparison of two orthogonal polarization states of the same wavefront originating from the object. This measurement principle is especially useful for linear microstructures with a size in the order of a wavelength. In this case we have a strong polarization dependence of the sample-light interaction and the polarization state divides in two eigenpolarizations, imprinted by the structure on the light field: One parallel to the line structures (TE-polarization) and one perpendicular (TM-polarization). A straightforward way to perform such interferometric measurements is using a liquid-crystal phase shifter with a following analyzer. The details of the method and its application to metrology of subwavelength structures can be found in [00Tot, 04Tiz].

In the following we will describe a related measurement technique in more detail that allows determining the complete partially coherent polarization state of the light field encoded in the coherence matrix. It falls back to classical principles of polarimetry.

The experimental set-up is based on a polarization microscope, operating in Deep UltraViolet (DUV) at 248 nm. Figure 9.1.18 shows the schematic set-up. As light source serves a xenon-mercury lamp, which is followed by a monochromator (λ = 248 nm, $\Delta\lambda$ = 5 nm). The freely accessible Koehler illumination set-up incorporates besides an adjustable aperture stop a polarization-state generator, consisting of a polarizer with a following rotating quarter-wave plate. By this means the illuminating polarization state can be chosen freely. For imaging we used a cemented DUV-objective 150 × /0.9. The post magnification is stepwise eligible between 1× and 6×. The polarization state emerging from the incoherently illuminated object is measured by the Polarizer-Sample-Compensator-Analyzer (PSCA) principle in combination with a Fourier-analytic evaluation procedure [93Col]. For this purpose a sequence of typically 8 images is captured for different uniformly distributed orientations of a quarter-wave plate followed by a fixed orientated analyzer. The pixel-wise evaluation of the image stack leads to a linear system of equations. The solution

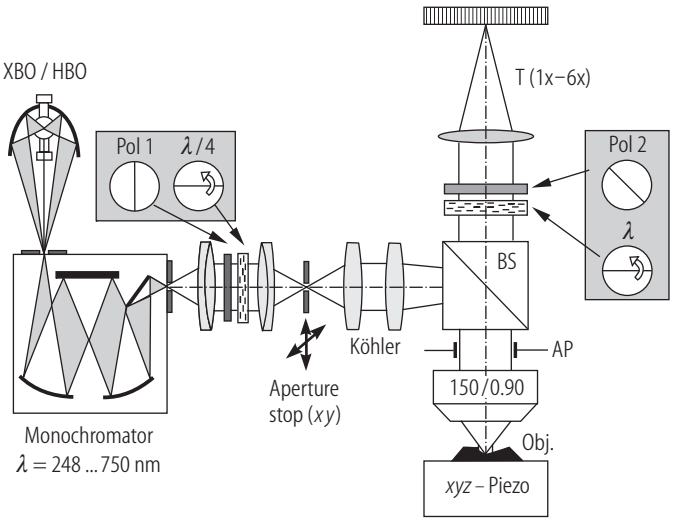

Fig. 9.1.18. Set-up for high-resolution polarimetry.

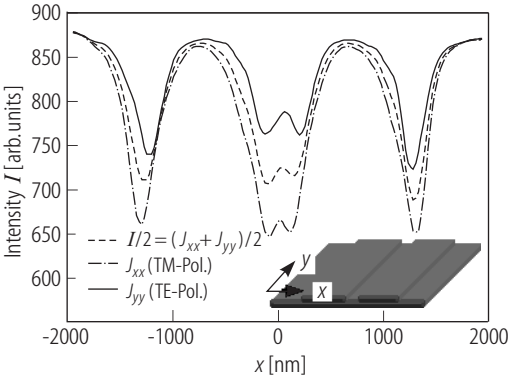

Fig. 9.1.19. Diagonal elements of the measured coherence matrix. The dependence of the contrast and the position of the intensity minima indicating the edge position with respect to the illuminating polarization state are clearly visible.

provides the 2D coherency matrix, which describes in the limit of high magnification a partially polarized light field completely.

The coherency matrix is the basis for determination of different quantities, valuable for precise quantitative image interpretation and evaluation. To these belong degree of coherence, degree of polarization, relative phase retardation etc. On the basis of this formalism polarization-induced interaction processes can be measured within a single measurement cycle. In the following, we give a measurement example, which demonstrates the validity of the method. The examined object consists of a beam-like structure of 160 nm height separated by a 330 nm wide groove. The illumination was linearly polarized under 45° relative to the structure's edges with the full numerical aperture of NA = 0.9. Figure 9.1.19 shows the diagonal elements of J as well as the overall intensity $I = J_{xx} + J_{yy}$ (divided by the factor of two for better comparison) along a cross section of the structure.

The direct comparison shows, that the different interaction behavior for both eigenpolarizations of the structure causes a conspicuous deviation in the corresponding intensity distributions. So, TM-polarization shows a stronger contrast in the intensity profile and more pronounced intensity minima in comparison to TE-polarization. This is caused by more efficient scattering at the structure edges for TM as in this case the electrical-field vector matches the physical boundary condition to be preferably perpendicular on the Si edges. The physical boundary condition also forces the tangential component of the electric field (i.e. TE-polarization) to be continuous, while the normal component (corresponding to TM-polarization) performs a jump at the surface border. This behavior results in a pushing effect of TE-polarized light away from the structure edges. This thesis is confirmed by the fact, that due to these effects the penetration of TE-polarized light in the groove (with dimensions in order of the wavelength) is strongly reduced and results in a further reduction of the contrast in comparison to singular edges. In TM-polarization, however, this effect is much less pronounced. The field displacement described above is also the reason for different positions of the intensity minima in TE- and TM-polarization. These minima are typically used for edge detection of pure phase objects. In the present case the positions are different in the order of about 50 nm. This means that a difference in linewidth measurement of about 100 nm occurs.

Besides the pure polarization-dependent intensity profile, represented by the diagonal elements of J, the nondiagonal elements of the coherency matrix can also be used for quantitative image interpretation. For this purpose we use the complex correlation factor of (9.1.20). It is a measure of the mutual correlation of the polarization states in x- and y-direction. It represents the different interaction behavior of the structure's eigenpolarizations and is localized in the optical image at structure details such as edges. Figure 9.1.20 (left) shows the relative phase retardation induced by the measured structure. It has the same physical origin as the different intensity profiles described above: While TM-polarized light propagates along the Si edge, TE-polarized light is pushed away from the edge and therefore is ahead in phase. Here also the effect is strengthened in the groove region. TE-polarization is more ahead on phase than at the singular edges due to the reduced pen-

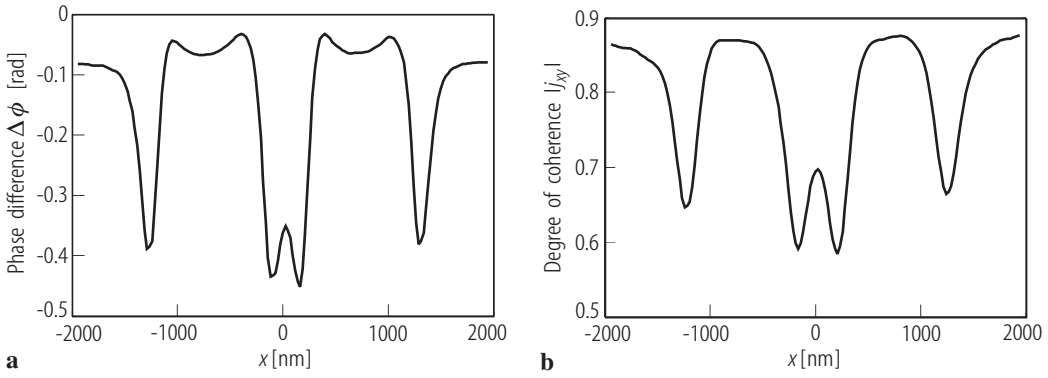

Fig. 9.1.20. Nondiagonal elements J_{xy} of the coherency matrix. Left: effective relative phase difference, right: degree of coherence.

etration capabilities into the groove. The right-hand side of Fig. 9.1.20 reveals a further important detail of polarization-dependent image formation. In the incoherently illuminating light field the polarization-dependent scattering process causes a strong reduction of mutual coherence, which is equal to the degree of polarization in the present case of 45°-orientated illumination (in this case J_{xx} and J_{yy} are equal). This means, that the minima in the intensity images are strongly linked to depolarization effects located at the structure edges.

9.1.5 Heterodyne interferometry for velocity and distance measurement

9.1.5.1 Principle of heterodyne interferometry

In heterodyne interferometry, a small frequency shift is introduced in one of the interferometer beams. It is a very powerful tool for the measurement of movements and velocities and distances by integrating the velocity. It is related to the well-known Doppler-shift measurement [71Dur]. The basic principle of heterodyne interferometry follows from the superposition of two waves A_1 and A_2, where one is frequency-shifted. It should be noted that perfect coherence is assumed. Describing the two waves as

$$A_1 = a_1 \cos(\omega_1 t + \Phi_1) \quad \text{and} \quad A_2 = a_2 \cos(\omega_2 t + \Phi_2(t)) \ ,$$

where $\Phi_2(t) = \Phi_2 \pm \dfrac{2\pi}{\lambda}\, 2\, v\,(t)\, t$, we obtain by superposing the two waves

$$I = |A_1 + A_2|^2 = |a_1|^2 + |a_2|^2 + 2a_1 a_2 \cos\left\{\Delta\omega\, t \pm \frac{2\pi}{\lambda}\, 2\, v\,(t)\, t + \Phi_1 - \Phi_2\right\} \ , \tag{9.1.33}$$

where Φ_1 and Φ_2 are constant, not time-dependent, phases of the amplitudes a_1 and a_2 of the two interfering beams. $v\,(t)$ is the velocity of the moving object, $\Delta\omega = \omega_2 - \omega_1 = 2\,\pi\,(f_2 - f_1)$.

There are different methods to introduce the frequency shift. Frequently an Acousto-Optical Modulator (AOM) is used, working at 40 or 80 MHz for instance [88Dae, 91Sod]. Because of its high working frequency it can be more convenient to carry out the analysis at a lower frequency. Therefore 2 acousto-optic modulators can be used with slightly different frequency shifts; hence for

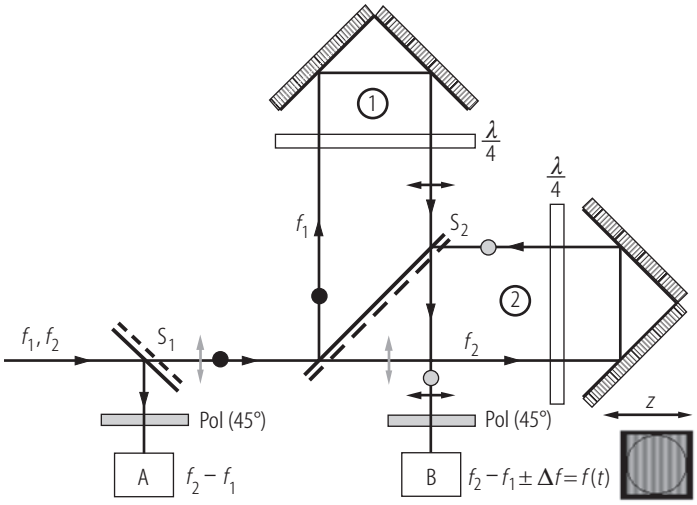

Fig. 9.1.21. Principle of the heterodyne interferometer with polarizing beam splitter.

the analysis the interferometer is working on the difference frequency, typically 100 kHz. Alternative phase-shifting methods are a rotating grating or a rotating $\lambda/4$ plate or the Zeeman splitting of a laser where a frequency shift is introduced in the laser cavity between two polarization directions. In Fig. 9.1.21 the principle of an arrangement used for distance measurement is shown. It is a Twyman–Green arrangement with retro reflectors instead of the plane mirrors for the reference and object beams in order to avoid the influence of small vibrations and tilts. The moving object leads to a frequency shift due to the time-varying phase $\Phi(z,t) = \Phi_0 + \Phi(t)$. The heterodyne frequency introduced by the interferometer is $f_2 - f_1$, the frequency shift introduced by the moving object is

$$\Delta f = \frac{2}{\lambda}\frac{\mathrm{d}\,z(t)}{\mathrm{d}\,t} = \pm\frac{2v}{\lambda}\,, \tag{9.1.34}$$

where $z(t)$ is the displacement variation projected onto the line of sight. Subtracting the known introduced frequency difference $f_2 - f_1$ from the measured frequency leads to Δf and hence to the speed of the movement. By integrating over the measuring time we deduce the distance z:

$$z = \frac{\lambda}{2}\int_{T_1}^{T_2} \Delta f\,\mathrm{d}\,t\,. \tag{9.1.35}$$

It is a very accurate incremental measuring principle used first in a commercial instrument by Hewlett Packard (HP). In the basic principle of the interferometer (Fig. 9.1.21) the two waves coming from the laser are polarized in two directions perpendicular to each other and have a slightly different frequency $f_2 - f_1$ (Zeeman splitting in the cavity). The polarizing beam splitter separates and recombines the two waves. A 90 degree rotation is required for the two waves to travel to the detector after reflection at the corner cubes (retro reflectors). Moving the retro reflector attached to the object leads to the frequency shift, from where the velocity respectively distance can be obtained. The method is frequently used for distance measurement in industrial environment. It is an accurate and robust but incremental method. An uncertainty of 10^6 can be achieved when a stabilized laser is used as light source. The measuring accuracy is limited by atmospheric disturbances. For accurate measurements, the atmospheric condition needs to be measured and its influence compensated.

9.1.5.2 Absolute heterodyne interferometry: Double heterodyne interferometry (DHI)

It has been pointed out that the heterodyne interferometer is an incremental interferometer, there is ambiguity whenever the optical path difference is equal or larger than the wavelength of the laser light used. To overcome some of the drawbacks of classical heterodyne interferometry, such as ambiguity but also its limitation to the use of highly polished surfaces only, a Double-Heterodyne-Interferometry (DHI) principle can be chosen [88Dae, 91Sod].

A Double Heterodyne Interferometer (DHI) can be considered to consist of two superposed heterodyne interferometers where each works on a slightly different wavelength. It can be shown that the two heterodyne interferometers lead to a beat frequency of the two wavelengths to be used for the distance measurement as discussed in [91Sod]. A developed double heterodyne interferometer will be discussed briefly.

The basic principle of an absolute heterodyne interferometer is shown in Fig. 9.1.22, where a high-frequency AOM is illuminated by two waves from a HeNe laser for instance with wavelengths λ_1 and λ_2, corresponding to the frequencies ν_1 and ν_2, where $\nu = c/\lambda$. The non-diffracted beams are focused onto the object under test by the lenses L_1 and L_2 after passing a Polarizing Beam Splitter (PBS) and a Quarter-Wave Plate (QWP) and will be combined with the reference after passing the PBS and the lens L_3 as well as a Half-Wave Plate (HWP). The heterodyne difference frequency is introduced by a Rotating Grating (RG) in the reference beam. The AOM is operated at a driver frequency f_d leading to two frequencies in the first-order diffracted beam, namely for λ_1 of $\nu_1 + f_\mathrm{d}$ and for λ_2 of $\nu_2 + f_\mathrm{d}$. The diffracted reference beams from the AOM traverse two adapted diffraction gratings G and RG. G has a high spatial frequency (600 lp/mm) and splits the two HeNe wavelengths in α_1 and α_2 (first diffraction order) leading to the difference $\Delta\alpha$. The second, a Rotating Grating (RG), compensates the diffraction angle difference $\alpha_2 - \alpha_1$ of the two reference beams with frequencies $\nu_1 + f_\mathrm{d}$ and $\nu_2 + f_2$ in such a way that the zeroth order of one is parallel to the diffracted first order, frequency-shifted by f_m. The first-order diffracted beams are frequency-shifted by the rotation of RG by f_m whereas the zeroth order is not. After RG the zeroth-order beam having a frequency $\nu_2 + f_\mathrm{d}$ and the first-order with a frequency $\nu_1 + f_\mathrm{d} + f_m$ are parallel, as well as the zeroth order with the frequency $\nu_1 + f_\mathrm{d}$ and the minus-first order with the frequency $\nu_2 + f_\mathrm{d} - f_m$, one pair is selected only. After superposition with the object wave the signal can be directly applied to a low-frequency phase meter (for example a two-channel lock-in amplifier). The reference for the lock-in amplifier was directly taken from the angle-encoder detector (square wave signal) output. The beat of the two heterodyne signals can be detected after demodulation and band-pass filtering (to remove the carrier) and neglecting a stochastic phase term in the carrier. The detected signal is:

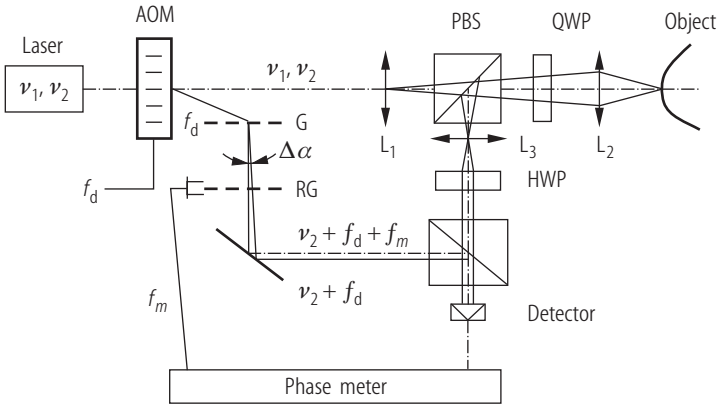

Fig. 9.1.22. Double heterodyne interferometer with rotational matched grating.

$$i\,(t) \propto I_0\,\cos\left[2\,\pi\,f_m\,t - \frac{2\,\pi\,\Delta z}{\Lambda}\right]\,, \tag{9.1.36}$$

where Δz is the optical path difference between object and reference paths,

$$\Lambda = \frac{\lambda_1\lambda_2}{|\lambda_1 - \lambda_2|} = \frac{c}{|\nu_1 - \nu_2|}\,. \tag{9.1.37}$$

Two-wavelength double heterodyne interferometry has proven to be a powerful tool for accurate interferometric measurements on smooth as well as on optically rough surfaces, providing that the roughness is slightly smaller than the depth resolution. For example by using a HeNe laser with the two wavelengths $\lambda_1 = 632.8$ nm and $\lambda_2 = 640.1$ nm, leading to $\Lambda = 55.5$ µm, and for a target distance of 6.5 mm, an accuracy of 0.3 µm was obtained. For high accuracy the single-wavelength heterodyne technique could be used with the same set-up. It should be noted that there are different set-ups for two-wavelength double heterodyne interferometry [88Dae, 91Sod, 96Tiz1, 96Tiz2, 97Tiz1].

9.1.6 Interferometry with adaptive optics

9.1.6.1 Interferometry with a null corrector

For testing polished optical plane or spherical surfaces to a shape accuracy of some nm RMS, interferometry is mainly applied. To measure or compare complicated wavefronts such as the shape of polished aspheric surfaces, holographic interferometry could be extremely useful. If a master optical component or optical system is available a hologram can be made of the wavefront produced by the component or system. The stored wavefront can be used to perform null tests of similar optical components or systems. If a master optical system is not available for making the hologram, a synthetic or Computer-Generated Hologram (CGH) can be produced to provide the reference wavefront. The CGH can be thought of as a binary representation of the ideal interferogram that would be produced by interference of the reference wavefront with the wavefront from a perfect aspheric surface for instance. In making the CGH the ray tracing needs to be done for the whole interferometer to determine the so-called aspheric wavefront at the hologram plane. Alternatively the compensator, also called null lens, can be designed as a refractive lens system, but in our days more frequently it is a diffractive element [72Wya, 85Doe].

Different interference arrangements can be used for testing polished optical surfaces, such as Fizeau, Twyman–Green, or Mach–Zehnder arrangement as discussed in Sect. 9.1.3. A Twyman–Green arrangement is shown in Fig. 9.1.23 with a CGH as null corrector for testing optical components and systems in transmission (Fig. 9.1.23a). The reflecting CGH is compensating the errors introduced by a refractive null lens or an element of an optical system to be tested. The use of the CGH for testing an aspheric surface is shown schematically in Fig. 9.1.23b. Frequently a lens system as used for testing spherical surfaces (Fig. 9.1.7 and Fig. 9.1.8) is added. It is useful in order to reduce the structure density of the CGH as shown in Fig. 9.1.23c. It should be noted that the null corrector in the test arm is designed in such a way that the rays hit the perfect aspheric surface under test perpendicular. For a perfect surface under test the reflected rays pass the null corrector again and are directed parallel to the incoming rays. The wave under test is combined with the reference wave, leading to interference patterns. If the measuring system is perfectly adapted only deviation from the perfectly designed aspheric shape leads to interference fringes to be analyzed in order to measure the shape deviation. However, care needs to be taken with respect to the positioning and alignment of the components of the test system and null corrector. A Fizeau set-up could equally well be used; the difference is mainly in the path of the reference beam.

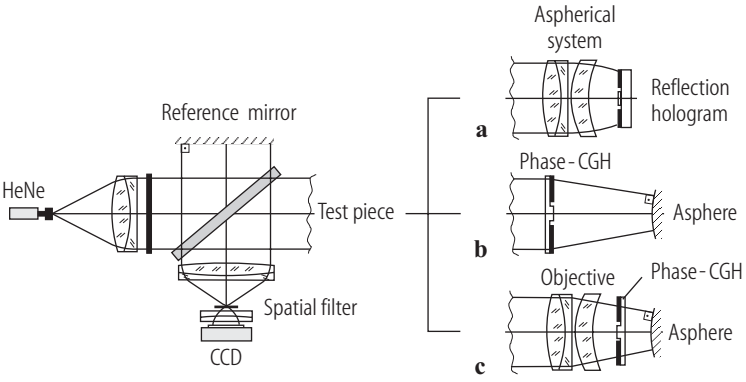

Fig. 9.1.23. (**a**) Interferometer based on the Twyman–Green principle with a CGH as null corrector for testing a system in transmission. Set-ups for testing a surface in reflection with a CGH (**b**) without and (**c**) with an additional collimating objective.

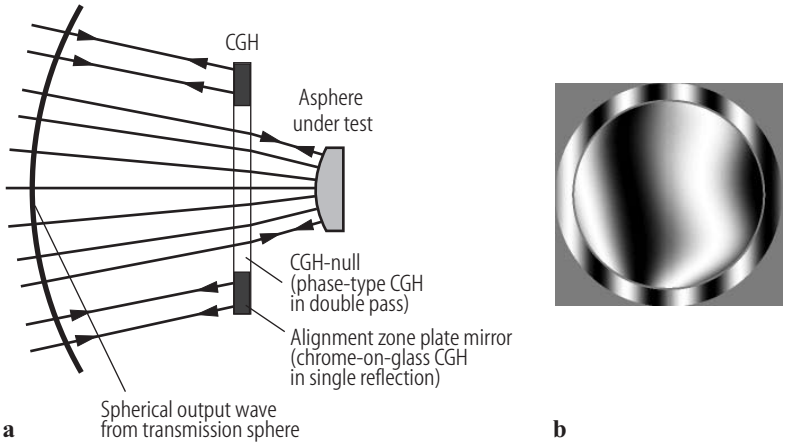

Fig. 9.1.24. (**a**) Multiple-function CGH with a ring-shaped reflection hologram (amplitude hologram) for adjustment and centering. The test hologram is a phase hologram. (**b**) Interference pattern of a not yet perfectly adjusted CGH.

For testing with null correctors, the null lens needs to be designed and manufactured with very high precision and tested. For a CGH as null corrector it can be an amplitude or phase element. To increase the diffraction efficiency phase holograms are used.

CGH's can be generated by using a photo plotter or by E-beam technology. As pointed out before, care needs to be taken in order to accurately adjust the CGH together with the components of the interferometer. Recently additional holograms for adjustments and centering were used [03Rei, 04Tiz]. In our case additional adjustment holograms are generated on the same substrate practically at the same time in order to reduce systematic errors in the testing and calibration procedure [03Rei]. In Fig. 9.1.24 the adjustment hologram is a reflecting amplitude hologram generated on the same substrate and made practically together with the CGH null system. The adjustment hologram shown schematically in Fig. 9.1.24a is placed at the periphery. In Fig. 9.1.24b an interference pattern of a not yet perfectly adjusted CGH is shown. The reference CGH makes the adjustment like positioning and centering of the hologram much simpler.

It should be noted that there are more parameters to describe an aspherical surface than a spherical. The degrees of freedom during alignment cause more types of corresponding wavefront aberrations than for spheres and centering tolerances for instance are more severe.

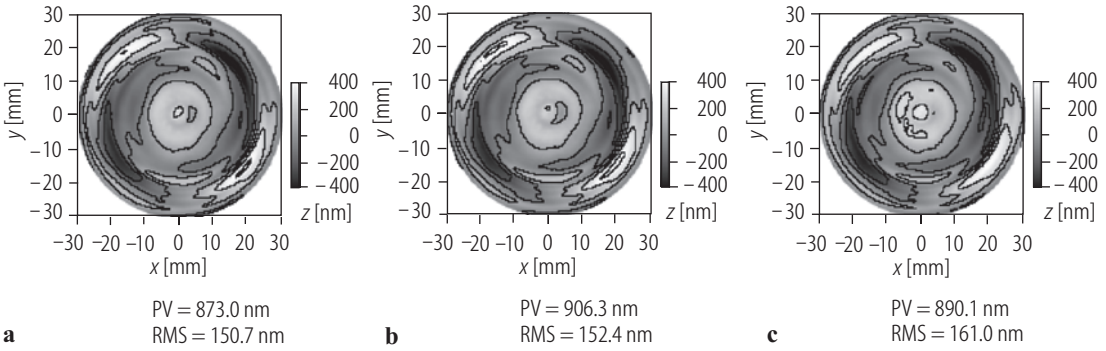

Fig. 9.1.25. Comparison of the results by measuring an aspheric surface with 3 different CGH's. (**a**) DI-CGH, (**b**) ITO-CGH, (**c**) Jenoptic-CGH.

After the interference patterns are obtained, the interference fringes are analyzed using one of the well-known techniques (Sect. 9.1.3.2.2) and the deviation from the perfect required shape of the aspheric surface is determined. Adjustment and calibration are very important for high-precision measurements [03Rei]. In Fig. 9.1.25 the results of an aspheric surface tested with three different CGH's produced from different laboratories with different techniques are shown. The manufacturers were (a) Diffraction International (DI), (b) ITO, University of Stuttgart, and (c) Jenoptic.

9.1.6.2 Adaptive optics with optical light modulator

Conventional adaptive optical systems for laser beam propagation or imaging are used in connection with astronomical telescopes, for instance. They consist of a wavefront sensor to detect the optical disturbance, a deformable mirror to correct the optical disturbance, and a computer to decode the sensor information for the active mirror. Interesting elements like Spatial Light Modulators (SLM's) as well as membrane mirrors are available today. The development of SLM's was driven by the data projectors, a consumer product. SLM's typically contain a matrix of individually addressable pixels of liquid-crystal cells or flip mirrors and more recently piston mirrors. Pixel sizes are on the order of tens of microns and therefore appropriate as active diffractive elements or flexible miniature masks. In consumer products the SLM's are mainly optimized for intensity modulation in transmission or reflection and not for phase modulation as it would be useful for some applications in wavefront shaping and analysis to be discussed, but progress has been made recently. For the analysis of the wavefront, Zernike polynomials are frequently used.

Wave aberrations limit the performance of optical systems. The aberration can be compensated using an appropriate hologram. At first, however, the wavefront needs to be determined. Interferometry or a Hartmann or Shack–Hartmann sensor could be appropriate. A method related to Young's double-slit experiment has been adapted together with an LCD as shown schematically in Fig. 9.1.26. The two "pinholes" generated by the LCD are moved across the pupil of the system under test. Interference between the two point sources occurs as in Young's experiment. The maximum of intensity appears, when the optical path difference, including the phase due to aberrations is a multiple of 2π. The fringe separation is inversely proportional to the separation of the pinholes.

The wavefront measurement obtained by analyzing the phase difference of the waves from the two pinholes carried out over the whole pupil is the base to produce the compensating hologram. The experimental set-up for wavefront measurement and wavefront correction is shown in Fig. 9.1.27a. The hologram generated is shown in Fig. 9.1.27b. The results obtained without and

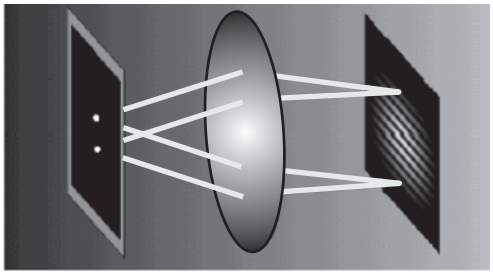

Fig. 9.1.26. Basic set-up for double-aperture interferometry using an LCD as mask. The light waves passing the two holes as in the Young experiment lead to an interference pattern in the focus plane. Figure 9.1.27b shows the measured wavefront aberrations.

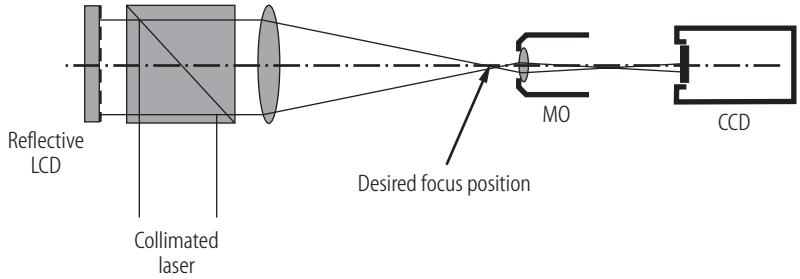

a

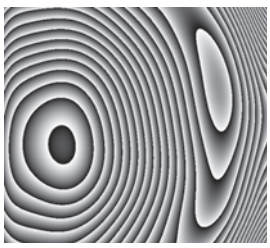

b

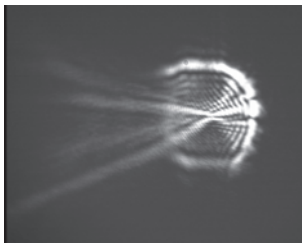

c

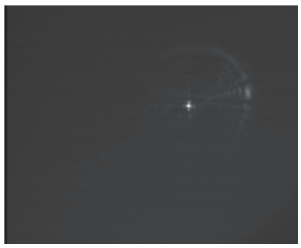

d

Fig. 9.1.27. (**a**) Experimental set-up for wavefront measurement and wavefront correction, based on the application of an LCD. (**b**) Phase distribution of the compensating hologram of the system with aberrations. (**c**) Point spread functions without and (**d**) with wavefront correction.

with the hologram introduced into the pupil plane are shown in Fig. 9.1.27c and Fig. 9.1.27d, respectively. It should be noted that the holograms were written in the LCD.

9.1.6.3 Adaptive optics with deformable membrane mirror

To correct wavefronts or adapt the wavefront to an aspheric surface a deformable membrane mirror can be useful as long as the local slope is not too high.

A typical membrane mirror consists of a thin, typically 1 μm thick, aluminum-coated silicon nitride membrane stretched over an array of electrodes. Due to the electrostatic forces, the membrane deforms by applying an electrostatic field between membrane and electrodes. Since the membrane deformation is smooth, the wavefront deformation is smooth, too.

The wavefront deformation depends on:

- the material constants and stress of the membrane,
- the gap between electrodes and membrane, and
- the voltage applied.

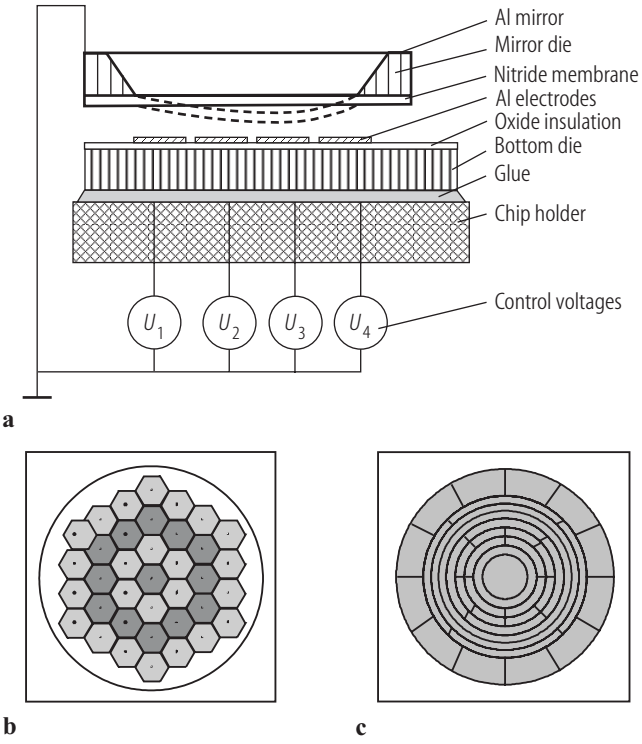

Fig. 9.1.28. (**a**) Principle of a membrane mirror. (**b**) Electrode configuration for hexagonal electrode structure and (**c**) for ring-shaped structure.

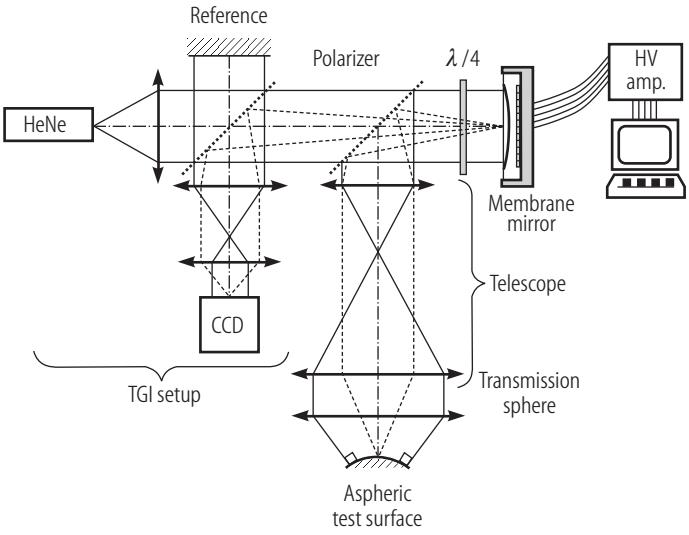

Fig. 9.1.29. Arrangement for testing an aspheric surface by the use of a membrane mirror to reduce the fringe density.

Material constants and stress depend on the fabrication process. The gap defines the maximum deflection. The deflection should not exceed 70% of the gap width [95Vdo]. For small deflections, the deflection is proportional to the square of the applied voltage. The basic principle of a membrane mirror is shown in Fig. 9.1.28a, two electrode configurations are shown in Fig. 9.1.28b and Fig. 9.1.28c with hexagonal and circular electrode arrangement, respectively.

In Fig. 9.1.29 a set-up of the dynamic "null lens" for testing an aspheric surface is integrated into a Twyman–Green interferometer set-up [04Pru]. The polarized beam in the test arm passes the polarizing beam splitter and the quarter-wave plate, is reflected back from the membrane mirror surface, and passes the retardation plate again. The quarter-wave plate in double pass rotates the polarization by 90 degree. The returning beam from the aspheric test surface passes the membrane

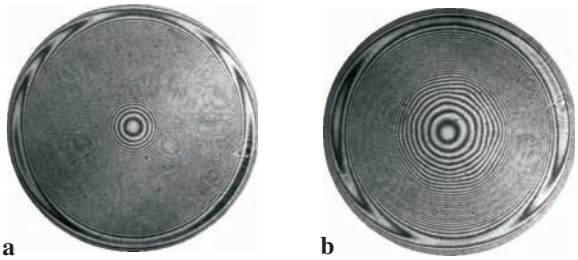

Fig. 9.1.30. Fringe pattern (**a**) without and (**b**) with partial wavefront compensation.

mirror again, which leads to a wavefront deformation that is four times the deformation of the membrane. For calibration of the membrane mirror the quarter-wave plate is rotated in order to have the reflected wavefront from the membrane mirror to be compared with the reference beam.

Membrane mirrors with a diameter up to 50 mm were used [95Vdo, 04Pru]; the experimental results shown in Fig. 9.1.30 were obtained with a diameter of 25 mm and a gap width of 70 µm. For driving the 37 channels of the mirror with a voltage up to 700 V a HV amplifier electronics was developed. Deflections up to 40 µm PV were obtained with a shape reproducibility of 50 nm. Figure 9.1.30a shows an interference pattern without and Fig. 9.1.30b with wave compensation.

9.1.6.4 Adaptive optics for optical stitching using dynamically tilted reference wave

For resolving high-density interference patterns a stitching technique could be used in order to select a small portion of the interference pattern at the time. By combining the different overlapping portions of the interferograms the whole wave field is obtained.

A very promising technique for a flexible wavefront measuring of otherwise not resolvable interference patterns is a flexible tilted reference or target wave [04Lie]. The technique is in the process of being developed for testing aspheric surfaces. The principle shown in Fig. 9.1.31 is based on a Twyman–Green interferometer. The main difference is a dynamically and flexibly tilted reference wave. The key elements are the addressable LCD together with the pinholes, defining a perfect spherical wave with a well defined selectable tilt angle. Details of the key element are shown in Fig. 9.1.32.

To explain the working principle a plane wave is falling obliquely on the LCD and is focused by micro lenses in the pinhole plane, but missing the pinholes all together. By generating a grating in the electrically addressed LC elements the first diffraction order deviates the selected beam (or beams) to pass the appropriate pinhole. The point source is now active and leads to a tilted reference wave after the collimating lens. Furthermore, a phase shift is introduced by laterally shifting the displayed grating proportional to the shift/grating period. The amplitude of the reference wave can be adapted by the diffraction efficiencies of the generated phase grating independently for the different point reference sources.

The LCD used in the described set-up was from CRL OPTO and had 1024×768 pixels with a pixel pitch of 36 µm. From the micro-lens array 70×70 LCD pixels were used in front of each micro lens. Gray-tone structures with 8 levels were produced by direct writing into photo resist with the photo plotter and transferred into fused silica substrate by dry etching: Reactive Ion Etching (RIE). The array of pinholes was etched into a black chromium layer as the absorbing layer with a separate mask. The micro-lens array works in its first diffraction order (Fig. 9.1.32).

On the back side of the 9 mm silica substrate were the pinholes generated by a separate mask aligned with respect to the existing micro-lens array. For the alignment of the pinholes alignment marks [01Gru] were printed onto the mask for the pinholes and the lenses simultaneously (self-imaging). 70×70 LCD pixels were used in front of each micro lens.

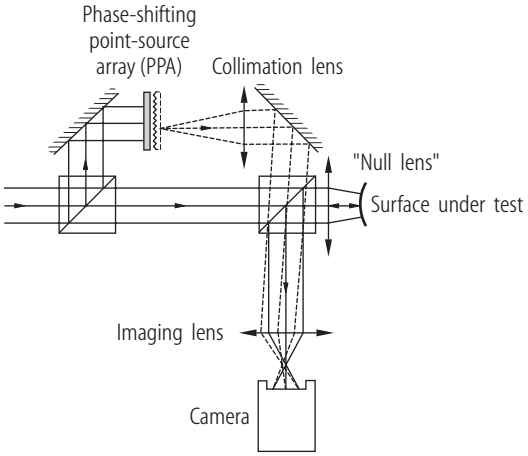

Fig. 9.1.31. Principles of dynamic reference beam.

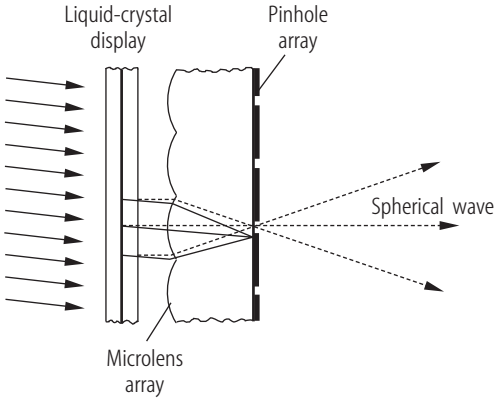

Fig. 9.1.32. Detail for generating the tilted reference wave and the phase shifting.

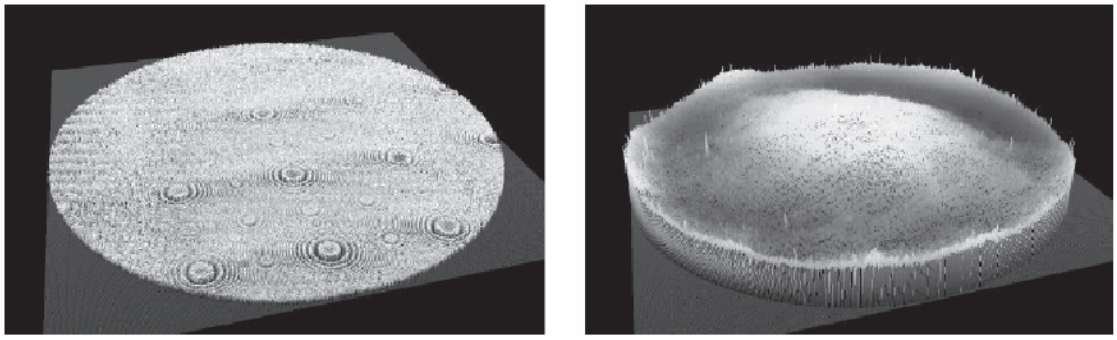

Fig. 9.1.33. Single-phase measurements of a defocused reference surface with 5×5 tilts (left), the result after unwrapping of 5×5 interferograms is shown (right).

Figure 9.1.33 shows first experimental results of the new stitching procedure. On the left are single-phase measurements of a test surface where different tilts were introduced into the reference beams, on the right is the unwrapped wavefront. In a comparison with simulated results after some calibration of the experimental set-up, the RMS value agreed by $\lambda/14$: The accuracy can be further improved. Alternatively, the object wave can be tilted (stitching) in the same way as demonstrated with the reference wave, which could even be more appropriate for practical applications.

9.1.7 Speckle pattern interferometry

The speckle phenomenon has long been familiar, but only the introduction of the laser, 1960, has brought attention and a deeper understanding. Laser speckles appear whenever an optically rough surface, with a roughness on the order of the wavelength or coarser, is illuminated with highly coherent light. The interference of the dephased, but coherent, secondary spherical wavelets originating from the surface results in granular patterns of intensity, commonly called speckle patterns. The path difference of these wavelets may be different by many wavelengths. Speckle

patterns appear everywhere, also in free space. Speckles can easily be seen when the wave field is intersected by a screen or a two-dimensional detector. Furthermore, the waves scattered from an optically rough surface have not only random phases but also random amplitudes. Analogous statistical phenomena are found in radio-wave propagation.

The speckle phenomenon is often a nuisance but there exist several techniques to reduce the graininess. Reducing the spatial coherence of the illumination [84McK] is one way, introducing a phase modulation or small vibration during the exposure is another way to reduce the speckle contrast in the time average. Multiple apertures can reduce the speckle contrast in the image plane as well.

Speckle techniques can be a powerful tool for studying surface properties of objects that are optically rough. In recent years, faster cameras with high resolution along with high memory and faster interfaces have revitalized the use of speckle techniques from its early stages of infancy to a tool very reliable for industrial tasks. The attractiveness of speckle methods lies in its ability to vary the sensitivity and range based both on speckle photography and speckle interferometry. Speckle techniques provide a large measurement range for in-plane and out-of-plane displacement, displacement derivative, and shape measurement. Another aspect of speckles is that they are generated due to the roughness of the object and therefore have also been used to measure roughness parameters.

Speckles and speckle photography have been described in many articles and books [70Arc, 72Tiz1, 72Tiz2, 75Ste, 78Erf, 79Fra, 80Tiz, 84McK, 89Jon, 93Sir, 93Yam, 94Oka, 94Sre, 01Leh, 01Ras1]. Speckle photography is based on the analysis of the speckle pairs resulting from the speckles before and after lateral displacement of the object or part of it.

By contrast, in speckle interferometry the phase variation of the speckles is analyzed; they should not move between the two exposures. Speckle interferometry is therefore used to detect small movements as is the case in holographic interferometry. Before concentrating on speckle applications some properties of speckles will be discussed.

9.1.7.1 Some properties of speckles

Speckle statistic is described in different books and papers [65Gol, 70Hop, 75Goo, 78Erf, 84Dai, 84Per, 89Jon, 01Leh]. Therefore some relevant results for its application in speckle interferometry will be summarized only. Scattered light has a grainy appearance when viewed in space. These speckles are termed objective speckle pattern. This graininess-like appearance can be observed on the image of the object as well. The speckles in the image are called subjective speckles (Fig. 9.1.34). The formation of speckles is random. The first-order statistics of a monochromatic polarized speckle

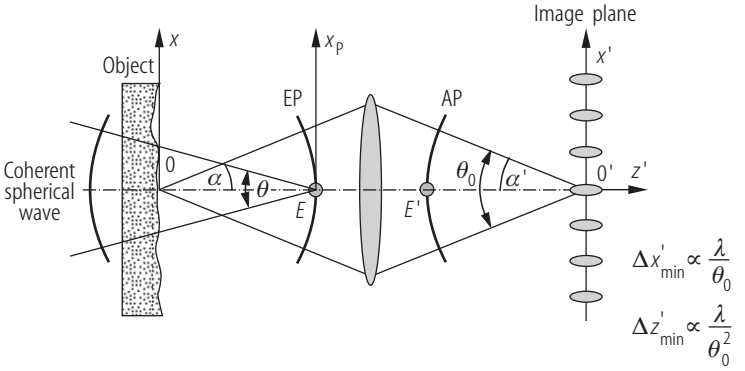

Fig. 9.1.34. Speckle formation and speckle size (for rectangular pupil).

deals with the probability density function of irradiance at a single point for an ensemble average of scatterers. The amplitude of the light wave at a given point of observation is considered to have contributions from different scattering regions of the surface. This pattern is identical to the classical pattern of random walk in a complex plane.

It is assumed that the scattering regions are statistically independent of each other and the phases are uniformly distributed between π and $-\pi$. It can be shown that the irradiance at a point for linearly polarized Gaussian speckles follows the negative exponential statistics which is given by

$$\begin{aligned} P_I(I) &= \frac{1}{\langle I\rangle}\,\exp\left(-\frac{I}{\langle I\rangle}\right)\,, \quad I \geq 0\,, \\ P_\phi(\phi) &= \frac{1}{2\,\pi}\,, \quad \phi \in [0, 2\,\pi]\,, \end{aligned} \tag{9.1.38}$$

where the mean intensity value of $\langle I\rangle$ is $2\sigma^2$, given by the variance [75Goo, 84Dai].

Consequently, we find that the most probable brightness of the speckle in a fully developed polarized speckle pattern is zero. The contrast of the speckle pattern is a ratio of the variance to the average irradiance. Using this definition, the contrast of a polarized speckle is found to be unity. Speckle patterns can be added both on an amplitude and intensity basis. In amplitude addition, there is no alteration in the statistics, except for a scaling factor. Addition on the intensity basis changes the statistics and the most probable brightness of the speckle is not zero anymore. The density function as a result of this is a sum of the simple decaying exponentials and the contrast of the speckle pattern assumes a minimum value of $1/\sqrt{2}$. The contrast of a sum of N speckle patterns on an intensity basis turns out to be $1/\sqrt{N}$.

For the description of other properties such as coarseness of the spatial structure of the speckle pattern or the spatial variation of amplitude and phase the second-order statistics needs to be considered as discussed by Goodman and Dainty [75Goo, 84Dai].

To describe the speckle size in an image-forming system let us consider the coherent image formation as a Fourier transform from the object to the entrance pupil, EP, and a second Fourier transform from the exit pupil, AP, to the image plane (Fig. 9.1.34) neglecting aberrations. α, α' are aperture angles, E, E' are the center of the pupils. If we put a screen or intensity recording detector in the entrance pupil, a speckle pattern as seen in the Fraunhofer plane would be observed (objective speckle), the mean speckle size and shape depends on the illuminated object area and shape and is basically given by the interference of the waves coming from the edge of the illuminated area. The lateral speckle size for an illuminated rectangular object area would be $\approx \lambda/\theta$, where θ is the total angle of the illuminated area in x-direction as seen from the middle of the entrance pupil (Fig. 9.1.34). For the image plane we consider the Fourier transformation of the random phase variation superposed on the object information on the entrance pupil and transferred to the exit pupil (neglecting aberrations) (Fig. 9.1.34). The information of the image is superposed to the speckle field (subjective speckles). The smallest subjective speckle size in the image plane (rectangular aperture) is $\Delta x'_{\min} \approx \lambda/\theta_0$, where θ_0 is the total aperture angle in the image space (Fig. 9.1.34). It turns out that it is also the dominant speckle size.

Assuming that we put a screen in the entrance pupil we would obtain the speckle size in the entrance pupil EP for a circular area of illumination

$$\Delta x_{\min} = 1.22\,\lambda\,\frac{z}{D} \tag{9.1.39a}$$

and in the image space

$$\Delta x'_{\min} = 1.22\,\lambda\,(1+M)F\,, \tag{9.1.39b}$$

where z is the distance from the illuminated object to the observation screen (the entrance pupil in Fig. 9.1.34). D is the diameter of the illumination area. For the image formation a circular aperture is considered, where F is the F-number of the image-forming system, M is the magnification, and

λ is the wavelength of light used. It should be noted that the diameter of the speckle in the image is inversely proportional to the aperture of the imaging system whereas the intensity of the speckle is directly proportional to the square of the diameter. The speckle in 3D space has the shape of a cigar; the length of the longitudinal speckle size for a circular aperture can be expressed as

$$\Delta z' = \frac{8\lambda}{{\theta_0}^2} \,. \tag{9.1.40}$$

For dark spots in a speckle pattern the intensity is zero as well as the phase in these regions, however, walking around the zero intensity regions one observes that the phase goes through a full $2\,\pi$ circle. These regions of phase jumps are called dislocations or phase singularities. It should also be noted that light scattered from most common objects does not necessarily retain the incident polarization state of the incident optical wave (Goodman [75Goo]).

9.1.7.2 Speckle applications

There are basically two important speckle application techniques for displacement-, deformation-, stress-, and vibration measurements, namely speckle photography and speckle pattern interferometry. Speckle photography is based on the displacement of the speckles due to an object displacement between two exposures [70Arc, 72Tiz1, 72Tiz2, 75Ste, 78Erf, 78Gre, 80Tiz, 93Yam, 94Oka, 94Sre, 99Sir]. Therefore two speckle patterns are recorded one before and one after deformation. There are different techniques such as the use of the principle of Young's experiment where the pairwise separated speckles stand for the pinholes in the Young experiment where the fringe spacing is inversely proportional to the spacing of the pinholes. To simplify let us consider one individual speckle before and after the object movement. Let us consider that the speckle moves with the object, which agrees for small movements. From Young's fringe separation the object displacement can be evaluated. Therefore the fringe spacing is inversely proportional to the speckle movement. Speckles are usually stored on photographic emulsion, before and after displacement. Instead of storing the speckles on photographic emulsions, photothermoplastic or photorefractive storage material or a CCD can be used [80Tiz, 94Oka]. Great progress has been made by using CCD storage devices and fast analysis. By contrast to speckle photography in speckle pattern interferometry the phase variation inside each speckle leads to the required information. We will concentrate on the application of speckle pattern interferometry and on digital holographic interferometry.

9.1.7.3 Speckle pattern interferometry for deformation measurements

In the previous Sects. 9.1.1 to 9.1.6 interferometry on optically polished surfaces was discussed. Speckle pattern interferometry, Electronic Speckle Pattern Interferometry (ESPI), and digital holography are whole-field interferometric techniques appropriate to study small deformations of objects with optically rough surfaces. The methods are based on interference of scattered light from the object superposed with a reference wave. The result is again a speckle pattern with randomly distributed speckles (with a random phase and amplitude) recorded on a CCD or CMOS chip, for instance. The changes in the object state due to displacement, deformation, or stress lead to phase changes within each speckle. A comparison with the phases of the speckles of the original object (without change) is the basis for ESPI [71But, 74Hun, 75Ste, 78But, 78Enn, 84Lok, 85Cre, 86Joe, 90Joe, 90Ker, 91Sir, 92Rod, 93Dav, 93Hun, 93Kau, 93Lok, 93Ped, 93Pry, 94Joe, 94Zou, 96Mei, 97Her, 97Hun, 97Ras1, 97Ras2, 98Ste, 01Kum, 01Ras2, 04Joe] and digital holography. In the ESPI method the speckle patterns before and after deformation of the object are recorded on a photoelectric detector and added or subtracted electronically with the appropriate software.

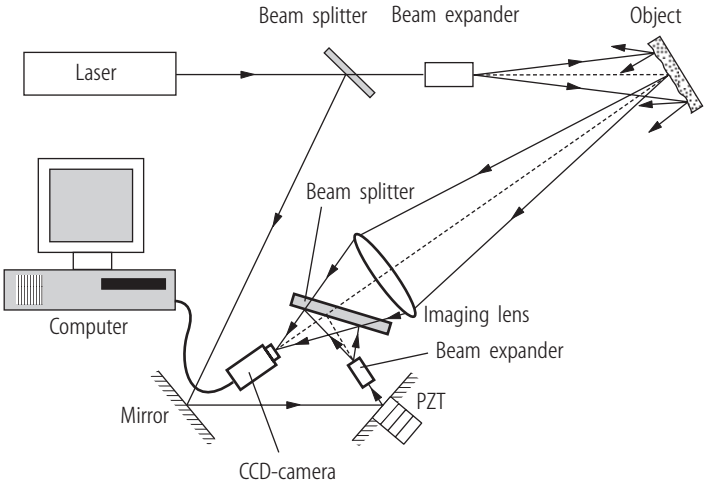

Fig. 9.1.35. Set-up for electronic speckle pattern interferometry.

A typical ESPI arrangement is presented in Fig. 9.1.35. A beam splitter separates the laser beam into an object and reference beam. The reference beam is reflected by a mirror mounted on a piezo-electric component (PZT) used for phase shifting, which is very useful for the analysis, as has been described in Sect. 9.1.3.2.

The resulting intensity in the recording plane (on a CCD or CMOS chip) of the overlapping waves at a given transverse point (x, y) for a given longitudinal position z and time t is given by

$$\begin{aligned} I(x,y,t) &= |U_{\mathrm{R}}(x,y,t) + U_{\mathrm{O}}(x,y,t)|^2 \\ &= |U_{\mathrm{R}}(x,y,t)|^2 + |U_{\mathrm{O}}(x,y,t)|^2 \\ &\quad + U_{\mathrm{R}}(x,y,t) \cdot U_{\mathrm{O}}^*(x,y,t) + U_{\mathrm{R}}^*(x,y,t) \cdot U_{\mathrm{O}}(x,y,t) \end{aligned} \tag{9.1.41}$$

and

$$I(x,y,t) = I_{\mathrm{R}}(x,y,t) + I_{\mathrm{O}}(x,y,t) + 2\sqrt{I_{\mathrm{R}}(x,y,t) I_{\mathrm{O}}(x,y,t)}\, \cos\left[\phi_{\mathrm{O}}(x,y,t) - \phi_{\mathrm{R}}(x,y,t)\right] , \tag{9.1.42}$$

where $U_{\mathrm{R}}(x,y,t)$, $U_{\mathrm{O}}(x,y,t)$, $\phi_{\mathrm{R}}(x,y,t)$, and $\phi_{\mathrm{O}}(x,y,t)$ are the complex amplitudes and phases of the reference and object beams, respectively, and I_{R}, I_{O} are the intensities of the reference and object beams. The term $\cos\left[\phi_{\mathrm{O}}(x,y,t) - \phi_{\mathrm{R}}(x,y,t)\right]$ denotes the modulation of the intensity of the combined speckle pattern. This term produces the resulting overall intensity variation in a transverse plane (x, y) at a given time for a time-varying signal. Equation (9.1.41) can be modified similarly to classical interferometry (Sect. 9.1.3, see (9.1.27)):

$$I(x,y,t) = I_{\mathrm{m}}(x,y,t)\left\{1 + V\cos\left[\Delta\phi(x,y,t)\right]\right\} , \tag{9.1.43}$$

where $I_{\mathrm{m}}(x,y,t)$ is the bias of the interference pattern and is equal to $I_{\mathrm{R}}(x,y,t) + I_{\mathrm{O}}(x,y,t)$, $\Delta\phi(x,y,t) = \phi_{\mathrm{O}}(x,y,t) - \phi_{\mathrm{R}}(x,y,t)$, and the so-called visibility is

$$V = \frac{2\sqrt{I_{\mathrm{R}}(x,y,t) I_{\mathrm{O}}(x,y,t)}}{I_{\mathrm{R}}(x,y,t) + I_{\mathrm{O}}(x,y,t)} .$$

Temperature-, mechanical-, or chemical perturbation will result in optical path length differences introduced between the two beams. These induced changes lead to a new speckle field to be generated whose characteristic statistical property is the same except for changes introduced by the perturbation. It was shown that in conventional interferometry an interferogram is observed, however, in speckle interferometry, the information is not directly revealed in one single state of

the superposing waves. To extract useful information from speckle interferometers we need (as in holographic interferometry or digital holographic interferometry, as will be shown in the next section) waves from a second state of the object. Comparing the two states of the superposing waves the information corresponding to the phase is revealed in form of fringes, called correlation fringes. Consequently, two states of the object can either be added or subtracted based on how the speckle patterns are recorded. Since the added intensities lead to fringes with low visibility, they are rarely used. Therefore the subtracted intensity of the two states will be given here only, namely:

$$I_2(x,y,t) - I_1(x,y,t) = I_{\mathrm{M}} \left|\cos\left(\Delta\phi_2(x,y,t)\right) - \cos\left(\Delta\phi_1(x,y,t)\right)\right| \ , \tag{9.1.44}$$

where I_{M} is the modulation of the combined speckle field. Here we have made the important assumption that only the phase has varied and that the individual speckle has not changed in position or shape. The above equation can be rewritten as

$$\begin{aligned} &|I_2(x,y,t) - I_1(x,y,t)| = \\ &\quad I_{\mathrm{M}} \left|\sin\left(\frac{\Delta\phi_2(x,y,t) + \Delta\phi_1(x,y,t)}{2}\right)\right| \left|\sin\left(\frac{\Delta\phi_2(x,y,t) - \Delta\phi_1(x,y,t)}{2}\right)\right| \ . \end{aligned} \tag{9.1.45}$$

Correlation fringes are obtained as a square of the difference and can be shown to be equal to

$$\left\langle |I_2(x,y,t) - I_1(x,y,t)|^2 \right\rangle = 2\left\langle {I_{\mathrm{M}}}^2 \right\rangle \sin^2\left(\frac{\Delta\phi_{12}(x,y,t)}{2}\right) \ , \tag{9.1.46}$$

where $\Delta\phi_{12}(x,y,t) = \Delta\phi_2(x,y,t) - \Delta\phi_1(x,y,t)$. Correlation fringes are obtained as a variation in intensity in the (x,y) plane and are related to the phase difference between the initial and the final states of the object. The fringes are modulated by speckles and even in the bright region one can observe dark regions caused by low modulation on the detector.

It should be noted that the speckle size discussed above needs to be adapted to the pixel size of the detector (e.g. a CCD), which can be achieved easily by choosing the aperture of the image-forming lens system as has been discussed in Sect. 9.1.7.1. Larger speckles reduce the spatial resolution; smaller speckles reduce the visibility because there would be more than one speckle in the pixel.

Variation of the incidence angle of the illumination or the wavelength or in special cases the refractive index of the object-surrounding medium between the two recordings leads to contour fringes for the object shape measurement [90Joe, 92Rod, 94Zou, 97Her, 01Ras2]. To obtain the derivative of surface movements, speckle shearing interferometry is a powerful tool for strain analysis [74Hun, 86Joe, 93Pry, 97Ras1, 98Ste].

Speckle interferometry has also been applied for vibration analysis, either in the time average or by stroboscopic illumination. Alternatively, illumination with short pulses, with pulse widths of 20 ns and pulse separations down to μs, is very useful for industrial applications. Two or multiple pulses can be applied which reduces the analysis of vibrating objects to two or multiple recordings of the speckle patterns [84Lok, 87Tyr, 93Lok, 93Ped].

Furthermore, the direction of illumination and observation determines the measurement sensitivity as well as the type of displacement the system will be sensitive to. Several novel techniques have been devised to visualize correlation fringes in speckle interferometry.

Figure 9.1.36 shows a result where the double-pulse speckle technique has been used for the measurement of vibrations.

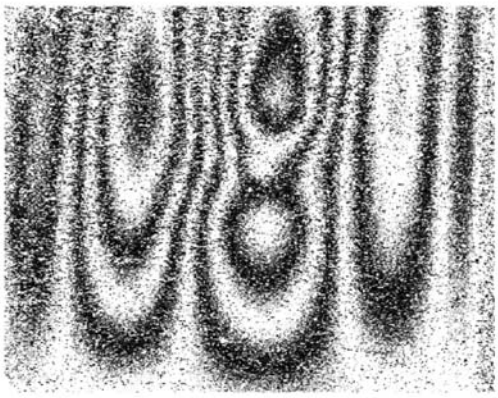

Fig. 9.1.36. The intensity pattern obtained by subtraction of two specklegrams of a vibrating cylindrical object. The frequency of vibration was 778 Hz and the pulse separation 200 μs.

9.1.7.4 Phase analysis in speckle interferometry

9.1.7.4.1 Phase analysis by phase stepping

The phase analysis occurs in the same way as in phase-stepping interferometry, a number of identical phase-stepped interference fringes are analyzed (see Sect. 9.1.3.2). A minimum of three measurements is required to solve for three unknowns in the interference equation. Typical phase steps introduced are 90 degrees, occasionally 120 degrees; in addition the analysis of more than three interferograms reduces possible errors occurring by the phase shifts introduced [85Cre, 90Ker, 93Kau] as in classical interferometry discussed in Sect. 9.1.3. Frequently the speckle fringes have to be processed in order to increase the visibility to achieve good phase plots. The accuracy of the method is limited by speckle distribution and speckle decorrelation. For the phase analysis in speckle interferometry we assume that the phase does not change appreciably over the time the three or four specklegrams are recorded. Other techniques like temporal phase steps or differentiating two interferograms that are phase-shifted by 90 degrees or the use of look-up tables are possible but not frequently used.

Several authors have discussed the phase-stepping technique for speckle pattern interferometry [85Cre, 90Ker, 93Kau]. To overcome the effect of random fluctuations in the speckle amplitude usually spatial and local averaging techniques are used to smooth the data. In this smoothing process a weighted averaging kernel $K(m, n)$ is used before the phase at a given pixel is evaluated. Wavelet transforms have been used to do signal processing on speckle interferometric fringes to reduce speckle noise by several authors [01Kum]. Alternative to this method is to perform temporal averaging of the speckles by collecting an independent series of identical interferograms except for the speckles, hence they are averaged by the summation.

9.1.7.4.2 Phase analysis by spatial phase shifting

In spatial phase shifting a known tilt is introduced by tilting the reference plane wave, for instance, in such way that the adjacent pixels on the CCD have an inherent phase difference of $\pi/2$. By analyzing the information on three or four adjacent pixels the phase at a given pixel can be evaluated. This procedure requires only one specklegram or one frame of the speckle pattern to extract the phase. The price to be paid is the loss in spatial resolution because the speckles have to extend over at least three CCD pixels if three phase-shifted specklegrams are used [97Bot].

9.1.7.4.3 Analysis of vibrating objects

Vibrating objects can be analyzed in a similar way as discussed when double-pulse technique is applied. In the case of vibrating objects where time-averaging techniques are used the fringes obtained are not cosinusoidal anymore, but lead to a zeroth-order Bessel function. Therefore, the analysis is not straightforward anymore. However, it is possible to make quantitative analysis using temporal phase stepping with time-averaged fringes. The speckle modulation is obtained by using the four-phase-step method [98Gre, 99Moo, 01Moo].

9.1.7.5 Temporal speckle pattern interferometry (TSPI)

For the analysis of dynamic phenomena the processing of the interference signals can be carried out in the temporal domain, instead of the spatial. In temporal phase evaluation procedures a series of phase maps are obtained as the object is gradually deformed developing complete information of the object deformation. In Temporal Speckle Pattern Interferometry (TSPI) the interference signal is analyzed in the temporal domain instead of the spatial [93Hun, 97Tiz2, 98Joe1, 98Joe2, 99Joe, 01Tiz]. If the temporal development of the interference signal at each pixel is investigated, the signal noise can be reduced, the calculation procedure is simplified, the accuracy improved, and the measuring range increased.

In TSPI, a point on the object is observed over time as the object is being continuously deformed or rotated or the wavelength changed continuously (Fig. 9.1.37). A bright speckle turns dark by a phase change of π.

The intensity modulation of the speckles thus obtained provides the temporal evolution related to the movement. By analyzing the time-dependent signal, object deformations ranging from few microns to few hundreds of microns or the shape surface from few hundred micrometers up to few centimeters can be measured.

A typical signal obtained is shown in Fig. 9.1.38. By Fourier transformation of the temporal

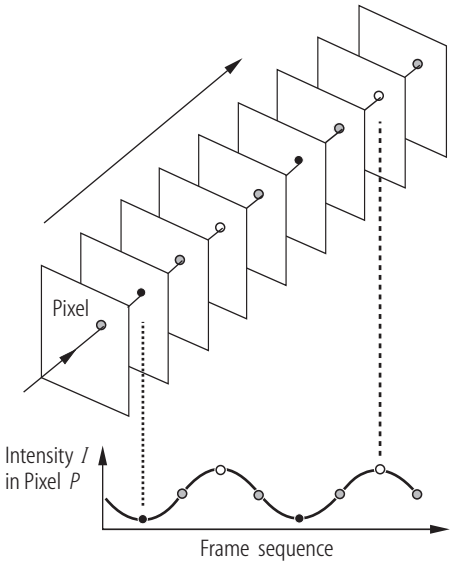

Fig. 9.1.37. Temporal evolution of a speckle on a CCD pixel.

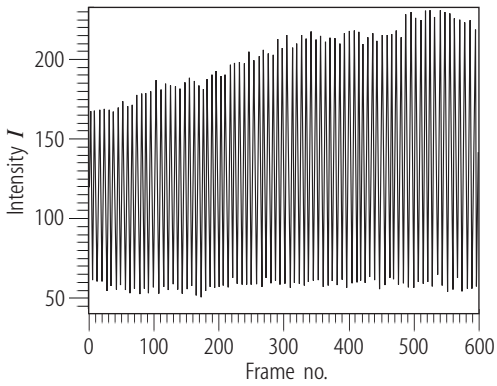

Fig. 9.1.38. Temporal intensity variation in a speckle.

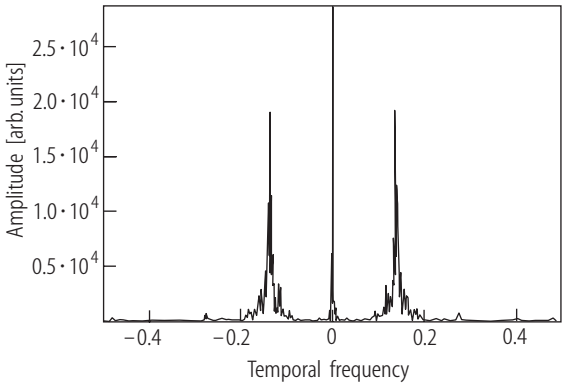

Fig. 9.1.39. Fourier spectrum of a temporal-varying speckle on a pixel.

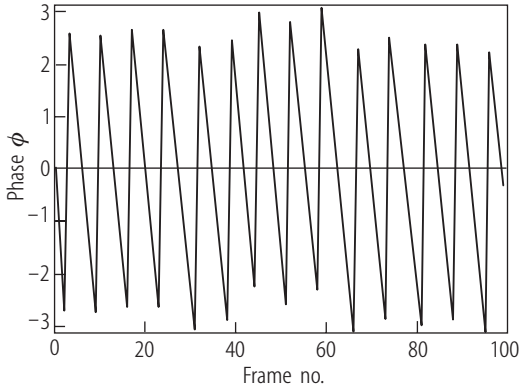

Fig. 9.1.40. Reconstruction of a side band of the spectrum in Fig. 9.1.39.

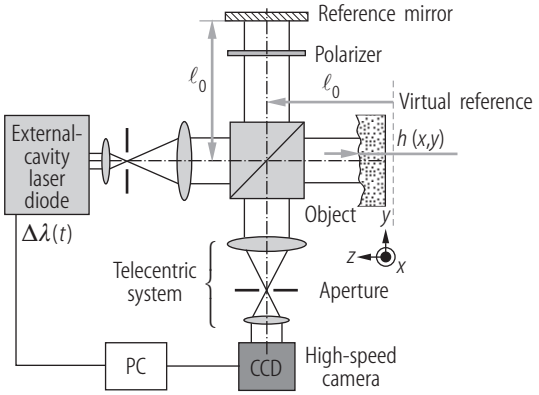

Fig. 9.1.41. Arrangement for recording of temporal speckle patterns for measuring shape and out-of-plane movements.

signal recorded in the series of frames, two bands are obtained on either side of a central peak in the Fourier spectrum as shown in Fig. 9.1.39 and one side band of the spectrum is filtered using a band-pass filter and shifted back to the origin. An inverse Fourier transform of the filtered spectrum portion leads to the raw phase that is then unwrapped to get the total phase at a given point (Fig. 9.1.40). The carrier frequency generated due to the object displacement or other changes should be large enough to separate the side bands from the central peak.

The object movement or deformation can be extracted using the Fourier-transformation method. This basic principle of TSPI can be extended to measure the object shape using variable wavelength or dual beam illumination, for in-plane motion detection [98Joe2]. Furthermore, the slope of the object deformation can be obtained by Temporal Fourier-Transform Speckle Pattern Shearing Interferometry (TSPSI) [97Ras1].

A TSPI arrangement is shown schematically in Fig. 9.1.41. The arrangement shown is basically a Twyman–Green set-up. One beam, after the beam splitter, illuminates a diffuse object and the other is reflected from a mirror forming the reference beam. The intensity of the reference beam is adjusted by introducing a polarizing system in order to adapt its brightness with respect to the object beam. The reference arm and the object arm are set to have arbitrary path lengths. A telecentric system is used to focus the object onto the sensor of a high-speed Charge-Coupled-Device (CCD) camera. In addition, the telecentric system insures the propagation axis of the beam from the mirror and the object to be collinear. It can be used for measuring the shape by varying the wavelength during the recording. With the same set-up out-of-plane deformation measurements can be carried out where the laser wavelength is kept constant and the time-varying optical path change due to object movement or time-varying out-of-plane deformation is studied.

For deformation measurements a He-Ne laser beam is expanded with a spatial filtering set-up and then collimated. The intensity of the interference signal observed at the sensor plane can be expressed as (see (9.1.43))

$$I(x,y,t) = I_0(x,y)\left\{1 + V(x,y)\,\cos\left[\phi_0(x,y) + \phi(x,y,t)\right]\right\}\ , \tag{9.1.47}$$

where I_0 is the mean intensity, V the visibility, $\phi_0(x,y)$ is the random phase of a speckle, and $\phi(x,y,t)$ is the position and time-dependent phase change introduced when an out-of-plane arrangement is used, see (9.1.50). For the shape measurement the height variation is measured as will be discussed in Sect. 9.1.7.5.1.

9.1.7.5.1 Shape measurement with TSPI by using time-varying wavelength change

For shape measurements either the wavelength is changed during exposure or the object is rotated in order to obtain a time-dependent phase variation leading to the shape information [98Joe1]. The wavelength change during exposure will be discussed only. Because the phase variation is analyzed, no mode hopping should occur during the wavelength change. The time-varying intensity due to the wavelength variation can be written in the same way as in (9.1.47), namely:

$$I(x,y,\lambda) = I_0(x,y)\left\{1 + V(x,y)\,\cos\left[\phi_0(x,y) + \phi(x,y,\lambda)\right]\right\}\ , \tag{9.1.48}$$

where $\phi(x,y,\lambda)$ is the phase variation due to the optical path difference in air, by assuming $n = 1.0$. For normal incidence of the illumination onto the object

$$\phi(x,y,\lambda) = \frac{4\,\pi\,h(x,y)}{\lambda(t)}\ , \tag{9.1.49}$$

where $h(x,y)$ is the height to be measured. The time-dependent wavelength variation $\lambda\,(t)$ will be discussed below.

9.1.7.5.2 Laser diode with external cavity for wavelength change

For the time-varying wavelength the variation of current or temperature in a semiconductor laser leads to a very small wavelength change without mode hopping ($\Delta\lambda \leq 0.3$ nm). To extend the range a laser diode with external cavity was chosen. The arrangements according to Littman/Metcalf and Littrow were investigated [01Tiz]. Both use a reflecting mirror to select the wavelength. The Littman/Metcalf set-up was chosen as shown in Fig. 9.1.42.

The grating diffracts the collimated wave, the -1st diffractive order is returned to the laser cavity by the wavelength-selecting mirror arranged to be in auto collimation, whereas the zeroth order is directed to the speckle interferometer. An anti-reflex coating is needed for the laser-diode exit mirror in order to activate the external cavity system. To avoid mode hopping care needs to be taken with respect to the selection of the wavelength and corresponding cavity length variation by choosing the exact position of the rotation point.

The method can be applied for shape measurements of polished as well as rough surfaces. As an example to demonstrate the principle a staircase made of steel sheets of 0.2 mm thickness was analyzed. The result is shown in Fig. 9.1.43.

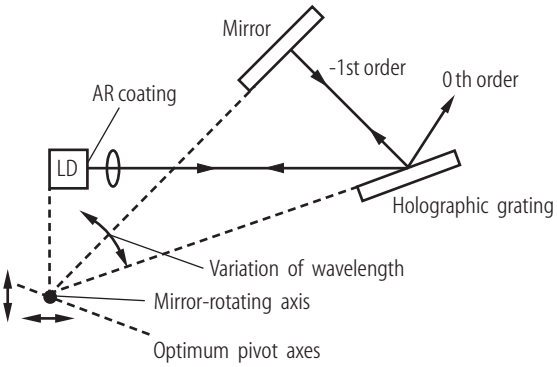

Fig. 9.1.42. Laser diode (LD) with external cavity according to Littman/Metcalf.

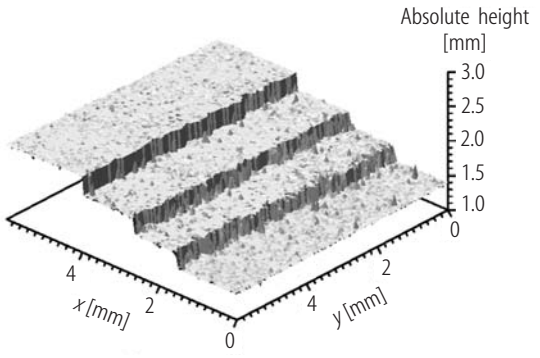

Fig. 9.1.43. TSPI-shape measurement of a staircase with continuous wavelength variation.

9.1.7.5.3 Application of TSPI for deformation measurement

Similar expressions can be derived for in-plane movement, object deformation- or the shape measurement of the object. The relationship for $\phi(x, y, t)$ depends on the set-up used [97Tiz2, 98Joe1, 98Joe2, 99Joe, 01Tiz]. For the out-of-plane arrangement we obtain for the phase:

$$\phi(x, y, t) = \frac{2\pi W(x, y, t)(1 + \cos\theta)}{\lambda} , \tag{9.1.50}$$

where θ is the angle of incidence of the object illumination, λ the wavelength, and $W(x, y, t)$ the deformation to be measured. The instantaneous temporal frequency f_i of the signal observed at a given point of the image of the object during t seconds of recording is

$$f_\mathrm{i}(x, y, t) = \frac{1}{2\pi\lambda} \frac{\partial\phi(x, y, t)}{\partial t} . \tag{9.1.51}$$

Thus the temporal frequency of the signal observed is dependent on the object deformation or its slope or the object height. A large number of frames of the speckle pattern is recorded sequentially as the object is being deformed. For each pixel we observe the speckle intensity variation over time, providing the pixel history. From the angle of the complex values of the resultant transform, the phase information is extracted. The initial phase is eliminated if the difference between the first frame and the last frame is taken. This procedure of obtaining the phase does not demand the displacement to be linear. For non-linear deformations the side bands broaden, demanding that the width of the band-pass filter used must be changed appropriately. This phase is then unwrapped as in phase-shifting interferometry thereby giving the total phase at that point. Obtaining the phase at all the points of the object provides the map of the time-dependent phase of the object deformation. The instantaneous angular frequency or the linear velocity generated during deformation of the object point is also determined. From these extrapolations the 3D plot of the object deformation is extracted. For in-plane measurement a two-beam illumination is used [98Joe2].

9.1.7.5.4 Deformation measurements by TSPI and digital holography, a comparison

For an experimental comparison an arrangement for digital holographic interferometry and TSPI was realized. The set-up is shown in Fig. 9.1.44. Object and reference beams were recorded on a high-speed CCD camera. For a direct comparison the exposures were the same but the analysis of the information was different. For the reason of simple data handling 200×200 image points

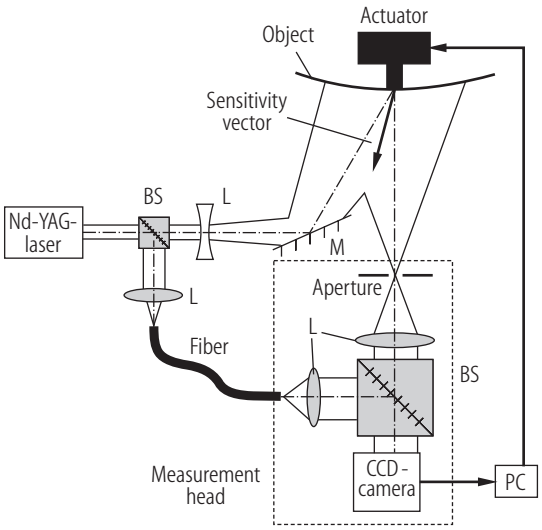

Fig. 9.1.44. Experimental set-up for deformation measurement by TSPI as well as by digital holography methods; BS: beam splitter, M: mirror, L: lenses.

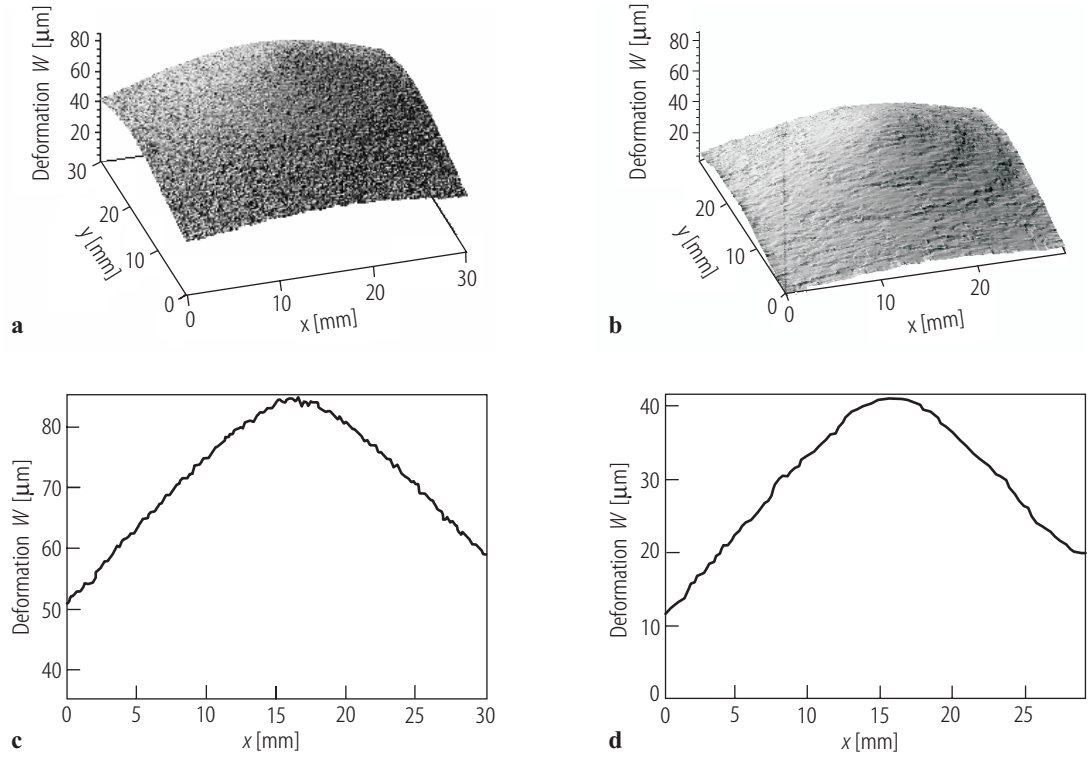

Fig. 9.1.45. A comparison of the results of the deformation measurement with TSPI and digital holography. (**a**) shows the result of TSPI and (**c**) a cross-section whereas (**b**) shows the result obtained by digital holography and (**d**) a cross-section.

were analyzed only and 1024 images were recorded for TSPI. For digital holography only every 25th image was analyzed leading to a deformation of 2 µm in the center. The results are shown in Fig. 9.1.45, where Fig. 9.1.45a shows the result of the TSPI analysis. It should be noted that in addition to the deformation the movement of the whole object during the measurements is observed with TSPI which is not the case in classical digital holographic interferometry as shown in Fig. 9.1.45b. Digital holographic interferometry will be discussed in Sect. 9.1.8. In addition a

cross-section of the deformations is shown for each method in turn in Fig. 9.1.45c, d. The body movement of 52 μm is seen clearly in Fig. 9.1.45c, measured with TSPI, which cannot be measured with a classical double-exposure digital holographic interferometry method. To obtain the sign information preliminary information can be used, or a more elaborate heterodyne technique can be used [01Tiz]. To measure deformation with temporal speckle patterns the temporal Hilbert-Transform (HT) method can also be applied for the phase analysis [03Mad].

9.1.7.5.5 Vibration measurement with TSPI

The evaluation of the time-dependent speckle modulation due to optical path-difference changes can be extended to vibration measurement [01Tiz]. For a sinusoidal signal evaluation with varying velocity: from zero at its reversal point, to maximum speed. For both cases we assume a harmonic vibration. For evaluation, the distance of two adjacent zero-velocity points is determined, giving half the mechanical time base.

Let us consider an experimental set-up like a Fizeau interferometer, see Fig. 9.1.46, where the object is harmonically vibrating. The periodical movement is expressed by:

$$z(t) = \hat{z} \cdot \sin\left(2\,\pi\, f_{\mathrm{mec}}\, t - \varphi_0\right) \ , \tag{9.1.52}$$

where f_{mec} is the frequency of mechanical oscillation and $\hat{z}$ its amplitude. The initial phase is represented by φ_0 and can be neglected. The instantaneous velocity $v(t)$ is given by the derivative of the mechanical path $z(t)$:

$$v(t) = \frac{\mathrm{d}\,z}{\mathrm{d}\,t} = 2\,\pi\, f_{\mathrm{mec}}\, \hat{z} \cdot \cos\left(2\,\pi\, f_{\mathrm{mec}}\, t\right) \ . \tag{9.1.53}$$

Using (9.1.48), the intensity at the detector can be written as

$$I(t) = I_0 \left(1 + V \cos\left\{\left(\frac{4\,\pi\,\hat{z}}{\lambda}\right) \sin\left(2\,\pi\, f_{\mathrm{mec}}\, t\right) - \varphi_0\right\}\right) \ . \tag{9.1.54}$$

The intensity at the detector is phase-modulated, the phase is

$$\varphi(t) = \frac{4\,\pi}{\lambda}\, z(t) \ , \tag{9.1.55}$$

written as frequency modulation of $v\,(t)$:

$$f(t) = \frac{2v(t)}{\lambda} = \frac{4\,\pi\, f_{\mathrm{mec}}}{\lambda}\ \hat{z} \cdot \cos\left(2\,\pi\, f_{\mathrm{mec}}\, t\right) \ , \tag{9.1.56}$$

where $f\,(t)$ is the instantaneous modulation frequency. In the analysis a frequency demodulation or a phase demodulation can be used in order to obtain the velocity or the optical path variation. FM-demodulation is done by FM/AM conversion for instance. Therefore the signal is differentiated and then low-pass-filtered in order to determine the envelope. An alternative demodulation method is the Fourier-based phase demodulation.

The experimental set-up is shown in Fig. 9.1.46. A fiber-optic arrangement is shown where the reference is reflected from the not coated fiber tip close to the object. For the experiment a loudspeaker was used as object with a sinusoidal frequency synthesizer at a frequency of 200 Hz. The fiber tip was put close to the vibrating membrane of the loudspeaker. The laser power of an InGaAs laser diode was 20 μW. The measuring time was 25 ms corresponding to 5000 samples.

Figure 9.1.47 shows the measurement of a vibration sequence recorded with the Fizeau set-up. The detector signal represents the frequency-encoded movement of the loudspeaker. The Fourier-based phase demodulation reconstructs the mechanical velocity which is shown in Fig. 9.1.48. The comparison to a high-precision vibrometer based on Doppler frequency measurement shows a good conformity including also higher harmonics. The noise is due to the small laser power and can be reduced when applying a band-pass or a special low-noise amplifier.

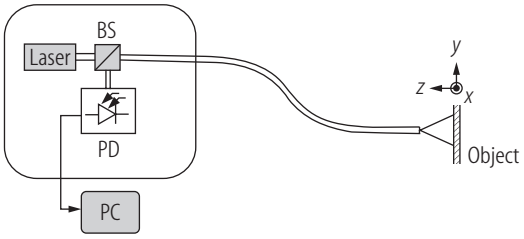

Fig. 9.1.46. Miniaturized Fizeau arrangement for vibration analysis with TSPI; the reference is the tip of the fiber.

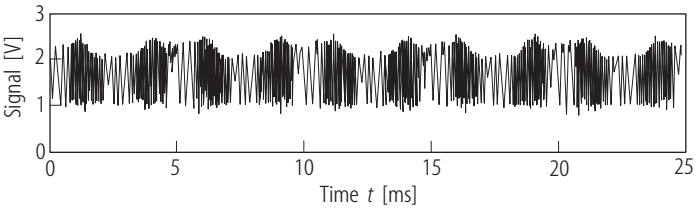

Fig. 9.1.47. Detector signal at an object point of the loudspeaker at 200 Hz.

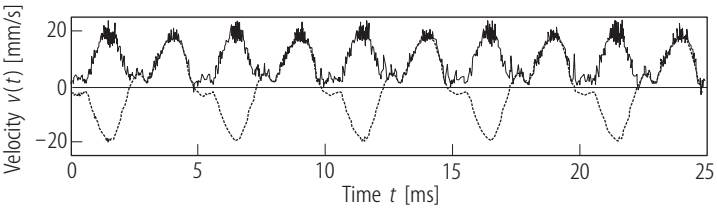

Fig. 9.1.48. Reconstructed mechanical velocity of the vibration analysis of the loudspeaker working at 200 Hz obtained with the Fizeau arrangement (upper part). For comparison a measurement with a high-performance vibrometer based on heterodyne technology is seen on the lower part (dashed line).

9.1.8 Holographic interferometry

9.1.8.1 Principle of holography

Holography is an interferometric technique for recording and reconstructing wavefronts. It was invented by Gabor in 1948 as an attempt to increase the resolution in electron microscopy [48Gab]. Gabor demonstrated that if a suitable coherent reference wave is present simultaneously with the light scattered from an object, the information about both the amplitude and phase of the object wave could be recorded, although the recording media only register the light intensity. The concept of holography was developed first as in-line arrangement. Gabor's holography was limited to film transparencies using a mercury arc lamp as the light source. His holograms contained distortions and an extraneous twin image.

For the next ten years, holography techniques and applications did not develop further until the invention of the laser 1960, whose coherent light was ideal for making holograms. By using a laser source, Leith and Upatnieks developed in 1962 the off-axis reference beam method which is most often used today [64Lei]. It permitted the making of holograms of solid objects by reflected light. Basically in holography, two coherent wavefronts, a reference and an object wave are recorded as an interference pattern as shown in Fig. 9.1.49. In classical holography the interference patterns are stored on high-resolution photographic emulsions, occasionally on photothermoplastic or photorefractive material. For the reconstruction a coherent wave, usually a laser, is used. Illuminating the hologram with a laser the physical reconstruction of the recorded wave field is performed as shown schematically in Fig. 9.1.50. By reconstructing the hologram the stored phase information

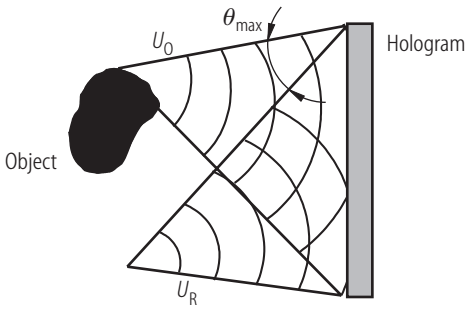

Fig. 9.1.49. Hologram recording.

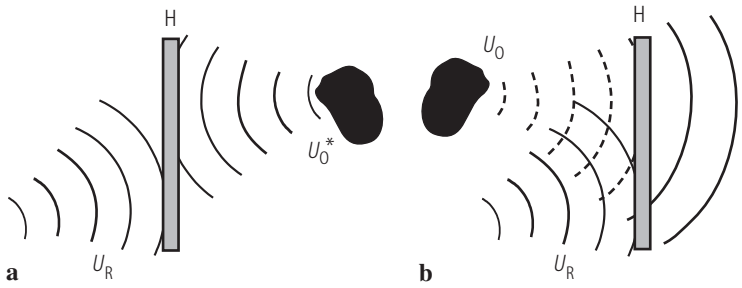

Fig. 9.1.50. Reconstruction obtained by illuminating the hologram with the original reference wave. The real (**a**) and the virtual (**b**) images are reconstructed. H is the hologram.

contains the information on the third dimension, the depth. Therefore a quasi three-dimensional reconstruction appears.

Leith's and Upatniek's off-axis arrangement [64Lei, 71Col, 74Cat, 79Sch, 79Ves, 89Jon, 96Kre] leads to a spatial separation of different reconstructions because the reconstructed waves and the zeroth order propagate in different directions. Two images are reconstructed to obtain a so-called virtual image (U_O) and a real image (U_O^*) as indicated schematically in Fig. 9.1.50. The virtual image is usually considered for holographic interferometry. Its position and size will be the same as for the original object when reference and reconstructing waves are the same with respect to geometry and wavelength.

There are different configurations for recording and reconstruction of the holograms [71Col, 79Sch, 79Ves, 96Kre], namely:

- Fresnel hologram,
- Fourier hologram,
- image-plane hologram.

A Fresnel hologram is the more general case where the recording is neither in the image nor Fourier plane of the object. Fourier holograms are recorded in the Fourier plane (focal plane of a lens). If the origin of the spherical reference wave is located in the plane of the object we call the hologram recorded a quasi-Fourier hologram. In image-plane holography, the image of the object is formed practically in the recording plane. Image-plane holograms are very convenient for digital holographic interferometry and speckle interferometry. An application of holography for optical engineering is holographic interferometry. The principles of holographic interferometry (Sect. 9.1.8.2) will be discussed mainly as introduction to the digital holographic interferometry (Sect. 9.1.8.4).

9.1.8.2 Principle of holographic interferometry

Holographic interferometry [79Sch, 79Ves, 96Kre] allows a comparison of different states of the object at different times. This technique uses the ability of the hologram to store two or more complex wavefronts by performing multiple exposures. The subsequent interference of these wave fields when they are reconstructed together produce a fringe pattern, from where the information of the deformations or change of refractive index of the object between the exposures can be obtained. There are different techniques to be used, namely:

- double-exposure technique,
- real-time technique,
- time-average technique.

In double-exposure holography two exposures are recorded (before and after deformation) on the storage material, a high-resolution photographic emulsion, for instance, and reconstructed together by illuminating with a laser.

In real-time holography the first hologram is recorded, the holographic plate is developed in its position or returned after development in exactly the same position. Because the precise repositioning is difficult, the holograms are frequently recorded on photothermoplastic or on photorefractive material. When the stored hologram is compared with the wavefront coming from the deformed object interference fringes, corresponding to the object deformation can be seen.

In the time-average technique [79Sch, 79Ves, 88Ste, 96Kre] the harmonic vibrations are recorded in the time average, i.e. during many vibration cycles.

We will concentrate on the double-exposure technique which is the most used for industrial applications. Two exposures are recorded on the hologram; one before and one after the deformation, for instance. The two recorded holograms are reconstructed together by illuminating the recorded holograms with a laser. In addition to the two reconstructed images of the object an interference pattern is superposed containing the information of the variation of the object between the two exposures. It should be noted that the deformation needs to be very small, in the range of a few micrometers. Hence the two reconstructed images are practically superposed. Furthermore, the virtual reconstructed image is usually analyzed as seen schematically in Fig. 9.1.51, but U_O and $\overline{U}_\mathrm{O}$ have a phase difference due to the deformation between the two exposures.

For a short analysis may U_R be the reference wave and U_O the object wave before and $\overline{U}_\mathrm{O}$ after deformation. To simplify the writing the coordinate dependences of U_R, U_O and $\overline{U}_\mathrm{O}$ are omitted.

Furthermore, may $U_\mathrm{O} = |U_\mathrm{O}| \exp(-\mathrm{i}\varphi)$ be the complex object wave before and $\overline{U}_\mathrm{O} = \left|\overline{U}_\mathrm{O}\right| \exp(-\mathrm{i}\overline{\varphi})$ after deformation. We assume $\left|\overline{U}_\mathrm{O}\right| \approx |U_\mathrm{O}|$.

The recording of a single hologram can be written in the form

$$I_1 = |U_\mathrm{R} + U_\mathrm{O}|^2 = |U_\mathrm{R}|^2 + |U_\mathrm{O}|^2 + U_\mathrm{R}^* U_\mathrm{O} + U_\mathrm{R} U_\mathrm{O}^* \tag{9.1.57}$$

(where * means complex-conjugate), and the recording of a double-exposed hologram is

$$\begin{aligned} I &= |U_\mathrm{R} + U_\mathrm{O}|^2 + \left|U_\mathrm{R} + \overline{U}_\mathrm{O}\right|^2 \\ &= 2\,|U_\mathrm{R}|^2 + |U_\mathrm{O}|^2 + \left|\overline{U}_\mathrm{O}\right|^2 + U_\mathrm{R}^* \left(U_\mathrm{O} + \overline{U}_\mathrm{O}\right) + U_\mathrm{R} \left(U_\mathrm{O}^* + \overline{U}_\mathrm{O}^*\right) . \end{aligned} \tag{9.1.58}$$

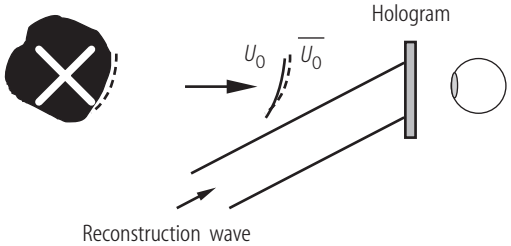

Fig. 9.1.51. Principle of a reconstruction of a double-exposed hologram.

After the hologram development and reconstruction by illuminating the hologram having a transmittance T with U_R we get

$$U_\mathrm{R}T = \text{const.} + \beta\tau\left[|U_\mathrm{R}|^2\left(U_\mathrm{O}+\overline{U}_\mathrm{O}\right)+U_\mathrm{R}U_\mathrm{R}\left(U_\mathrm{O}^*+\overline{U}_\mathrm{O}^*\right)\right] . \tag{9.1.59}$$

β and τ are parameters depending on the recording and developing process. τ is the exposure time and β the parameter of the photographic emulsion for instance. Due to the oblique incidence of the reference wave the different terms in (9.1.58) are spatially separated in the reconstructions. The intensity of the reconstructed wave of interest (virtual reconstruction) is given by

$$\begin{aligned} I_\mathrm{V} &= \left|\beta\tau\,|U_\mathrm{R}|^2\,|U_\mathrm{O}|\left(\mathrm{e}^{-\mathrm{i}\varphi}+\mathrm{e}^{-\mathrm{i}\overline{\varphi}}\right)\right|^2 \\ &= 2\left(\beta\tau\right)^2|U_\mathrm{R}|^4\,|U_\mathrm{O}|^2\left[1+\cos\left(\varphi-\overline{\varphi}\right)\right] . \end{aligned} \tag{9.1.60}$$

The additional phase difference $\varphi - \overline{\varphi}$ accounts for the deformation between the two exposures, leading to an interference pattern on the reconstructed images. From the analysis of the interference fringes and by knowing the geometrical data of the set-up and the object shape the 3D object deformation can be computed [71Col, 74Cat, 79Sch, 79Ves, 96Kre].

9.1.8.3 Digital holography

9.1.8.3.1 Principle of digital holography

In classical holography the interference patterns of the reference and object waves are stored on high-resolution photographic emulsions: for holographic interferometry occasionally on photothermoplastic or photorefractive material. For the reconstruction a coherent wave, usually a laser, is used.

The holographic process is time-consuming, particularly with respect to the development of the photographic film, making the method unsuited for industrial environments. In recent years optoelectronic recording devices like CCD or CMOS cameras have become an attractive alternative to photographic film, photothermoplastic or photorefractive crystals as recording media in holography. The time-consuming wet processing of photographic film is avoided and the physical reconstruction of holograms can be replaced by numerical reconstruction using a computer, normally an ordinary PC. One disadvantage of using CCD sensors for hologram recording is, however, the relatively low spatial resolution, compared to that of photographic material. The limitation in spatial resolution is a problem but the technology is improving further. The enormous progress in the performance of computers and increase in the computer capacity is very favorable for digital holography.

The problem of recording holograms on low-resolution media has been discussed in many books and publications since people first begun to record holograms [71Col, 74Cat, 94Sch, 95Ped, 96Sch]. Particle size and position measurements were based on digital reconstruction [97Ada]. Different holographic recording arrangement as in classical holography can be applied. The off-axis hologram arrangement using a point source (P) as a reference can be used (Fig. 9.1.49). The intensity of the interference between the reference (U_R) and the object (U_O) waves is given by (9.1.57). The maximum spatial frequency that can be recorded is limited by the resolution of the recording medium. To record a hologram of the entire object, the resolution must be sufficient to resolve the fringes formed by the reference wave and the wave from the object point farthest from the reference point. If θ_max is the maximal angle between the object and the reference beam (Fig. 9.1.49), the maximal spatial frequency f_max in the hologram is:

$$f_\mathrm{max} = \frac{2}{\lambda}\sin\left[\frac{\theta_\mathrm{max}}{2}\right] , \tag{9.1.61}$$

where λ is the wavelength of the laser light used for the recording. Consider that the intensity described by (9.1.57) is recorded on a two-dimensional array of sensors ($M \times N$ cells) of cell dimension $\Delta x \times \Delta y$. For the recording, in most cases a CCD sensor is used, but technology is progressing and a CMOS sensor may be used in future. The discretized intensity recorded by the sensor can thus be written in the form $I_H(m\Delta x, n\Delta y)$, where n and m are integer numbers. For the most common case of equidistant cells, we have $\Delta x = \Delta y = \Delta$. From the sampling theorem (see e.g. [96Goo]) it is necessary to have at least two sampled points for each fringe, therefore the maximum spatial frequency which can be recorded is $f_{max} = 1/(2\Delta)$. The interference fringes obtained between the light coming from the object and the reference should have a period greater than 2Δ.

There are different types of digital holograms as in classical holography [96Kre], namely Fresnel, Fourier, and image-plane holograms. Furthermore, there are in-line and off-axis holograms, as in classical holography. For off-axis holograms the separation of the reconstructed images is simpler even though the reconstruction occurs by computer and not physically as described above. We will concentrate now on off-axis digital holography. A Fresnel hologram is the more general case where the recording is neither in the image nor Fourier plane of the object. If the origin of a spherical reference wave is located in the plane of the object we call the hologram a quasi-Fourier hologram. Image-plane holograms are very convenient for digital holographic interferometry. The recording is therefore very similar to ESPI recording (Sect. 9.1.7).

The electronic recording device is considered as a two-dimensional (thin) hologram (Fig. 9.1.49). It is possible that electronic digital devices could be developed in the future where even volume holograms can be recorded and reconstructed digitally. We will restrict our discussion to holograms that can be digitized with currently available devices.

9.1.8.3.2 Configurations for recording and reconstruction of digital holograms

Holograms may be classified according to the geometry used for the recording and reconstruction. Quasi-Fourier, Fresnel, image-plane, and in-line and off-axis holograms will be described together with the digital reconstruction. All these different configurations can be used for recording on an electronic device.

In classical holography the physical reconstruction process is performed by illumination of the developed hologram with the reference wave. In digital holography this process is replaced by computer simulation. Before considering the different recording and reconstruction geometries, we will introduce some mathematical definitions that are helpful for the description of digital reconstruction. From the diffraction theory we know that if the amplitude and phase of a wavefront are known at a plane (x_1, y_1), it is possible to calculate the propagation of such a wavefront in the plane (x_2, y_2), see Fig. 9.1.52. The recorded intensity is multiplied with a numerical representation of the reference wave followed by numerical calculation of the resulting diffraction field at a certain distance d in z-direction from the hologram plane where the reconstruction is supposed to be located. For calculating the diffracted wavefront there are different approximations, which may be deduced by solving the wave equation. If we consider the Rayleigh–Sommerfeld diffraction integral

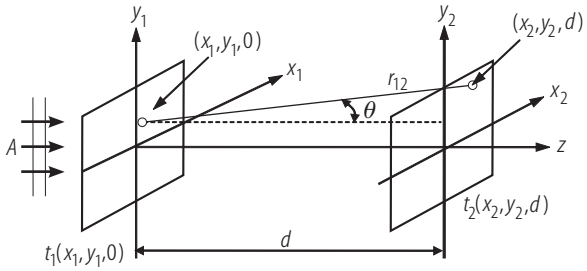

Fig. 9.1.52. Geometry for Rayleigh–Sommerfeld diffraction.

[96Goo], between two planes the wave field at a distance d is given by:

$$U_2(x_2, y_2, d) = \frac{\mathrm{i}\,A}{\lambda} \iint U_1(x_1, y_1) \frac{\exp(\mathrm{i}\,k r_{12})}{r_{12}} \cos(\theta)\ \mathrm{d}x_1\,\mathrm{d}y_1\ , \tag{9.1.62}$$

where $r_{12} = \sqrt{d^2 + (x_2 - x_1)^2 + (y_2 - y_1)^2}$ and $k = 2\,\pi/\lambda$; A is the amplitude of the incident wave and $\cos(\theta)$ is the obliquity factor. It should be mentioned that a slightly different assumption in the boundary conditions lead to different obliquity factors. If we consider e.g. the Kirchhoff–Fresnel approximation the obliquity factor is given by $(1 + \cos\theta)/2$ [96Goo]. For small θ there is only a small difference between the two. In the following the obliquity factor will be neglected.

If the distance d between the object and hologram plane or the hologram and the image plane is large compared to $(x_1 - x_2)$ and $(y_1 - y_2)$ the binominal expansion of the square root up to the third term yields:

$$r_{12} \approx d \left[1 + \frac{1}{2} \left(\frac{x_1 - x_2}{d} \right)^2 + \frac{1}{2} \left(\frac{y_1 - y_2}{d} \right)^2 \right] . \tag{9.1.63}$$

Equations (9.1.62) and (9.1.63) give the Fresnel approximation of the diffraction integral:

$$U_2(x_2, y_2, d) = \frac{A\,\mathrm{e}^{\mathrm{i}\,kd}}{\mathrm{i}\,\lambda\,d}\, \mathrm{e}^{\mathrm{i}\,\frac{k}{2d}\left(x_2^2 + y_2^2\right)} \iint U_1(x_1, y_1)\, \mathrm{e}^{\mathrm{i}\,\frac{k}{2d}\left(x_1^2 + y_1^2\right)}\, \mathrm{e}^{-\mathrm{i}\,\frac{k}{d}(x_1 x_2 + y_1 y_2)}\, \mathrm{d}x_1\,\mathrm{d}y_1\ . \tag{9.1.64}$$

Equation (9.1.64) has the form of a convolution integral, and we know from the Fourier theory that a convolution of two functions in the space domain is equivalent to multiplying their individual Fourier transforms. By inverse Fourier transforming we go back to the space domain. This property is very useful since it allows the computation of the wavefront propagation in a short time. If we consider a digitized wave field from which we would like to compute the propagation (e.g. formed by 1000×1000 points) it would take a very long time to compute the convolution integral described by (9.1.64), convolutions are in fact time-consuming. The Fourier transform of a discrete function can be calculated in a short time by using the FFT (Fast-Fourier-Transform) algorithm and this allows a dramatically reduced computation time of the discretized wave fields.

In order to simplify the notation we introduce a function approximating a spherical wavefront diverging from a point located at distance d from the origin of the coordinate system (Fresnel approximation)

$$h(x_1, y_1, d) = \exp\left[\frac{\mathrm{i}\,k}{2d} \left(x_1^2 + y_1^2 \right) \right] . \tag{9.1.65}$$

The Fresnel transform described by (9.1.64) can be seen as a Fourier transform of the object wave field multiplied by a quadratic factor and can be written in the more compact form

$$U_2 = \frac{A\,\mathrm{e}^{\mathrm{i}\,kd}}{\mathrm{i}\,\lambda\,d} U_1 \otimes h\ , \tag{9.1.66}$$

where $\otimes$ denotes convolution. The multiplicative phase term $\left(A\,\mathrm{e}^{\mathrm{i}\,kd}\right)/(\mathrm{i}\,\lambda\,d)$ will be omitted in the following calculations. To simplify the writing the coordinate dependence is omitted.

The wavefront in the hologram plane is related to the distribution in the object plane by the convolution of U_1 with the impulse response h. If we write U_O as the object wave instead of U_1 (see (9.1.57)), the intensity recorded by the sensor may be written in the form

$$I_\mathrm{H} = |U_\mathrm{R}|^2 + |U_\mathrm{O} \otimes h|^2 + U_\mathrm{R}\,[U_\mathrm{O} \otimes h]^* + U_\mathrm{R}^*\,[U_\mathrm{O} \otimes h]\ . \tag{9.1.67}$$

This expression will be used in the calculations describing the digital reconstruction of the wavefronts. After this mathematical review of the formulae of wave propagation we may now consider some recording geometries and the corresponding reconstruction method.

We will begin our description with the lensless Fourier hologram, which is relatively simple because the digital reconstruction requires only the calculation of the Fourier transform of the recorded discrete intensity.

9.1.8.3.2.1 Lensless Fourier hologram

The arrangement used to record a lensless Fourier (or quasi-Fourier) hologram (these are the two names used in the literature) is shown in Fig. 9.1.53. Instead of recording the holograms on films as discussed before, they are recorded on a low-resolution electronic device. For the hologram recording a point source located close to the object is used as a reference. The spherical reference U_{R} used for the hologram recording can be approximated by the function $h(x+a, y, d)$ (see (9.1.65)), where a denotes the offset of the reference point source, $P = (-a, 0)$. By taking the Fourier transform of I_{H} we will get the reconstruction of four wavefronts.

In this notation the last term of (9.1.67) leads to

$$I_{\mathrm{H}P}(x_{\mathrm{H}}, y_{\mathrm{H}}) = h\,(x_{\mathrm{H}} + a, y_{\mathrm{H}}, -d)\,[U_{\mathrm{O}}(x_{\mathrm{H}}, y_{\mathrm{H}}) \otimes h(x_{\mathrm{H}}, y_{\mathrm{H}}, d)]\ . \tag{9.1.68}$$

The Fourier transform of the quadratic function $h(x_{\mathrm{H}}, y_{\mathrm{H}}, d)$ is still a quadratic function. After some manipulation, in particular by using the convolution theorem, the Fourier transform $\mathcal{F}$ of $I_{\mathrm{H}P}(x_{\mathrm{H}}, y_{\mathrm{H}})$ takes the form [74Cat]

$$\mathcal{F}\,\{I_{\mathrm{H}P}(x_{\mathrm{H}}, y_{\mathrm{H}})\} = \lambda^2 d^2\, \exp\left\{\mathrm{i}\,k\,a_{\mathrm{f}}^2\right\}\, U_{\mathrm{O}}(-x_{\mathrm{f}} - a_{\mathrm{f}}, -y_{\mathrm{f}})\, h\,(x_{\mathrm{f}}, y_{\mathrm{f}}, d)\ , \tag{9.1.69}$$

which represents an inverted image U_{O} of the object multiplied by a quadratic phase factor and shifted by a_{f}. x_{f} and y_{f} denote the coordinates in the Fourier plane. Without loss of generality, we assume that the wavefront is reconstructed with unity magnification, i.e. $a_{\mathrm{f}} = a$. (Since the wavefront is not reconstructed physically we can change its size). By analogy, the Fourier transform of the third term of the intensity function will lead to the secondary reconstruction. Both the primary and secondary images are focused. The Fourier transform of a real positive function (the intensity) yields a Hermitian distribution in the Fourier plane, with its absolute value symmetrical with respect to the center.

Figure 9.1.54 shows a one-dimensional sketch of the hologram spectrum. The spectrum of the first term in (9.1.67) is, for a homogeneous wave, a delta function centered at the origin and does not disturb the reconstruction because its spatial extension is very small. A more fundamental limit is the spread of the central distribution due to the Fourier transform of $|U_{\mathrm{O}} \otimes h|^2$ which will

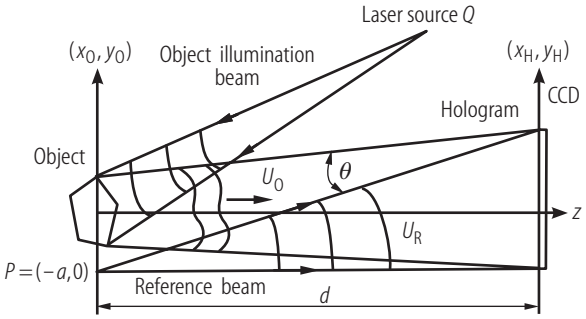

Fig. 9.1.53. Recording of an off-axis digital hologram.

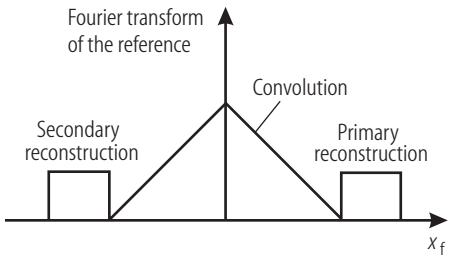

Fig. 9.1.54. Spectrum of a hologram, the components are well separated.

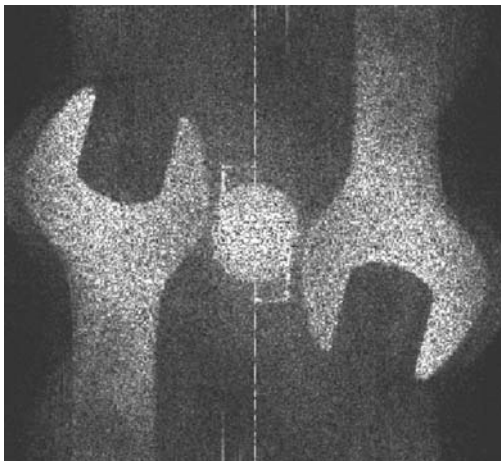

Fig. 9.1.55. Digital reconstruction of a quasi-Fourier hologram.

represent a distribution having twice the extension of the reconstructed object. In order to avoid their superposition in the reconstructed images, the closest object point must be at least one object width from the reference. In practice this condition reduces the reconstructed object size almost by a factor of four.

Figure 9.1.55 shows an example of a reconstructed quasi-Fourier hologram of a small object (3×5 cm^2). The object was located at the distance $d = 140$ cm from the sensor. The hologram was recorded on a 512×512 array and the Fourier transform calculated with an FFT algorithm implemented on a computer (PC). The bright area in the center is the superposition of the reference wave and a convolution term.

9.1.8.3.2.2 Fresnel hologram

A Fresnel hologram may be recorded by using the arrangement shown in Fig. 9.1.53 but we would like to point out that the reference does not need to be a point source located in the plane of the object. Simulating the diffraction of the reference wave used for the recording the digital reconstruction of the complex amplitude in a plane at a distance d from the hologram can be calculated. In digital holography we usually use a homogeneous plane or spherical wave for the recording which can be simulated easily. The wavefronts diffracted by the hologram are obtained by multiplying the intensity I_H recorded with the reference wave U_R and calculating the resulting diffraction. Mathematically we can write the wavefront in the plane (x, y) located at the distance d from the hologram in the form

$$U_\mathrm{r} = [U_\mathrm{R} I_\mathrm{H}] \otimes h \; . \tag{9.1.70}$$

As noted before, this calculation can be carried out using a Fourier-Transform (FT) algorithm. We obtain a reconstruction of the object wavefront without any additional quadratic phase term as for the quasi-Fourier hologram. It should be noted that the Fresnel approximation is valid only when the distance d is large with respect to the size of the recorded hologram. A digital reconstruction of the wavefront close to the hologram needs special considerations.

Recording a digital Fresnel hologram of a large object requires frequently a demagnification by means of an optical system. In this way the angle between the object and the reference beam is reduced. A positive lens [95Ped] or a negative lens [96Sch, 99Wag] can be helpful.

9.1.8.3.2.3 Image-plane hologram

For an image-plane digital hologram the object is projected onto the detector array by a lens system, as shown in Fig. 9.1.56. The arrangement is very similar to that one used for speckle pattern interferometry. Image-plane holography is very suitable to calculate the complex amplitude of a wavefront in the plane of the detector. In order to reduce the spatial frequency of the wavefront arriving on the sensor (increase the speckle size), an aperture (AP) has been inserted. The reference is a spherical wave originating from the point P located close to the aperture. A quasi-Fourier hologram of the aperture (with size and distance from the reference chosen in order to satisfy the sampling theorem) is recorded. By performing a Fourier transform of the intensity recorded with such an arrangement, we get two reconstructions (primary and secondary) of the reconstruction of the aperture together with the central convolution term. When the three terms are well separated (as in the case of Fig. 9.1.57), we can filter out the central term and one of the reconstructions of the aperture and keep the other. After this filtering operation an inverse Fourier transform is applied and the complex amplitude of the object wave field in the hologram plane, which is the image plane, is obtained.

It appears clearly from Fig. 9.1.57 that the most convenient form of the aperture is the rectangular one. This is the best compromise between the possibility of filtering and the possibility of using the maximum of the area. It is obvious that the aperture should be chosen as large as possible for two reasons: firstly for improved light collection, and secondly for collecting higher spatial frequencies leading to increased spatial resolution.

Unlike the quasi-Fourier and Fresnel holograms, the reconstructed image-plane hologram is localized in the image plane. This means that a certain area of the image-plane hologram contains only information about a certain part of the object.

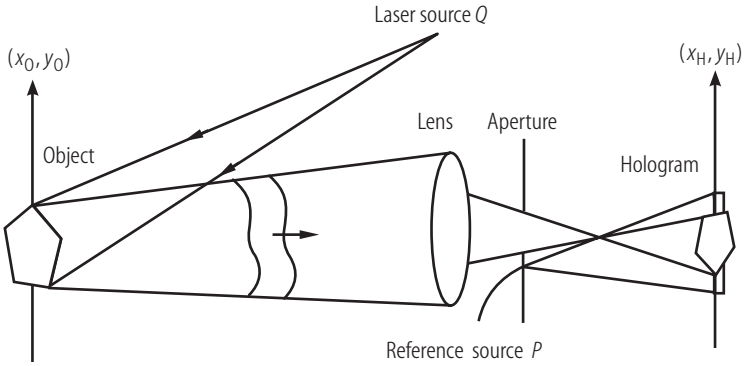

Fig. 9.1.56. Arrangement for the recording of an image-plane hologram.

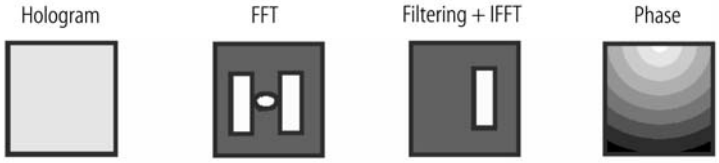

Fig. 9.1.57. Filtering procedure for obtaining the phase.

9.1.8.4 Digital holographic interferometry

9.1.8.4.1 Principle of digital holographic interferometry

The advantage of digital holography is the calculation of the phase of the reconstructed wavefront from the complex amplitude. The digital method allows not only the analysis of wavefronts without physical reconstruction but also a comparison of two or more wavefronts [76Fri, 85Tha, 94Sch, 95Ped, 96Goo, 96Ped, 96Sch, 97Ada, 97Ped1, 97Ped2, 97Ped3, 97Ped4, 98Ped, 98Seb, 99Ped1, 99Ped2, 99Ped3, 01Ped, 01Per, 01Sch, 01See, 02Kol].

Therefore, two digital holograms can be recorded for example without and with loading as in classical holographic interferometry and in speckle pattern interferometry. However, no physical reconstruction of the two stored holograms is required in digital holographic interferometry. We denote the two corresponding reconstructed wave fields without and with loading by U_O and $\overline{U}_\mathrm{O}$, respectively, as in Sect. 9.1.8.2. The wrapped phases ϕ_w and $\overline{\phi}_\mathrm{w}$ of the reconstructed wavefronts can be obtained from the complex amplitudes by

$$\phi_\mathrm{w} = \arg\left(U_\mathrm{O}\right) \ , \tag{9.1.71}$$

$$\overline{\phi}_\mathrm{w} = \arg\left(\overline{U}_\mathrm{O}\right) \ , \tag{9.1.72}$$

where arg denotes the argument of a complex amplitude. The dependence from the position (x, y, z) has been omitted for convenience. The phases ϕ_w and $\overline{\phi}_\mathrm{w}$ vary between 0 and $2\,\pi$. The difference between the wavefronts is obtained by the phase differences

$$\Delta\phi_\mathrm{w} = \overline{\phi}_\mathrm{w} - \phi_\mathrm{w} \ . \tag{9.1.73}$$

In order to have a phase difference in the interval from 0 to $2\,\pi$ it is necessary to add $2\,\pi$ if $\Delta\phi_\mathrm{w} < 0$. $\Delta\phi_\mathrm{w}$ is a wrapped phase map ($0 \leq \Delta\phi_\mathrm{w} \leq 2\,\pi$) containing the information about the change of the wavefront between the two exposures.

When an object illuminated by coherent light is deformed, the phases of the reflected wavefront change as a function of the deformation [79Sch, 79Ves, 96Kre]. If we consider two states of the object (before and after deformation), the relation between the deformation vector $\boldsymbol{L}$ and the change of the optical phase $\Delta\phi$ of the wavefront is given by

$$\Delta\phi = \frac{2\,\pi}{\lambda}\,\boldsymbol{L}\cdot\boldsymbol{s} \ , \tag{9.1.74}$$

where $\boldsymbol{s}$ is the sensitivity vector given by the geometry of the set-up: $\boldsymbol{s} = \boldsymbol{k}_\mathrm{i} - \boldsymbol{h}$, where $\boldsymbol{k}_\mathrm{i}$ and $\boldsymbol{h}$ are the unit vectors of illumination and observation, respectively. Digital holography permits the calculation of the phase difference modulo $2\,\pi$ of the phase difference $\Delta\phi_\mathrm{w}$ between two wavefronts; the phase $\Delta\phi$ is obtained by unwrapping $\Delta\phi_\mathrm{w}$. From (9.1.74) the projection of the deformation $\boldsymbol{L}$ on the sensitivity vector $\boldsymbol{s}$ is calculated from the phase $\Delta\phi$.

A few results of some applications of digital holographic interferometry will be presented. In particular the phase difference obtained by subtraction from different digital holograms recorded at different times will be shown leading to the measurement of deformation, vibration, or shape.

9.1.8.4.2 Digital holographic interferometry for dynamic deformations

9.1.8.4.2.1 Dimensional measurements

Figure 9.1.58 shows an interference pattern obtained by recording two digital image-plane holograms of a plane object (metal plate) submitted to a shock. A pulsed ruby laser with pulse width of 20 ns, which can emit two high-energy pulses separated by few microseconds has been used for the recording of the two holograms on a CCD. The laser pulses were fired shortly after the shock

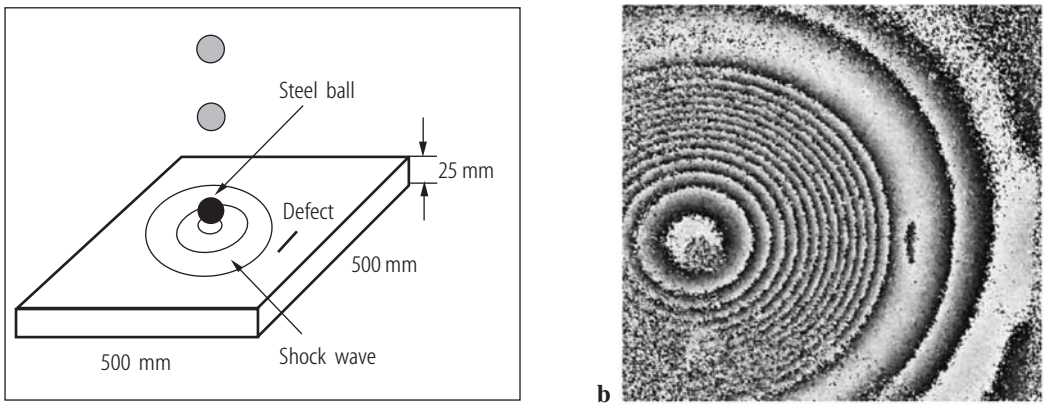

Fig. 9.1.58. (**a**) Object submitted to a shock excitation. (**b**) Phase map obtained by double-pulse-exposed digital holography.

produced by a metal ball falling on the plate. After calculation and subtraction of the phases of the two reconstructed digital holograms, we get a phase map containing 2π discontinuities. Notice that the fringes are concentric around the point of the impact. A small defect was inserted in the plate and the shock wave propagating at the surface of the plate is disturbed by this defect. This example shows the principle for defect detection in mechanical parts with digital holographic interferometry [01Sch].

For this kind of investigations the holograms recorded by the CCD for each laser pulse must be separated. Two or even four separated holograms can be recorded on a CCD sensor with pulse separation in the microsecond range. For the recording of two digital holograms within few microseconds the procedure is the following. The first pulse is fired producing the electrical charges inside the photosensors corresponding to the recording of the first hologram. Since we record 2 separated holograms (and not a sum of 2 holograms) it is necessary to transfer the information of the first hologram before the second pulse is fired. In a commercially available CCD it is possible to transfer the image (or more correctly the electrical charges corresponding to the recorded image) from the photosensors to the shift register. The time necessary for the transfer is short (2 . . . 5 microseconds for a commercially available interline sensor) because the transfer is parallel from each photosensor to the adjacent register cell. After the charge transfer, the photosensors of the camera are ready for the new image that is recorded with the second pulse. The charges corresponding to the 2 holograms are transferred from the CCD into a computer and digitally evaluated later.

9.1.8.4.2.2 Digital holographic interferometry for deformation and vibration analysis of 3D objects

In some cases a three-dimensional analysis of the deformation or vibration is necessary. This can be obtained if the shape of the object under investigation and the deformation are known. For 3D vibration analysis, the complete determination of the vibration occurs by combination of three different measurements, namely:

1. 3D vibration of the surface obtained by digital holography,
2. shape measurement of the object,
3. 3D vibration on a point obtained using a laser Doppler vibrometer for calibration.

The system used for the measurement of the vibrations is schematically shown in Fig. 9.1.59. Light from a pulsed ruby laser is divided into two beams, one is coupled into an optical monomode

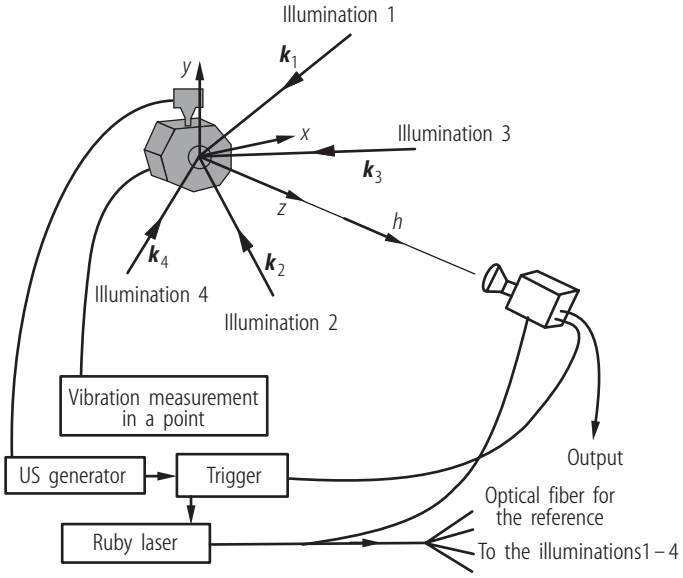

Fig. 9.1.59. Schematic arrangement for 3D deformation or vibration analysis of 3D objects.

fiber and serves as the reference beam and the other one is further divided into four beams used to illuminate the object from four different directions. Together with the reference beam, four different sensitivity vectors are formed.

Equation (9.1.74) gives us the deformation along one sensitivity vector. For the 3D case, the relation between the phase differences and the deformation $\boldsymbol{L}$ is

$$\Delta\phi_i = \frac{2\pi}{\lambda}\,\boldsymbol{L}\cdot\boldsymbol{s}_i\ . \tag{9.1.75}$$

The sensitivities $\boldsymbol{s}_i$ are given by the geometry of the set-up:

$$\boldsymbol{s}_i = \boldsymbol{k}_\mathrm{i} - \boldsymbol{h}\ , \quad i = 1, 2, 3, \ldots\ , \tag{9.1.76}$$

where $\boldsymbol{k}_\mathrm{i}$ and $\boldsymbol{h}$ are the unit vectors of illumination and observation, respectively. The most convenient way to determine the deformation vector $\boldsymbol{L}$ is to decompose all vectors into their orthogonal components x, y, and z.

There are many known methods used for shape measurement, for instance: triangulation [97Hun], fringe projection, interferometric methods (holography, speckle interferometry). We will restrict our attention to interferometric methods based on digital holography [98Seb, 99Ped1, 99Ped2, 02Kol].

The two-wavelength method for contouring was used in the early years of holography [76Fri, 85Tha]. Two holograms of an object were recorded with two wavelengths (λ_1 and λ_2) on holographic film; for the reconstruction the hologram was illuminated by a laser using one wavelength. Contour fringes corresponding to the object shape were obtained on the reconstructed object. Digital holography can be used for shape measurement in an optical set-up where two digital holograms are recorded using two different wavelengths. There are different methods to change the wavelength of a laser e.g. a dye laser or a diode laser with external cavity discussed in Sect. 9.1.7.5.2 when only a small change of the wavelength is necessary. For very small wavelength change, tuning a laser diode by changing the temperature or the injection current may be used. When the form of the object has to be determined in a short time, e.g. few microseconds, a pulsed laser has to be used. The wavelength of a pulsed ruby laser may be changed by changing the spacing between the etalon plates of the laser cavity [99Ped1].

Two separated holograms are recorded at two different wavelengths λ_1 and λ_2, and the phases $\phi_{\lambda 1}$ and $\phi_{\lambda 2}$ are calculated digitally. The phase difference contains the information about the shape

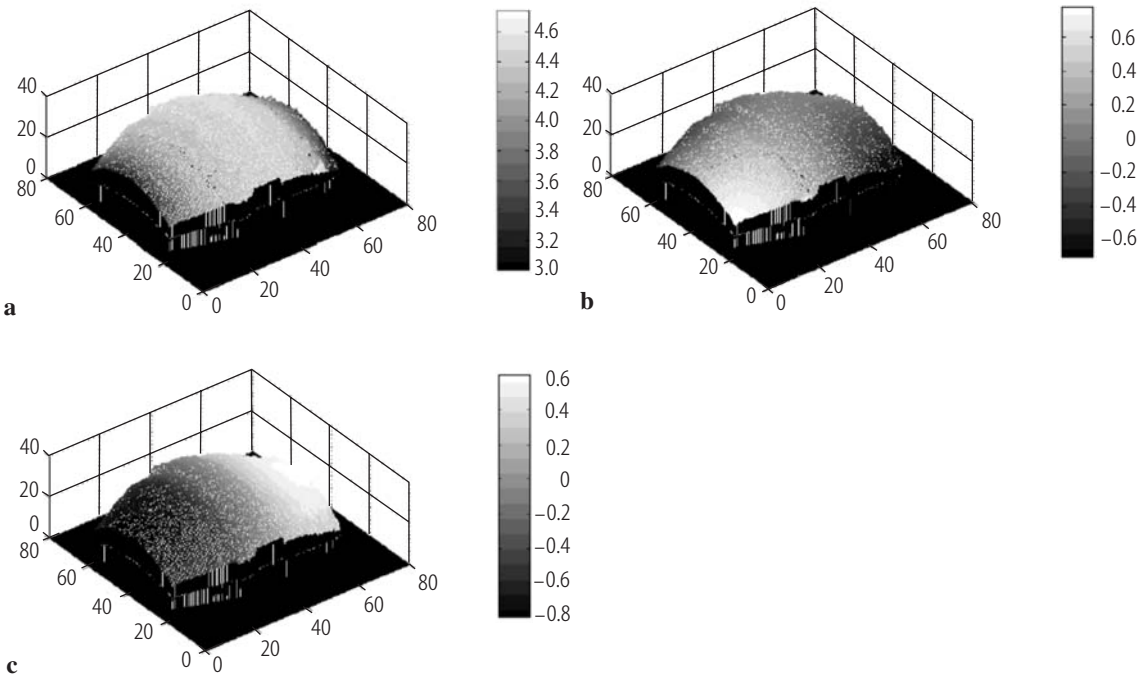

Fig. 9.1.60. Superposition of the 3D vibration amplitudes on the shape of the object. Amplitudes along the (**a**) x-direction, (**b**) y-direction, and (**c**) z-direction, respectively. The shape of the object is given in mm, the gray scale for the vibration amplitude is in μm. It should be noticed that the gray scale is different for each picture.

of the object. In the case where the illumination is parallel to the observation, the fringes of equal phase obtained represent the intersection of the object surface with equidistant planes of spacing

$$\Lambda = \frac{\lambda_1 \lambda_2}{2\,|\lambda_1 - \lambda_2|}\ . \tag{9.1.77}$$

If for the illumination a diverging beam is used and the observation is not parallel to the illumination direction, a factor depending on the geometry of the arrangement needs to be introduced in (9.1.77).

An example of the 3D information obtained for a vibrating object is shown in Fig. 9.1.60. The object was a tool used in the ultrasound technology vibrating at a frequency of 20 kHz. The deformations in the three directions (x, y, z) are superimposed onto the shape measurements. The magnitude of the amplitude is coded by gray levels. The maximum of the vibrating amplitude is in the x-direction. This is as expected because the object was excited by a piezoelectric actuator along this direction. The shape of the object was measured by the two-wavelength method implemented by changing of the etalon plate separation. A precise 3D measurement of the vibrations in a point occurred by using a three-beam Doppler laser vibrometer. This measurement is necessary because in double-pulse holography we get only the relative deformation of the object in the time between the two pulses. Even in the case of a simple harmonic vibration, the information of the deformation between the two laser pulses is not sufficient to reconstruct the amplitude and phase of the vibration, as the absolute deformation is unknown. The total object deformation is obtained from the vector resultant from the data obtained from the phase maps for each sensitivity vector with the combination of the object shape obtained from the contouring measurements.

9.1.8.4.3 Pulsed digital holographic interferometry for endoscopic investigations

Holographic interferometry combined with endoscopy enhances the versatility of standard 2D endoscope imaging as it opens up possibilities to measure additional parameters, on hidden surfaces [01See, 02Kol, 03Kol, 03Ped2]. Combinations of the digital holography with an endoscope for carrying the image and a pulsed laser as light source allow measurements in an industrial environment (e.g. vibration measurements, non-destructive testing of technical objects) and in-vivo investigation of biological tissues [99Ped1, 99Sch, 00Kem, 01Sch, 01See, 02Kol].

Figure 9.1.61 shows a schematic illustration of rigid and flexible endoscopes combined with a measuring system based on pulsed holographic interferometry. The optical set-up consists of the pulsed laser, the interferometer unit with the CCD camera, and the endoscope unit. Figure 9.1.61a shows the arrangement for a rigid endoscope. However, the set-up can also be combined with a flexible fiber endoscope, as shown in Fig. 9.1.61b. Rigid and flexible endoscopes have a lot in common. The objective lens forms an image of the subject which in turn is transferred by the relay optics and magnified by a lens system on the sensor. To allow flexibility the image is carried by a bundle of optical fibers, instead of a system of lenses as for the rigid endoscopes. The resolution of a flexible endoscope depends on the number of fibers and their diameter. More fibers of smaller diameter give higher spatial resolution.

For both arrangements the recording procedure and the way to process the digital holograms is exactly the same. The pulsed laser emits short (20 ns) Q-switched pulses, which are divided at the beam-splitter in the reference and the object beam. The reference beam is conveyed to the interferometer unit with a single-mode optical fiber. An image-plane hologram is formed on the CCD detector as a result of the interference between the slightly off-axis reference beam and the object beam. The diverging output beam illuminates the object, the light is diffusely reflected back from the object surface towards the endoscope, which in turn brings the object information to the interferometer unit. The aperture serves to limit the spatial frequencies of the interference pattern in such a way that the detector resolves it. The dimensions of the aperture are chosen considering the resolution of the CCD detector and the distance between the aperture and the sensor. Two or more digital holograms, corresponding to the laser pulses, are captured at separate video frames of the CCD camera.

Figure 9.1.62 shows an example where the system was used to measure inside a pump; Fig. 9.1.62b shows an image of the inside of the pump, and Fig. 9.1.62c shows an interferogram. During the pumping operation, the piston is moving forward and backward (frequency 50 Hz). At the right side (piston) there are more fringes. This means that the piston movement was increased as compared to the other areas around. This example shows that by using the endoscopic technique it is possible to look inside a more or less closed object and investigate deformation and vibrating portions.

A dynamical deformation of in-vivo biological tissues was tested. The problem with measurements of biological tissues is that the reflectivity is not ideal and furthermore any disruption of

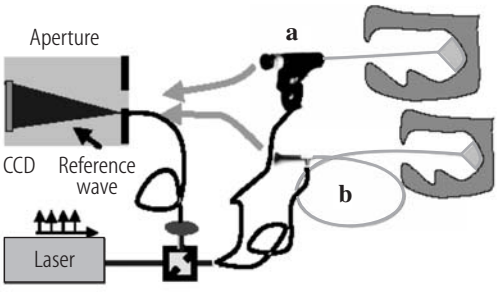

Fig. 9.1.61. Set-up with (**a**) rigid and (**b**) flexible fiber endoscopes for investigations together with pulsed digital holography.

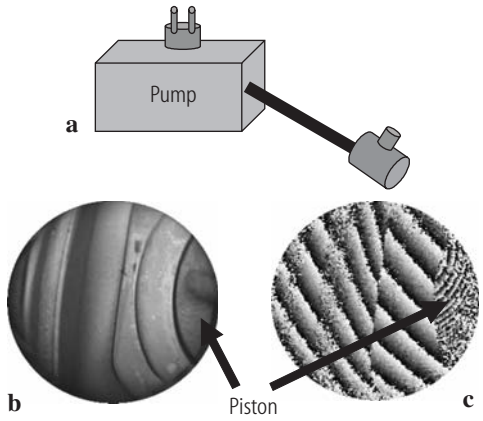

Fig. 9.1.62. (**a**) Measurements inside a pump. (**b**) Image of the object. (**c**) Phase map obtained during the pump operation.

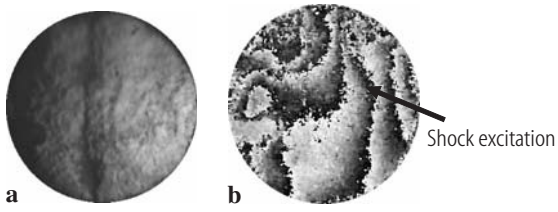

Fig. 9.1.63. In-vivo investigation inside the oral cavity. (**a**) Image of the investigated part (tongue). (**b**) Phase map corresponding to the deformation produced by a shock excitation of the tongue.

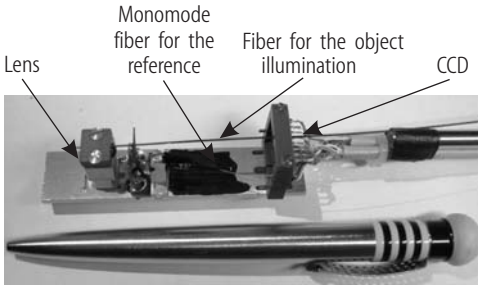

Fig. 9.1.64. Image of the prototype, diameter: 18 mm.

the biological tissue produces, together with the deformation, alterations of the microstructure of the surface. Consequently, the correlation between the holographic patterns recorded with the two laser pulses is reduced resulting in noise in the fringe patterns leading to poor quality. Figure 9.1.63 shows phase maps obtained from measurements performed inside the oral cavity (in vivo) using a rigid endoscope.

In order to measure at hidden surfaces, we can combine commercially available endoscopes with an interferometer based on digital holography. Recently, with the newer smaller CCD detector arrays, it has become possible to build the complete interferometric system small (CCD included). Figure 9.1.64 shows a picture of a built prototype. The chip has 659×494 pixels (pixel size 7.4×7.4 μm^2). The sensitive area is quite small (4.8×3.6 mm^2), but the sensor is inserted on a mount which has much larger size (12×13 mm^2), in effect limiting the size of our holographic head to a diameter of 18 mm. The prototype shown in Fig. 9.1.64 has been used to perform measurements inside a cavity, as shown in Fig. 9.1.65. A pulsed Nd:YAG laser was used for these measurements. Meanwhile the size of the interferometer has been reduced to a diameter of 6 mm.

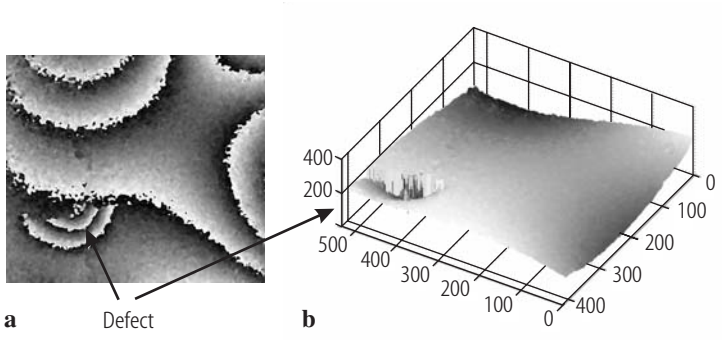

Fig. 9.1.65. Vibration measurement of an object with a defect located inside a cavity. Vibration frequency: 2350 Hz. (**a**) Phase map. (**b**) Pseudo 3D representation of the vibration.

9.1.8.4.4 Temporal phase unwrapping of digital holograms

In Sect. 9.1.7.5 a technique to analyze dynamical deformation based on temporal speckle pattern interferometry is described. The method will be extended to digital holography. The complex amplitude of an object submitted to dynamical deformation is a function of the time. On the sensor plane this amplitude is

$$U_{\mathrm{H}}(x,y,t) = |U_{\mathrm{H}}(x,y,t)| \, \exp\{\mathrm{i}\,\phi_{\mathrm{H}}(x,y,t)\} \ , \tag{9.1.78}$$

where $|U_{\mathrm{H}}(x,y,t)|$ and $\phi_{\mathrm{H}}(x,y,t)$ are the amplitude and the phase of the wavefront as a function of the position and the time, respectively. We consider now the case where a sequence of K digital holograms (e.g. 100 or 1000) of an object submitted to deformation is recorded. For each hologram (frame), the intensity is integrated during the exposure period $\Delta\tau$. The intensity recorded in one camera frame can be written as

$$I_{\mathrm{H}}(m\Delta x, n\Delta y, k\Delta\tau) = \int\limits_{(k-1)\Delta\tau}^{k\Delta\tau} I_{\mathrm{H}}(m\Delta x, n\Delta y, t)\,\mathrm{d}t \ , \tag{9.1.79}$$

where k is an integer number indicating the recorded frame, k takes the value 1 for the first frame of the sequence and K for the last. The operation described by (9.1.79) corresponds to a time averaging of the hologram during the period $\Delta\tau$. If the deformation of the object is small during the frame exposure, the phase ϕ_{H} recorded may be considered as a constant across the pixel and can be reconstructed from the intensity $I_{\mathrm{H}}(m\Delta x, n\Delta y, k\Delta\tau)$. The time necessary to record the sequence will be $K\Delta\tau$. Each hologram is then processed individually as shown in Fig. 9.1.66. This operation is nothing else than the calculation of the phase for each recorded hologram by using the method described in Fig. 9.1.57. From the hologram intensity $I_{\mathrm{H}}(m\Delta x, n\Delta y, k\Delta\tau)$ we will get the phase $\phi_{\mathrm{H}}(m\Delta x, n\Delta y, k\Delta\tau)$ at the point $(m\Delta x, n\Delta y)$ and at the time $k\Delta\tau$. The phase

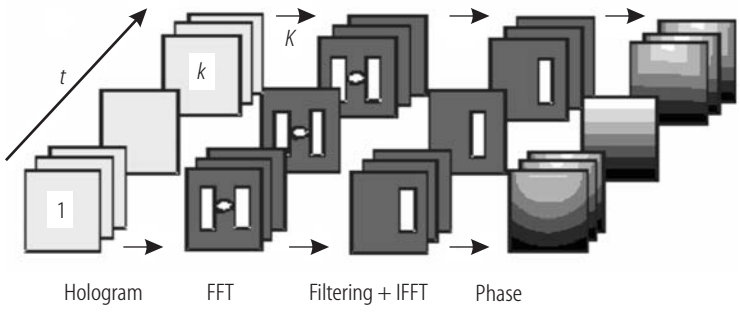

Fig. 9.1.66. Procedure for calculating the phase from a sequence of digital holograms.

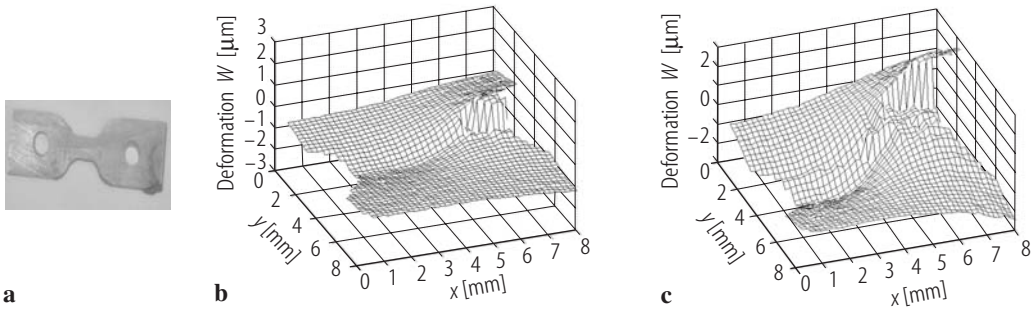

a b c

Fig. 9.1.67. Deformation measurement of (**a**) a notched piece of a bone immersed in water. Measurement at two different times, namely (**b**) 0.5 s and (**c**) 1.5 s after the beginning of the loading process.

$\phi_{\mathrm{H}}(m\Delta x, n\Delta y, k\Delta\tau)$ obtained from the evaluation of the digital holograms is in the interval $-\pi$ to π and is indefinite to an additive integer multiplied by $2\,\pi$. The unwrapping procedure involves the detection of the phase steps. The unknown integer multiplied by $2\,\pi$ is detected by comparison of two successive phase changes. If the change is larger than π, the value of the integer multiple is increased by 1, if the change is lower than $-\pi$, the value is decreased by 1. Consider now only one pixel, the phase at this pixel as a function of the time may easily be unwrapped by a one-dimensional unwrapping algorithm. The temporal unwrapping can be done for all the points of the sensor and a two-dimensional evaluation of the phase as a function of the time can be obtained. Some pixels (due to the low modulation of the interference fringes) do not give a good measurement of the phase. In order to detect the pixels not giving good results, the intensity modulation as a function of the time for each pixel is calculated. The method measures the phase change for each pixel, by assigning the value 0 to the initial phase change and calculate all the deformations with respect to this initial phase.

Combining digital holography and the temporal phase unwrapping leads to the investigation of dynamical deformations [03Ped1]. This method can be applied successfully when the recorded sequence of digital holograms satisfies the sampling theorem in the spatial and temporal domain. For the spatial domain we need the period of the cycle produced by interference between the reference and the object beams to be larger than two times the sensor pixel, this allows to get the phase from the digital hologram. In the time domain we need to sample the hologram in order that from one hologram of the sequence to the next one the change of the phase is smaller than π.

Compared with the temporal speckle method described in Sect. 9.1.7.5 this method has the advantages that it calculates the phase and thus gives us the information about the direction of the deformation without the introduction of additional temporal phase modulation (heterodyne technique) [01Tiz].

The method has been used to measure the deformation of biological tissues. Figure 9.1.67 shows a measurement where the object, a piece of deer antler immersed in water, was loaded by using a special tension device. The camera used had 690×480 pixels with an acquisition rate of 30 full frames/second. The measurements were performed within a period of 4 seconds (during this period the sample was loaded), and 120 holograms (30 each second) were recorded. Figure 9.1.67 shows the results of the object deformation at two different times after the beginning of the loading process. Close to the notch we see a strange deformation. This is the location where the bone will break.

References for 9.1

1819Ara Arago, F., Fresnel, A.: Ann. Chim. Phys. **2** (1819) 288.

1852Sto Stokes, G.G.: Trans. Cambridge Phil. Soc. **9** (1852) 399–416.

21Mic Michelson, A.A., Pease, F.G.: J. Astrophys. **53** (1921) 249.

34Van Van Cittert, P.H.: Physica **1** (1934) 201–210.

38Zer Zernike, F.: Physica **5** (1938) 785–795.

39Van Van Cittert, P.H.: Physica **6** (1939) 1129–1138.

48Gab Gabor, D.: Nature (London) **161** (1948) 777.

51Hop Hopkins, H.H.: Proc. R. Soc. (London) A **208** (1951) 263–277.

53Hop Hopkins, H.H.: Proc. R. Soc. (London) A **217** (1953) 408–432.

54Wol Wolf, E.: Proc. R. Soc. (London) A **225** (1954) 96–111.

55Hop Hopkins, H.H.: Opt. Acta **2** (1955) 23–29.
55Wol Wolf, E.: Proc. R. Soc. (London) A **230** (1955) 246–265.

62Shu Shurcliff, W.A.: Polarized light, Cambridge: Harvard University Press, 1962.

64Lei Leith, E.N., Upatnieks, J.: J. Opt. Soc. Am. **54** (1964) 1295.
64Mur Murty, M.V.R.: Appl. Opt. **3** (1964) 853.

65Gol Goldfischer, L.I.: J. Opt. Soc. Am. **55** (1965) 247.
65Man Mandel, L., Wolf, E.: Rev. Mod. Phys. **37** (1965) 231–287.

66Fra Francon, M.: Optical interferometry, New York: Academic Press, 1966.

70Arc Archbold, E., Burch, J.M., Ennos, A.E.: Opt. Acta **17** (1970) 883–898.
70Hop Hopkins, H.H., Tiziani, H.J.: Proc. Int. Symposium on Holography, Besancon, 1970.

71But Butters, J.N., Leendertz, J.A.: J. Phys. E **4** (1971) 277–279.
71Col Collier, R.J., Burckhard, C.B., Lin, L.H.: Optical holography, Chap. 5, New York: Academic Press, 1971.
71Dur Durst, F., Withelaw, J.H.: J. Phys. E **4** (1971) 804.

72Tiz1 Tiziani, H.J.: Appl. Opt. **11** (1972) 2911–2917.
72Tiz2 Tiziani, H.J.: Opt. Commun. **5** (1972) 271–274.
72Wya Wyant, J.C., Bennett, V.P.: Appl. Opt. **11** (1972) 2833–2839.

74Bru Bruning, J.H., Herriott, D.R., Gallagher, J.E., Rosenfeld, D.P., White, A.D., Brangaccio, D.J.: Appl. Opt. **13** (1974) 2693–2703.
74Cat Cathey, W.T.: Optical information processing and holography, Chap. 9, New York: John Wiley & Sons, 1974.
74Hun Hung, Y.Y.: Opt. Commun. **11** (1974) 132–135.

75Goo Goodman, J.W.: Statistical properties of laser speckle patterns, Chap. 2, in: Dainty, J.C. (ed.): Laser speckle and related phenomena, Berlin: Springer-Verlag, 1975, p. 9–75.
75Ste Stetson, K.A.: Opt. Eng. **14** (1975) 482–489.

76Fri Friesem, A.A., Levy, U.: Appl. Opt. **15** (1976) 3009–3020.

78But Butters, J.N., Jones, R.C., Wykes, C.: Electronic speckle pattern interferometry, in: Erf, R.K. (ed.): Speckle metrology, New York: Academic Press, 1978, p. 111–157.
78Enn Ennos, A.E.: Prog. Opt. **16** (1978) 233–288.
78Erf Erf, R.K.: Speckle metrology, New York: Academic Press, 1978.
78Gre Gregory, D.A.: Topological speckle and structural inspection, in: Erf, R.K. (ed.): Speckle metrology, New York: Academic Press, 1978, p. 183–223.

79Fra Francon, M.: Laser speckle and application to optics, New York: Academic Press, 1979.
79Sch Schumann, W., Dubas, M.: Holographic interferometry, Heidelberg: Springer-Verlag, 1979.
79Ves Vest, C.M.: Holographic interferometry, New York: John Wiley & Sons, 1979.

80Tiz Tiziani, H.J., Leonhardt, K., Klenk, J.: Opt. Commun. **34** (1980) 327–331.

82Doe Dörband, B.: Optik (Stuttgart) **60** (1982) 161.
82Tak Takeda, M., Hideki, I., Kobayashi, S.: J. Opt. Soc. Am. A **72** (1982) 156–160.

83Sch Schwider, J., Burow, R., Elssner, K.E., Grzanna, J., Spolaczyk, R., Merkel, K.: Appl. Opt. **22** (1983) 3421–3432.

84Dai Dainty, J.C.: Introduction, in: Dainty, J.C. (ed.): Laser speckle and related phenomena, 2nd edition, Berlin: Springer-Verlag, 1984.
84Lok Lokberg, O.J.: J. Acoust. Soc. Am. **75** (1984) 1783–91.
84McK Mc Kechnie, T.S.: Speckle reduction, in: Dainty, J.C. (ed.): Laser speckle and related phenomena, 2nd edition, Berlin: Springer-Verlag, 1984.
84Per Perry, G.: Speckle patterns in partially coherent light, in: Dainty, J.C. (ed.): Laser speckle and related phenomena, 2nd edition, Berlin: Springer-Verlag, 1984.

85Cre Creath, K.: Appl. Opt. **24** (1985) 3053–3058.
85Doe Dörband, B., Tiziani, H.J.: Appl. Opt. **24** (1985) 2604–2611.
85Tha Thalmann, R., Dändliker, R.: Opt. Eng. **24** (1985) 930–935.

86Joe Joenathan, C., Narayanmurthy, C.S., Sirohi, R.S.: Opt. Commun. **56** (1986) 309–312.
86Sch Schwider, J., Burow, R., Elssner, K.E., Grzanna, J., Spolaczyk, R.: Appl. Opt. **25** (1986) 1117–1121.

87Bor Born, M., Wolf, E.: Principles of optics, 6th edition, Oxford: Pergamon Press, 1987.
87Tyr Tyrer, T.R.: Proc. SPIE (Int. Soc. Opt. Eng.) **746** (1987) 98–103.

88Dae Dändliker, R., Thalman, R., Prongue, D.: Opt. Lett. **13** (1988) 339.
88Ste Stetson, K.A., Brohinsky, W.R.: J. Opt. Soc. Am. A **5** (1988) 1472–1476.

89Jon Jones, R., Wykes, C.: Holographic and speckle interferometry, 2nd edition, Cambridge: Cambridge Univ. Press, 1989.

90Har Hariharan, P.: Selected papers on interferometry, Bellingham, Washington: SPIE Press, 1990.

90Joe Joenathan, C., Tiziani, H.J., Pfister, P.: Appl. Opt. **29** (1990) 1905–1911.
90Ker Kerr, D., Santoyo, F.M., Tyrer, J.R.: J. Opt. Soc. Am. **7** (1990) 820–826.
90Kin Kino, G.S., Chim, S.S.C.: Appl. Opt. **29** (1990) 3775.

91Cre Creath, K.: Proc. SPIE (Int. Soc. Opt. Eng.) **1553** (1991) 213.
91Sir Sirohi, R.S.: Selected papers on speckle metrology, Washington: SPIE Press, 1991.
91Sod Sodnik, S., Fischer, E., Ittner, T., Tiziani, H.J.: Appl. Opt. **30** (1991) 3139.

92Bro Brosseau, C.: Fundamentals of polarized light: a statistical approach, New York: John Wiley & Sons, Inc., 1992.
92Dre Dresel, T., Häusler, G., Venzke, H.: Appl. Opt. **31** (1992) 919.
92Gre Greivenkamp, J.E., Bruning, J.H.: Phase shifting interferometry, in: Malacara, D. (ed.): Optical shop testing, 2nd edition, New York: John Wiley & Sons, Inc.,1992.
92Mal Malacara, D.: Optical shop testing, New York: John Wiley & Sons, Inc., 1992.
92Rod Rodriguez-Vera, R., Kerr, D., Mendoza-Santoyo, F.M.: J. Opt. Soc. Am. A **9** (1992) 2000–2008.

93Col Collett, E.: Polarized light – fundamentals and applications, New York: Marcel Dekker, 1993.
93Dav Davies, J.C., Buckberry, C.H.: Television holography and its applications, in: Williams, D.C. (ed.): Optical methods in engineering metrology, London: Chapman and Hall, 1993.
93Hun Huntley, J.M., Saldner, J.: Appl. Opt. **32** (1993) 3047–3052.
93Kau Kaufmann, G.H.: Automatic fringe analysis procedures in speckle metrology, in: Sirohi, R.S.: Speckle metrology, New York: Marcel Dekker, 1993.
93Lok Lokberg, O.J.: Recent developments in video speckle interferometry, in: Sirohi, R.S.: Speckle metrology, New York: Marcel Dekker, 1993, p. 157–194.
93Ped Pedrini, G., Pfister, B., Tiziani, H.J.: J. Mod. Opt. **40** (1993) 89–96.
93Pry Pryputniewicz, R.J.: Proc. SPIE (Int. Soc. Opt. Eng.) **1821** (1993) 27–37.
93Rob Robinson, D.W., Reid, G.T.: Interferogram analysis: Digital fringe pattern measurement techniques, UK: IOP Publications Ltd, 1993.
93Sch Schwider, J., Falkensdorfer, O., Schreiber, H., Zöller, A., Streibl, N.: Opt. Eng. **32** (1993) 1883.
93Sir Sirohi, R.S.: Speckle metrology, New York: Marcel Dekker, 1993.
93Yam Yamaguchi, I.: Theory and application of speckle displacement, in: Sirohi, R.S.: Speckle metrology, New York: Marcel Dekker, 1993.

94Joe Joenathan, C., Tiziani, H.J., Franze, B.: Appl. Opt. **33** (1994) 7305–7311.
94Oka Okada, E., Enomoto, H., Minamitani, H.: Proc. IEEE: IECON 1994, Vol. 2 (1994) 890–893.
94Sch Schnars, U.: J. Opt. Soc. Am. A **11** (1994) 2011–2015.
94Sre Sreedhar, R., Krishna Mohan, K., Sirohi, R.S.: Opt. Eng. **33** (1994) 1989–95.
94Zou Zou, Y., Pedrini, G., Tiziani, H.J.: J. Mod. Opt. **41** (1994) 1637–52.

95Ped Pedrini, G., Zou, Y., Tiziani, H.J.: J. Mod. Opt. **42** (1995) 367–374.
95Vdo Vdovin, G., Sarro, P.M.: Appl. Opt. **34** (1995) 2968.

96Goo Goodman, W.: Introduction to Fourier optics, New York: McGraw-Hill, 1996.
96Kre Kreis, Th.: Holographic interferometry, principles and methods, Berlin: Akademie Verlag, 1996.
96Lei Leibbrand, G.W.R., Harbeers, G., Kunst, P.J.: Appl. Opt. **35** (1996) 6151.

96Mei Meinschmidt, P., Hinsch, K.D., Sirohi, R.S.: Selected papers on speckle pattern interferometry – principles and practice, Washington: SPIE Press, 1996.
96Ped Pedrini, G., Zou, Y., Tiziani, H.J.: J. Mod. Opt. **43** (1996) 395–407.
96Sch Schnars, U., Kreis, Th., Jueptner, W.P.: Opt. Eng. **35** (1996) 977–982.
96Tiz1 Tiziani, H.J., Maier, N., Rothe, A.: Opt. Commun. **123** (1996) 34.
96Tiz2 Tiziani, H.J., Rothe, A., Maier, N.: Appl. Opt. **45** (1996) 3225.

97Ada Adams, M., Kreis, Th., Jueptner, W.: Proc. SPIE (Int. Soc. Opt. Eng.) **3098** (1997) 234.
97Bot Bothe, T., Burke, J., Helmers, H.: Appl. Opt. **36** (1997) 5310–5316.
97Her Hertwig, M.: Proc. SPIE (Int. Soc. Opt. Eng.) **3098** (1997) 90–105.
97Hun Huntley, J.M., Saldner, H.: Opt. Eng. **36** (1997) 610–615.
97Ped1 Pedrini, G., Froening, Ph., Fessler, H., Tiziani, H.J.: Opt. Laser Technol. **29** (1997) 505–511.
97Ped2 Pedrini, G., Tiziani, H.J.: Opt. Laser Technol. **29** (1997) 249–256.
97Ped3 Pedrini, G., Tiziani, H.J., Zou, Y.: Opt. Lasers Eng. **26** (1997) 199–219.
97Ped4 Pedrini, G., Zou, Y., Tiziani, H.J.: Appl. Opt. **36** (1997) 786–792.
97Ras1 Rastogi, P.K.: Opt. Lasers Eng. **26** (1997) 83–278.
97Ras2 Rastogi, P.K.: Optical measurement techniques and applications, London: Artech House Boston, 1997.
97Sch Schreiber, H., Schwider, J.: Appl. Opt. **36** (1997) 5321–5324.
97Tiz1 Tiziani, H.J.: Chap. 2, in: Rastogi, P.K. (ed.): Optical measuring techniques and applications, Boston: Artech House Inc., 1997.
97Tiz2 Tiziani, H.J., Franze, B., Haible, P.: J. Mod. Opt. **44** (1997) 1485.

98Fra Franze, B., Tiziani, H.J.: J. Mod. Opt. **45** (1998) 861.
98Gre Gren, P., Schedin, S., Li, X.: Appl. Opt. **37** (1998) 834–840.
98Joe1 Joenathan, C., Franze, B., Haible, P., Tiziani, H.J.: Appl. Opt. **37** (1998) 2608–2614.
98Joe2 Joenathan, C., Franze, B., Haible, P., Tiziani, H.J.: Appl. Opt. **37** (1998) 3385–3390.
98Mov Movilla, J.M., Piquero, G., Martínez-Herrero, R., Mejías, P.M.: Opt. Commun. **149** (1998) 230.
98Ped Pedrini, G., Froening, Ph., Fessler, H., Tiziani, H.J.: Appl. Opt. **37** (1998) 6262–6269.
98Seb Sebacher, S., Osten, W., Jueptner, W.: Proc. SPIE (Int. Soc. Opt. Eng.) **3479** (1998) 104–115.
98Ste Steinchen, W., Yang, L.X., Kupfer, G., Mackel, P., Vossing, F.: J. Strain Anal. **33** (1998) 171–182.

99Joe Joenathan, C., Franze, B., Haible, P., Tiziani, H.J.: Appl. Opt. **38** (1999) 1169–1178.
99Moo Moore, A.J., Hand, D.P., Barton, J.S., Jones, J.D.C.: Appl. Opt. **38** (1999) 1159–1162.
99Ped1 Pedrini, G., Fröning, Ph., Tiziani, H.J., Gusev, M.E.: Appl. Opt. **38** (1999) 3460–3467.
99Ped2 Pedrini, G., Fröning, Ph., Tiziani, H.J., Mendoza Santoyo, F.: Opt. Commun. **164** (1999) 257–268.
99Ped3 Pedrini, G., Schedin, S., Tiziani, H.J.: Opt. Commun. **171** (1999) 29–36.
99Piq Piquero, G., Movilla, J.M., Mejías, P.M., Martínez-Herrero, R.: Opt. Quantum Electron. **31** (1999) 223.
99Sch Schedin, S., Pedrini, G., Tiziani, H.J.: Opt. Commun. **165** (1999) 183–188.
99Sir Sirohi, R.S., Chau, F.S.: Optical methods of measurement: Whole field techniques, New York: Marcel Dekker, 1999.
99Wag Wagner, C., Seebacher, S., Osten, W., Jüptner, W.: Appl. Opt. **38** (1999) 4812–4820.

00Kem Kemper, B., Dirksen, D., Avenhaus, W., Merker, A., von Bally, G.: Appl. Opt. **39** (2000) 3899–3905.

00Mov Movilla, J.M., Piquero, G., Mejías, P.M., Martínez-Herrero, R.: Opt. Quantum Electron. **32** (2000) 1333.
00Tot Totzeck, M., Jacobsen, H., Tiziani, H.J.: Appl. Opt. **39** (2000) 6295–6305.

01Ge Ge, Z., Kobayashi, F., Matsuda, S., Takeda, M.: Appl. Opt. **40** (2001) 1649.
01Gru Gruber, M., Hagedorn, D., Eckert, W.: Appl. Opt. **40** (2001) 5052–5055.
01Kum Kumar, R., Singh, S.K., Shakher, C.: Opt. Laser Technol. **33** (2001) 567–571.
01Leh Lehmann, M.: Speckle statistics in the context of digital speckle interferometry, in: Rastogi, P.K. (ed.): Digital speckle pattern interferometry and related techniques, Chichester: John Wiley & Sons, 2001.
01Moo Moore, A.J., Jones, J.D.C., Valera, J.D.R.: Dynamic measurement, in: Rastogi, P.K. (ed.), Digital speckle pattern interferometry and related techniques, Chichester: John Wiley & Sons, 2001.
01Ped Pedrini, G., Tiziani, H.J.: Digital holographic interferometry, in: Rastogi, P.K. (ed.): Digital speckle pattern interferometry and related techniques, Chichester: John Wiley & Sons, 2001.
01Per Perez-Lopez, C., Mendoza Santoyo, F., Pedrini, G., Schedin, S., Tiziani, H.J.: Appl. Opt. **40** (2001) 5106–5110.
01Ras1 Rastogi, P.K.: Digital speckle pattern interferometry and related techniques, Chichester: John Wiley & Sons, 2001.
01Ras2 Rastogi, P.K.: Surface displacements, derivatives and shapes, in: Rastogi, P.K. (ed.): Digital speckle pattern interferometry and related techniques, Chichester: John Wiley & Sons, 2001.
01Sch Schedin, S., Pedrini, G., Tiziani, H.J., Aggarwal, A.K., Gusev, M.E.: Appl. Opt. **40** (2001) 100–103.
01See Seebacher, S., Osten, W., Baumbach, T., Jüptner, W.: Opt. Lasers Eng. **36** (2001) 103–126.
01Tiz Tiziani, H.J.: Optik (Stuttgart) **9** (2001) 370–380.

02Kol Kolenovic, E., Lai, S., Osten, W., Jüptner, W.: A miniaturized digital holographic endoscopic system for shape and deformation measurement, in: VDI Berichte 1694: International symposium on photonics and measurement, Düsseldorf: VDI Verlag GmbH, 2002, p. 79–84.

03Har Hariharan, P.: Optical interferometry, 2nd edition, London: Academic Press, 2003.
03Kol Kolenovic, E., Osten, W., Klattenhoff, R., Lai, S., von Kopylow, Ch., Jüptner, W.: Appl. Opt. **42** (2003) 5167–5172.
03Mad Madjarova, D., Kadono, V., Toyooka, H.: Opt. Express **6** (2003) 617.
03Ped1 Pedrini, G., Alexeenko, I., Osten, W., Tiziani, H.J.: Appl. Opt. **42** (2003) 5846–5854.
03Ped2 Pedrini, G., Gusev, M., Schedin, S., Tiziani, H.J.: Opt. Lasers Eng. **40** (2003) 487–499.
03Rei Reichelt, S., Pruss, C., Tiziani, H.J.: Appl. Opt. **42** (2003) 4468–4479.
03Wya Wyant, J.C.: Opt. Photonics News **15** (2003) 36.

04Joe Joenathan, C., Tiziani, H.J.: Speckle metrology, in: Wiley: Optics Encyclopedia, 2004.
04Lie Liesener, J., Tiziani, H.J.: Proc. SPIE (Int. Soc. Opt. Eng.) **5252** (2004) 264–271.
04Pru Pruss, C., Tiziani, H.J.: Opt. Commun. **233** (2004) 15–19.
04Tiz Tiziani, H.J., Totzeck, M.: High-precision optical metrology for surfaces, Chap. 5.1, in: Landolt-Börnstein, Group VIII, Vol. 1, Laser Physics and Applications, Subvol. C, Berlin: Springer-Verlag, 2004.